



저작자표시-비영리-변경금지 2.0 대한민국

이용자는 아래의 조건을 따르는 경우에 한하여 자유롭게

- 이 저작물을 복제, 배포, 전송, 전시, 공연 및 방송할 수 있습니다.

다음과 같은 조건을 따라야 합니다:



저작자표시. 귀하는 원저작자를 표시하여야 합니다.



비영리. 귀하는 이 저작물을 영리 목적으로 이용할 수 없습니다.



변경금지. 귀하는 이 저작물을 개작, 변형 또는 가공할 수 없습니다.

- 귀하는, 이 저작물의 재이용이나 배포의 경우, 이 저작물에 적용된 이용허락조건을 명확하게 나타내어야 합니다.
- 저작권자로부터 별도의 허가를 받으면 이러한 조건들은 적용되지 않습니다.

저작권법에 따른 이용자의 권리는 위의 내용에 의하여 영향을 받지 않습니다.

이것은 [이용허락규약\(Legal Code\)](#)을 이해하기 쉽게 요약한 것입니다.

[Disclaimer](#)

Doctoral Thesis

**A Study on Gas Hydrate-based F-gas Separation
and Discovery of New F-gas Hydrates**

Eunae Kim

Department of Urban and Environmental Engineering
(Environmental Science and Engineering)

Graduate School of UNIST

2019

A Study on Gas Hydrate-based F-gas Separation and Discovery of New F-gas Hydrates

Eunae Kim

Department of Urban and Environmental Engineering
(Environmental Science and Engineering)

Graduate School of UNIST

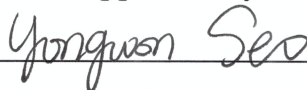
A Study on Gas Hydrate-based F-gas Separation
and Discovery of New F-gas Hydrates

A thesis/dissertation
submitted to the Graduate School of UNIST
in partial fulfillment of the
requirements for the degree of
Doctor of Philosophy

Eunae Kim

12. 11. 2019

Approved by



Advisor

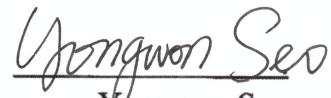
Yongwon Seo

A Study on Gas Hydrate-based F-gas Separation and Discovery of New F-gas Hydrates

Eunae Kim

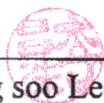
This certifies that the dissertation of Eunae Kim is approved.

December 11th, 2018



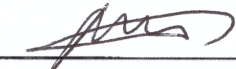
Yongwon Seo

School of Urban and Environmental Engineering
Ulsan National Institute of Science and Technology
Committee Chairperson



Chang soo Lee

School of Urban and Environmental Engineering
Ulsan National Institute of Science and Technology
Committee Member



Sung-Deuk Choi

School of Urban and Environmental Engineering
Ulsan National Institute of Science and Technology
Committee Member



Sang Kyu Kwak

School of Energy and Chemical Engineering
Ulsan National Institute of Science and Technology
Committee Member



Seong-Pil Kang

Greenhouse Gas Laboratory
Korea Institute of Energy Research
Committee Member

ABSTRACT

This study investigated thermodynamic and microscopic characteristics of various F-gas hydrates to examine the feasibility of gas hydrate-based F-gas separation process and to demonstrate the newly discovered F-gas hydrates. Thermodynamic phase equilibria were measured to determine the thermodynamically stable region of each F-gas hydrate, while powder X-ray diffraction was conducted to identify the gas hydrate crystal structure and lattice parameter. In addition, ^{13}C & ^{19}F NMR and *in-situ* Raman spectroscopy were utilized to confirm the hydrate structure and observe cage-filling guest-molecular behavior. Lastly, the gas and hydrate phase compositions were analyzed via gas chromatography to examine the separation efficiency by gas hydrate formation process. From the experimental results, the thermodynamic stability range of pure CHF_3 and $\text{CHF}_3 + \text{N}_2$ gas hydrates demonstrated that CHF_3 can be captured in hydrate phase with high separation efficiency, while they form sI hydrate regardless of CHF_3 concentrations used in this study. On the other hand, pure C_2F_6 and $\text{C}_2\text{F}_6 + \text{N}_2$ gas mixture formed sII hydrates, and since $\text{C}_2\text{F}_6 + \text{N}_2 + \text{water}$ system showed an azeotropic behavior at high temperature range, restricting the gas hydrate-based separation process only applicable at specific temperature and pressure range. Lastly, the fundamental thermodynamic and spectroscopic properties of pure NF_3 hydrate were obtained to estimate the feasibility for gas hydrate-based separation process. This study also made important discoveries on two F-gases (c- C_4F_8 and C_3F_8) which form sH hydrate in presence of suitable guest molecules. Since C_3F_8 and c- C_4F_8 molecules have large molecular sizes, those molecules have not been expected to be enclathrated in sI or sII hydrate cages. However, this study discovered that c- C_4F_8 molecules can be enclathrated in sH large ($5^{12}6^8$) cages in presence of CH_4 as help gas, which was demonstrated through PXRD and ^{13}C NMR spectroscopy. In addition, C_3F_8 was found to act as a dual hydrate former between sH and sII hydrates according to help gas molecules. Via ^{13}C NMR and Raman spectroscopy, C_3F_8 was confirmed to form sH hydrate with CH_4 , while forming sII hydrate in presence of SF_6 . The discovery of c- C_4F_8 and C_3F_8 as sH hydrate former is very meaningful, since there have been no gas-phase sH hydrate former investigated until present. The overall results obtained in this study provide invaluable information of various properties of F-gas hydrates, and are expected to be useful sources for gas hydrate application fields in the future.

Contents

Chapter 1. Introduction	1
1.1. Introduction of Gas Hydrates	1
1.2. F-gases and Global Warming Effects	4
Chapter 2. Experimental Investigation	7
2.1. Materials	7
2.2. Experimental Apparatus and Procedure	7
2.2.1. Hydrate Phase Equilibria Measurement	7
2.2.2. Hydrate Structure Identification	10
2.2.3. Microscopic Analyses of Hydrate Phase	10
2.2.4. Composition Analyses and Gas Consumption Measurement	11
Chapter 3. Gas Hydrate-based F-gases Separation	12
3.1. Gas Hydrate Formation with Pure CHF ₃ and C ₂ F ₆ Gases	12
3.1.1. Abstract	12
3.1.2. Thermodynamic Phase Equilibria	13
3.1.3. Microscopic Analyses on Pure CHF ₃ and C ₂ F ₆ Hydrates	16
3.1.4. Computational Methods and Results	23
3.1.5. Conclusions	28
3.2. Gas Hydrate-based CHF ₃ Separation from CHF ₃ + N ₂ Mixture Gas	29
3.2.1. Abstract	29
3.2.2. Thermodynamic Phase Equilibria	30
3.2.3. Thermodynamic and Kinetic Examination on Separation Efficiency	33
3.2.4. Crystal Structures and Cage-filling Characteristics of CHF ₃ + N ₂ Hydrates	37
3.2.5. Conclusions	43
3.3. The Azeotropic Behavior of C ₂ F ₆ + N ₂ Gas Hydrates	45
3.3.1. Abstract	45
3.3.2. Thermodynamic Phase Equilibria	46
3.3.3. Structural Analyses through PXRD	49
3.3.4. Pressure-Composition Analyses	51
3.3.5. Conclusions	54
3.4. NF ₃ Hydrate Formation and its Microscopic Properties	55
3.4.1. Abstract	55
3.4.2. Thermodynamic Phase Equilibria	56
3.4.3. Microscopic Analyses on Pure NF ₃ Hydrate	59
3.4.4. Conclusions	63

Chapter 4. Novel discoveries on sH hydrate forming F-gases	64
4.1. A New Discovery of Abnormal sH Hydrate Former: $c\text{-C}_4\text{F}_8$ Gas Molecules	64
4.1.1. Abstract	64
4.1.2. Thermodynamic Phase Equilibria	65
4.1.3. Microscopic Demonstration of sH Hydrate Formation	68
4.1.4. Conclusions	71
4.2. An Investigation on Dual (sH/sII) Hydrate Former: C_3F_8 Gas Molecules	73
4.2.1. Abstract	73
4.2.2. Thermodynamic Phase Equilibria	74
4.2.3. Microscopic Analyses on sH Hydrate	77
4.2.4. Observation of sII Hydrate Formation through in-situ Raman Spectroscopy	80
4.2.5. Conclusions	83
Chapter 5. Conclusions and Future Perspectives	84
5.1. Conclusions	84
5.2. Future Perspectives	87
References	92
Acknowledgement	99

List of Figures

Figure 1.1.1. Three Representative Structures of Gas Hydrates. (a) sI Hydrates (b) sII Hydrates (c) sH Hydrates.

Figure 1.1.2. Various Fields of Gas Hydrates.

Figure 2.2.1. Schematic diagram of the apparatus for phase equilibria measurement.

Figure 2.2.2. Determination of three-phase (H-L_w-V) equilibrium point.

Figure 3.1.1. (a) H-L_w-V, H-L_{CHF₃}-V, L_w-L_{CHF₃}-V equilibria of the pure CHF₃ + water system. (b) H-L_w-V, H-L_{C₂F₆}-V, L_w-L_{C₂F₆}-V equilibria of the pure C₂F₆ + water system.

Figure 3.1.2. (a) PXRD patterns of the pure CHF₃ hydrate (*Pm3n*, *a* = 11.91 Å). (b) PXRD patterns of the pure C₂F₆ hydrate (*Fd3m*, *a* = 17.15 Å). Asterisks (*) indicate hexagonal ice (Ih).

Figure 3.1.3. (a) ¹³C MAS NMR spectra of CHF₃ gas and pure CHF₃ hydrate at 240 K. (b) ¹⁹F MAS NMR spectra of CHF₃ gas and pure CHF₃ hydrate at 240 K.

Figure 3.1.4. (a) ¹³C MAS NMR spectra of C₂F₆ gas and pure C₂F₆ hydrate at 240 K. (b) ¹⁹F MAS NMR spectra of C₂F₆ gas and pure C₂F₆ hydrate at 240 K.

Figure 3.1.5. (a) Real-time Raman spectra for the C-H stretching mode of pure CHF₃ hydrate at 278.15 K and 2.5 MPa. (b) Final Raman spectrum of the C-H stretching mode for pure CHF₃ hydrate.

Figure 3.1.6. Optimized structures for unit cells of (a) sI hydrate (cubic) and (b) sII hydrate (rhombohedral).

Figure 3.1.7. Optimized structure for CHF₃ and C₂F₆ hydrate cage by DFT calculations. (a) and (b) represent CHF₃ in large (5¹²6²) and small cages (5¹²) of sI hydrate, respectively. (c) and (d) represent C₂F₆ in large (5¹²6⁴) and small (5¹²) cages of sII hydrate, respectively. Black, cyan, and light purple colors represent hydrogen, carbon, and fluorine atoms, respectively. (For interpretation of the references to colour in this figure legend, the reader is referred to the web version of this article.)

Figure 3.1.8. Interaction energies (kcal/mol) in terms of (a) the occupancy of small cage (5¹²) of CHF₃ in sI hydrate and (b) the occupancy of large cage (5¹²6⁴) of C₂F₆ in sII hydrate.

Figure 3.2.1. Hydrate phase equilibria of CHF₃ + N₂ + water mixtures.

Figure 3.2.2. PXRD patterns of CHF₃ + N₂ hydrates. Asterisks (*) indicate hexagonal ice (Ih).

Figure 3.2.3. Pressure-composition diagram of $\text{CHF}_3 + \text{N}_2$ hydrates at 279.15 K and 283.15 K.

Figure 3.2.4. Gas uptake for two different pressure conditions (2.5 and 3.5 MPa) during CHF_3 (40%) + N_2 (60%) hydrate formation at 279.15 K.

Figure 3.2.5. Composition change in the vapor phase for two different pressure conditions (2.5 and 3.5 MPa) during CHF_3 (40%) + N_2 (60%) hydrate formation at 279.15 K.

Figure 3.2.6. Raman spectra of $\text{CHF}_3 + \text{N}_2$ hydrates at 279.15 K and $\Delta P=1.0$ MPa. (a) N-N stretching mode of N_2 molecules. (b) C-H stretching mode of CHF_3 molecules.

Figure 3.2.7. (a) Real time Raman spectra of the C-H stretching mode for CHF_3 (40%) + N_2 (60%) hydrate at 279.15 K and 2.5 MPa ($\Delta P=1.0$ MPa). (b) Cage occupancy ratio (θ_i/θ_s) of CHF_3 molecules captured in CHF_3 (40%) + N_2 (60%) hydrate at 279.15 K and 2.5 MPa ($\Delta P=1.0$ MPa).

Figure 3.2.8. A hybrid system of gas hydrate-based CHF_3 separation process combined with membrane/adsorption and liquefaction processes.

Figure 3.3.1. Three-phase (H-L_w-V) equilibria of pure C_2F_6 and $\text{C}_2\text{F}_6 + \text{N}_2$ hydrates.

Figure 3.3.2. PXRD patterns of pure C_2F_6 and $\text{C}_2\text{F}_6 + \text{N}_2$ hydrates at 123.15 K. Asterisks (*) indicate hexagonal ice (I_h).

Figure 3.3.3. Pressure-composition diagram of $\text{C}_2\text{F}_6 + \text{N}_2 + \text{H}_2\text{O}$ systems at 275.15 K and 279.15 K.

Figure 3.4.1. Three-phase (H-L_w-V) equilibria of pure NF_3 hydrate.

Figure 3.4.2. PXRD patterns of pure NF_3 hydrate at 123.15 K. Asterisks (*) indicate hexagonal ice (I_h).

Figure 3.4.3. Raman spectra of pure NF_3 hydrate and its deconvolution.

Figure 4.1.1. H – L_w – V equilibrium curves of c- $\text{C}_4\text{F}_8 + \text{CH}_4$ clathrate hydrates.

Figure 4.1.2. PXRD patterns of c- C_4F_8 (5.0%) + CH_4 (95.0%) clathrate hydrate. Asterisks (*) indicate hexagonal ice (I_h).

Figure 4.1.3. ^{13}C NMR spectra of c- C_4F_8 (5.0%) + CH_4 (95.0%) clathrate hydrate.

Figure 4.1.4. Illustration for inclusion of c- C_4F_8 and CH_4 in the sH unit cell.

Figure 4.2.1. (a) Three-phase (H-L_w-V) equilibria of C_3F_8 (10%) + CH_4 (90%) hydrate.

(b) Three-phase (H-L_w-V) equilibria of C_3F_8 (25%) + SF_6 (75%) and C_3F_8 (50%) + SF_6 (50%) hydrates.

Figure 4.2.2. PXRD patterns of C_3F_8 (10%) + CH_4 (90%) hydrate at 123.15 K.

Figure 4.2.3. (a) PXRD patterns of C_3F_8 (25%) + SF_6 (75%) hydrate at 123.15 K.

(b) PXRD patterns of C_3F_8 (50%) + SF_6 (50%) hydrate at 123.15 K.

Figure 4.2.4. ^{13}C NMR spectra of C_3F_8 (10%) + CH_4 (90%) hydrate.

Figure 4.2.5. Raman spectra of C_3F_8 (10%) + CH_4 (90%) hydrate.

Figure 4.2.6. (a) Real time Raman spectra of C_3F_8 (25%) + SF_6 (75%) hydrate at 279.65 K and 1.05 MPa ($\Delta T=5$ K).

(b) Final Raman spectra of C_3F_8 (25%) + SF_6 (75%) hydrate at 279.65 K and 1.05 MPa ($\Delta T=5$ K).

Figure 5.2.1. Comparison of thermodynamic CHF_3 separation efficiency between gas hydrate formation and liquefaction processes.

(a) Effect of CHF_3 mole fraction in feed gas at 283.15 K and 4.0 MPa.

(b) Effect of CHF_3 mole fraction in feed gas at 279.15 K and 4.0 MPa.

Figure 5.2.2. Comparison of thermodynamic CHF_3 separation efficiency between gas hydrate formation and liquefaction processes.

(a) Effect of pressure with CHF_3 mole fraction of 0.4 at 283.15 K.

(b) Effect of pressure with CHF_3 mole fraction of 0.4 at 279.15 K.

Figure 5.2.3. Hydrate dissociation thermogram for pure CHF_3 + water system at 1.8 MPa with a heating rate of 1 K/min.

Figure 5.2.4. Additional works required for overall gas hydrate-based F-gas separation process optimization.

List of Tables

Table 1.1.1. Geometry and Crystal Parameters of Gas Hydrate Cages.

Table 1.1.2. F-gas Capture and Recovery Methods Developed until Now.

Table 1.2.1. Atmospheric Lifetimes and Global Warming Potentials of Various F-gases.

Table 3.1.1. Hydrate phase equilibrium data of the $\text{CHF}_3 + \text{water}$ system.

Table 3.1.2. Hydrate phase equilibrium data of the $\text{C}_2\text{F}_6 + \text{water}$ system.

Table 3.1.3. Occupancies of gas molecules for small and large cages in sI and sII hydrates of the $(3 \times 3 \times 3)$ supercell system. The numbers in parentheses represent average numbers of enclathrated gas molecules over the total number of each cage in sI and sII hydrates, respectively.

Table 3.2.1. Hydrate phase equilibrium data of the $\text{CHF}_3 + \text{N}_2 + \text{water}$ system.

Table 3.3.1. The three-phase (H-L_W-V) equilibria of the $\text{C}_2\text{F}_6 + \text{N}_2 + \text{H}_2\text{O}$ systems.

Table 3.3.2. Pressures and compositions of $\text{C}_2\text{F}_6 + \text{N}_2 + \text{H}_2\text{O}$ systems at 275.15 K and 279.15 K.

Table 3.4.1. Hydrate phase equilibrium data of the $\text{NF}_3 + \text{water}$ system.

Table 4.1.1. H – L_W – V equilibrium data of c-C₄F₈ + CH₄ clathrate hydrates

Table 4.2.1. (a) Three-phase (H-L_W-V) equilibria of C₃F₈ + CH₄ hydrate

(b) Three-phase (H-L_W-V) equilibria of C₃F₈ + SF₆ hydrates

Chapter 1. Introduction

1.1. Introduction of Gas Hydrates

Gas hydrates, also called clathrate hydrates, are non-stoichiometric crystalline compounds that occur when water molecules form cage-like lattices via hydrogen bonding around guest molecules under high pressure and low temperature conditions [1]. There are three representative structures of gas hydrates that contain different sizes and shapes of cages: structure I (sI), structure II (sII), and structure H (sH). The unit cell of sI hydrate consists of two small (5^{12}) cages and six large ($5^{12}6^2$) cages; sII hydrate consists of sixteen small (5^{12}) cages and eight large ($5^{12}6^4$) cages; and sH hydrate consists of three small (5^{12}) cages, two medium ($4^35^66^3$) cages, and one large ($5^{12}6^8$) cage [1]. In general, small gas molecules such as methane and carbon dioxide form sI hydrates, while larger guests such as propane and tetrahydrofuran, or much smaller gas molecules such as nitrogen and oxygen, form sII hydrates. sH hydrates have been known to be formed with large liquid hydrocarbons such as neohexane and methylcyclopentane in the presence of small help gases such as methane or hydrogen sulfide [1].

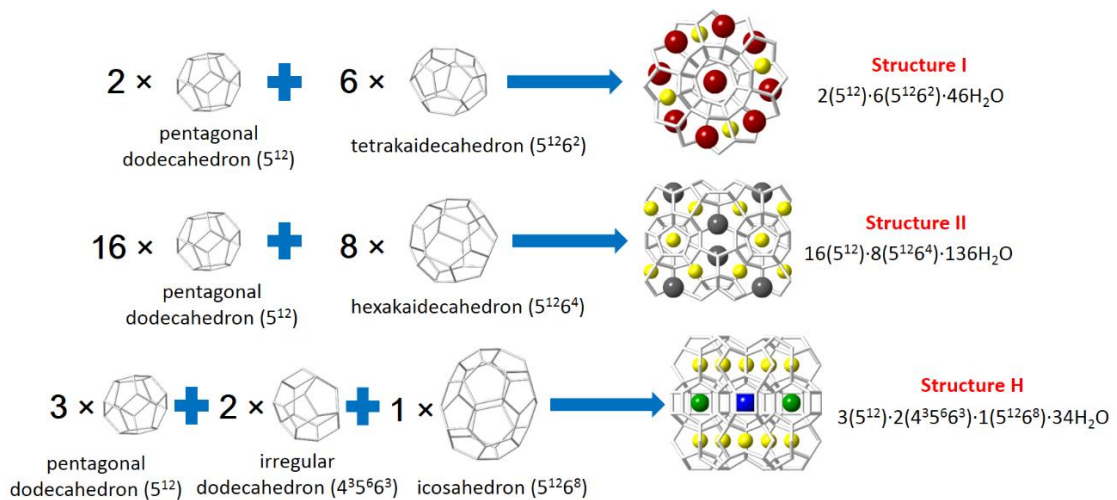


Figure 1.1.1. Three Representative Structures of Gas Hydrates.

(a) sI Hydrates (b) sII Hydrates (c) sH Hydrates

Table 1.1.1. Geometry and Crystal Parameters of Gas Hydrate Cages [1]

	Structure I		Structure II		Structure H		
Crystal System	Cubic		Cubic		Hexagonal		
Space Group	Pm3n		Fd3m		P6/mmm		
Lattice Parameters	a=b=c=12 Å		a=b=c=17.3 Å		a=b=12.2 Å c=10.1 Å		
Cavity	Small	Large	Small	Large	Small	Medium	Large
Description	5 ¹²	5 ¹² 6 ²	5 ¹²	5 ¹² 6 ⁴	5 ¹²	4 ³ 5 ⁶ 6 ³	5 ¹² 6 ⁸
No. of Cavities / Unit cell	2	6	16	8	3	2	1
Average Cavity Radius (Å)	3.95	4.33	3.91	4.73	3.94	4.04	5.79
No. of Water Molecules / Cavity	20	24	20	28	20	20	36

There are various applications of gas hydrates, such as natural gas storage/transportation, CO₂ capture and storage, and desalination [2-30]. In particular, researchers have proposed gas hydrate-based CO₂ capture from pre-combustion fuel gas mixtures or post-combustion flue gas mixtures [8-16]; subsequently, the possibility of sequestering CO₂ into the deep ocean or naturally occurring gas hydrate layers has been proposed in order to mitigate the global warming effect caused by the increased concentration of CO₂ in the atmosphere [17-19]. Similarly, other global warming gases such as fluorinated gases (F-gases) should be sequestered from the emission source in order to reduce their environmental impacts, and gas hydrate formation is expected to be a potential mean to separate them efficiently [25-30].

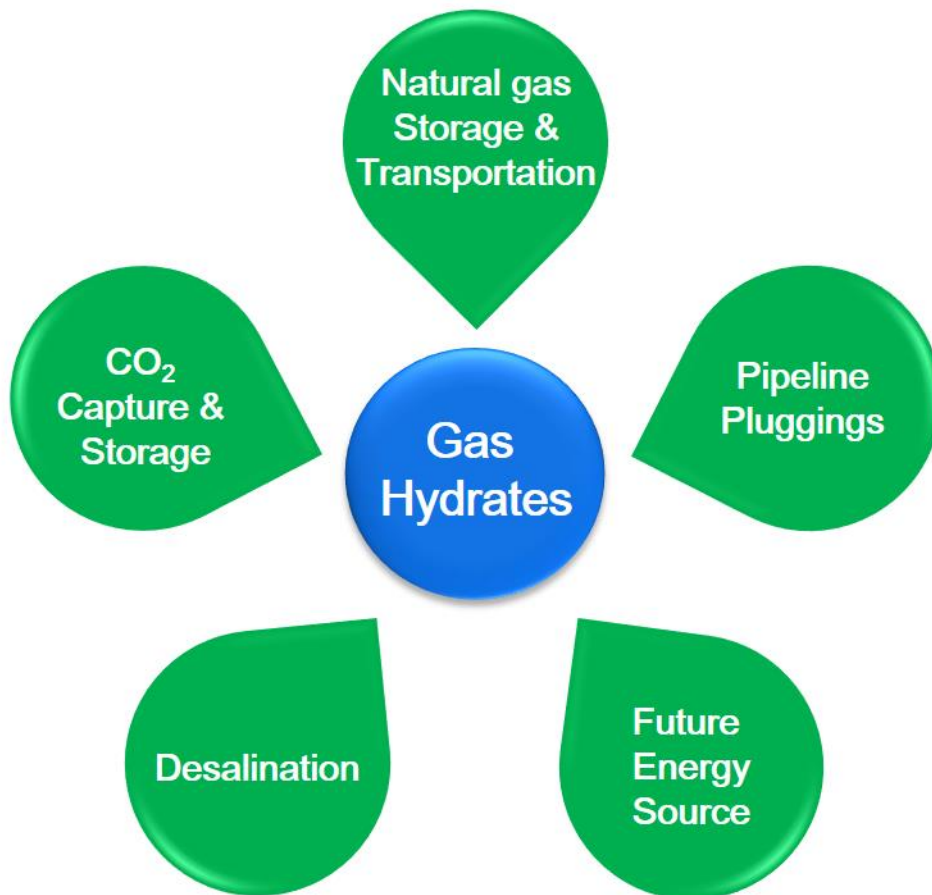


Figure 1.1.2. Various Applications of Gas Hydrates

1.2. F-gases and Global Warming Effects

F-gases are man-made gases that are widely used in various industries including semiconductor industries or refrigeration systems thanks to their high molecular stability, and the amount of F-gas emission toward the atmosphere due to the leakage of the gas during the process is gradually increasing. However, since F-gases have significantly higher global warming potentials(GWP) and long atmospheric lifetimes compared to other global warming gases (CO₂, CH₄ and N₂O), the emission of F-gases became one of the major threats of increasing the average temperature of the globe. [31-37]. Therefore, the demand of developing methods to separate and capture F-gas from the emission source have been increased. In this sense, several methods such as membrane separation, adsorption, and liquefaction have been proposed for capture and recovery of F-gases [35, 37-42]. However, these methods have drawbacks such as high operational costs and low efficiency, requiring the development of an innovative and efficient F-gas separation method which can overcome these operational limits and enables the reuse of F-gases after recovery. In this sense, gas hydrate-based separation technology was suggested as a potential option for separating and recovering F-gases. Because F-gases have a relatively larger molecular size and, accordingly, higher thermodynamic stability of gas hydrates compared with nitrogen (N₂), F-gases can be selectively captured in the gas hydrate cages when gas hydrates are formed from F-gas + N₂ gas mixtures.

Table 1.1.2. F-gas Capture and Recovery Methods Developed until Now [35, 37-42]

Capture/recovery methods	Target Gases	Features
Membrane Separation	CF ₄ , C ₂ F ₆ , C ₃ F ₈ , C ₄ F ₈ , CHF ₃ , SF ₆ , CFCs	Based on gas permeation in semi-permeable polymeric membrane. Poly ethylene oxide (PEO), polyfluorononyl moieties (PF) and silicone rubber (SR) are used. No molecular degradation.
Adsorption	CF ₄ , C ₂ F ₆ , SF ₆	Effective when there are excessive amount (>95%) of F-gases. Activated carbon as adsorbent. No molecular degradation.
Liquefaction	CF ₄ , C ₂ F ₆ , C ₃ F ₈ , CHF ₃ , SF ₆	Can obtain almost pure gas after the process. Requires thermodynamic conditions to be above the liquefaction point.

In this study, various F-gases were selected as target gases to be captured in gas hydrate phase. First, CHF₃, C₂F₆ and NF₃ hydrates were investigated, because they are commonly used in semiconductor industries as well as in refrigeration systems, while having extremely high global warming potentials (CHF₃:11,700; C₂F₆:9200, NF₃: 17,200) and long atmospheric lifetimes (CHF₃: 264 years, C₂F₆:

10,000 years, NF_3 : 740 years) [31]. In order to assess the feasibility of the hydrate-based F-gas separation process, various approaches from thermodynamic, kinetic, and spectroscopic views on both the pure F-gas hydrates and F-gas + N_2 mixed gas hydrates were required. Moreover, computational methods were combined to analyze the cage occupancy of each F-gas hydrate phase.

Second, this study demonstrated that the large molecular F-gases such as C_3F_8 (7.68Å) and *c*- C_4F_8 (7.66Å) can also form gas hydrates in presence of help gases. Since their molecular sizes are much larger than usual sI/sII hydrate former guests, they were not expected to be enclathrated in gas hydrate cages. However, this study discovered that those large molecules can also become gas hydrate formers in presence of appropriate help gas molecules. Moreover, it was demonstrated that they act as gas phase sH hydrate guests and C_3F_8 can select the hydrate structure to form respective to its help gases. The experiments to verify the enclathration of those molecules present thermodynamic phase equilibria, crystal structures and lattice parameters, and guest molecular behaviors in each hydrate phase.

The experimental and computational results from the first and second subjects of this study are presented below, and they are expected to give technological progress for gas hydrate-based F-gas separation process and broaden the gas hydrate science and possible application ranges.

Table 1.2.1. Atmospheric Lifetimes and Global Warming Potentials of Various F-gases

Industrial Name	Chemical Name	Chemical Formula	Atmospheric Lifetime (yrs)	Global Warming Potential (100yrs)
	Carbon dioxide	CO ₂	Variable	1
	Methane	CH ₄	12	21
R-23	Trifluoromethane	CHF ₃	264	11,700
R-116	Hexafluoroethane	C ₂ F ₆	10,000	9,200
R-218	Octafluoropropane	C ₃ F ₈	2,600	7,000
R-C318	c-Octafluorobutane	c-C ₄ F ₈	3,200	8,700
	Nitrogen trifluoride	NF ₃	740	17,200
	Sulfur hexafluoride	SF ₆	3,200	23,900

Chapter 2. Experimental Investigation

2.1. Materials

The highly purified CHF_3 (99.999%), C_2F_6 (99.999%), SF_6 (99.99%) and N_2 (99.99%) gases were supplied by PSG Gas Co. (Republic of Korea), whereas C_3F_8 (99.99%), $\text{c-C}_4\text{F}_8$ (100%) gases and fourteen $\text{c-C}_4\text{F}_8$ (2, 5%) + N_2 , C_3F_8 (25, 50%) + N_2 , CHF_3 / C_2F_6 (10, 20, 40, 60, 80%) + N_2 mixture gases were supplied by RIGAS (Republic of Korea). Double-distilled and deionized water was used for the gas hydrate formation. Especially, deuterium oxide (D_2O) with a purity of 99.9 atom% D was purchased from Sigma-Aldrich (USA) and used for the gas hydrate formation during *in situ* Raman analyses. All materials were used without further purification.

2.2. Experimental Apparatus and Procedure

2.2.1. Hydrate Phase Equilibria Measurement

The experimental apparatus used in this study was specifically manufactured to accurately measure the pressure and temperature during the hydrate formation and dissociation process for the purpose of the phase equilibrium measurement and sample preparation. The equilibrium cell with an internal volume of 250 cm^3 was made from 316 stainless steel, and it was immersed in a water bath connected to an external circulator with a programmable temperature controller (RW-2025G, JEIO Tech, Republic of Korea). The inner content of the equilibrium cell was strongly agitated using an impeller-type stirrer. Two sapphire windows at the front and back sides of the equilibrium cell allowed visual observation of the phase transitions that occur in the cell. A thermocouple with a temperature range from 73.15 K to 1273.15 K was introduced into the equilibrium cell in order to measure the temperature of the cell content. The thermocouple was calibrated using an ASTM 63C thermometer (H-B Instrument Company, USA) with a resolution of 0.1 K. A pressure transducer (S-10, Wika, Germany) with an uncertainty of 0.01 MPa was used to measure the pressure in the equilibrium cell, and it was calibrated using a Heise Bourdon tube pressure gauge (CMM – 137219, 0–10.0 MPa). The schematic diagram of the apparatus for phase equilibria measurement is depicted in Figure 2.2.1.

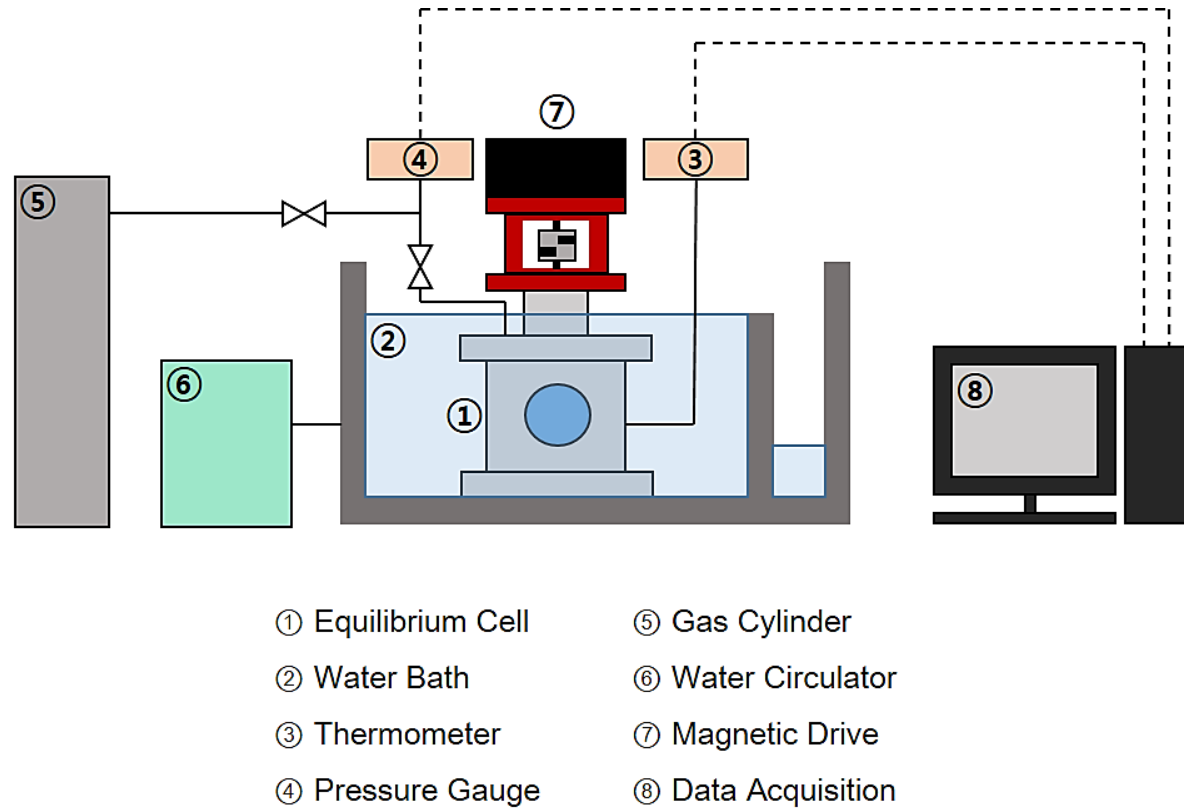


Figure 2.2.1. Schematic diagram of the apparatus for phase equilibria measurement.

In order to measure the three-phase equilibria of the F-gas + water system, the equilibrium cell was filled with approximately 80 cm³ of water. Before beginning the experiment, the equilibrium cell was ventilated at least three times with the object gas in order to remove the residual air in the cell. Then, the equilibrium cell was filled with the object gas up to the desired pressure, and the overall system temperature was slowly cooled to a temperature lower than the expected equilibrium temperature. The pressure decreased slightly as the temperature decreased until an abrupt pressure drop was observed as a result of the gas hydrate nucleation and growth. After a sufficient time for the complete conversion of water into gas hydrate, the temperature was increased in a stepwise manner at 0.1 K/90 min. The intersection point between the hydrate dissociation line and thermal expansion line at a given pressure was determined as the three-phase (gas hydrate (H) – liquid water (L_w) – vapor (V)) equilibrium point. The three-phase gas hydrate (H) – liquid F-gas (L_{F-gas}) – vapor (V) and three-phase liquid water (L_w) – liquid F-gas (L_{F-gas}) – vapor (V) equilibria were also measured for pure CHF₃ and C₂F₆ hydrates, after pressurizing the equilibrium cell up to the liquefaction pressure of CHF₃ or C₂F₆ at a given temperature.

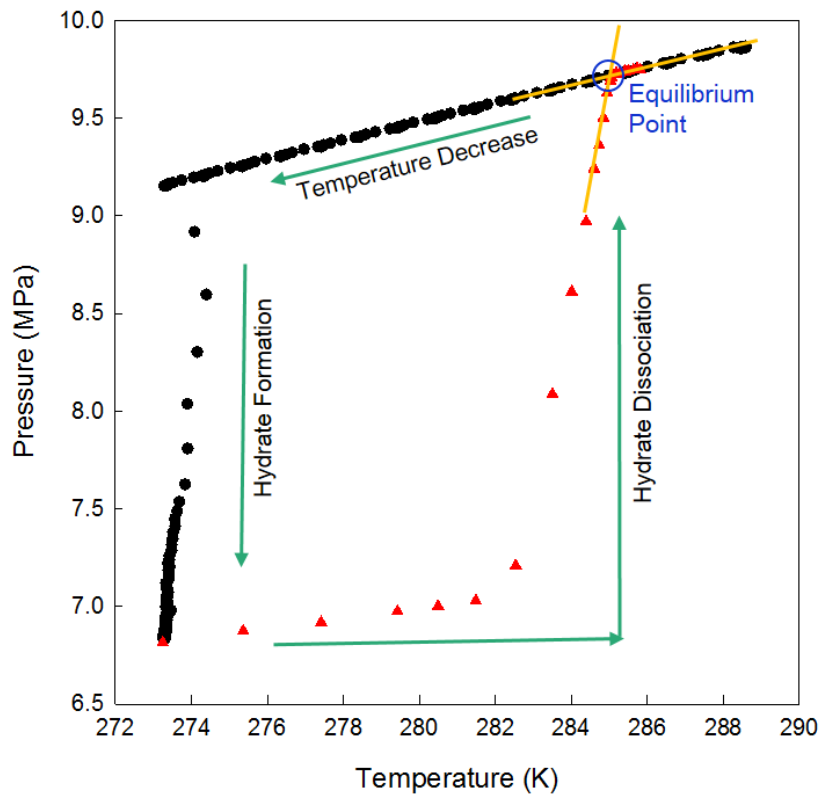


Figure 2.2.2. Determination of three-phase (H-L_w-V) equilibrium point

2.2.2. Hydrate Structure Identification

The hydrate crystal structures and their lattice parameters were usually analyzed by powder X-ray diffraction. The hydrate samples were taken from the equilibrium cell and powdered into fine particles using a 100 μm sieve in a liquid nitrogen vessel. The powder X-ray diffraction (PXRD) patterns for determination of the crystal structures were collected using an X-ray diffractometer (Rigaku Geigerflex, D/Max-RB) or PLS-II 6D C&S UNIST-PAL beamline of the Pohang Accelerator Laboratory in Republic of Korea. The diffractometers were equipped with a graphite-monochromatized Cu K α 1 radiation source ($k = 1.5406 \text{ \AA}$), and the patterns were collected in a step mode with a fixed time interval of 3 s and a step size of 0.02° for $2\theta = 5\text{--}55^\circ$ at 123.15 K. The obtained patterns were analyzed using the ChekCell program or Fullprof.

2.2.3. Microscopic Analyses of Hydrate Phase

^{13}C NMR, ^{19}F NMR and in-situ Raman spectroscopy were used to confirm enclathration of the object gas molecules and reassure the hydrate crystal structures. For NMR analyses, a Bruker 400 MHz solid-state NMR spectrometer in Korea Basic Science Institute (KBSI) was used. For sample preparation, the formed gas hydrates were finely powdered in a liquid nitrogen vessel and placed into a zirconia rotor with a 4 mm outer diameter, which was then loaded into a variable temperature (VT) probe. All ^{13}C NMR spectra were recorded at a Larmor frequency of 100.6 MHz. An excitation pulse length of 2 μs and a pulse repetition delay of 10 s under proton decoupling were applied. Radio frequency field strengths of 50 kHz, which correspond to 5 μs 90° pulses, were used for both ^{13}C and ^1H channels. The downfield carbon resonance peak of adamantane of 38.3 ppm at 300 K was used as a secondary external chemical shift reference. All ^{19}F NMR spectra were recorded at a Larmor frequency of 376.5 MHz without proton decoupling. An excitation pulse length of 2 μs (with a $\pi/2$ pulse of approximately 6 μs for an aqueous LiAsF_6 saturated solution) and a pulse repetition delay of 5 s were applied. The LiAsF_6 solution was used as a secondary external chemical shift reference using the center (-69.5 ppm) of the four peaks split by J-coupling between ^{75}As and ^{19}F . All NMR spectra were acquired at 240 K and a magic angle spinning (MAS) rate between 2 and 4 kHz. The *in situ* Raman spectroscopy was used to observe the growth process of the hydrates and the cage occupancy behavior of the guest molecules. The Raman spectra were collected using a modular Raman spectrometer (SP550, Horiba, France) equipped with a multi-channel air cooled CCD detector and a 1800 groove/mm grating. The Raman band of a silicon wafer at 520.7 cm^{-1} was used to calibrate the spectrometer. A fiber optic Raman probe, which was inserted in the high pressure reactor, enabled the acquisition of time-dependent Raman spectra during the gas hydrate formation process. After the hydrate growth process was completed, the final Raman spectra of the fully grown hydrates were obtained and deconvoluted using the Voigt function.

2.2.4. Composition Analyses and Gas Consumption Measurement

The pressure-composition analyses of the vapor and hydrate phases at three-phase (H-L_w-V) equilibrium states were measured by a gas chromatograph (7890A; Agilent Technologies, USA), which is equipped with a sampling valve (Model 7010; Rheodyne, USA) and a 5 μL loop. The gas chromatograph was connected to the high-pressure equilibrium cell through a high-pressure metering pump (Eldex, USA). A thermal conductivity detector (TCD) and a Porapak Q column (Supelco, USA) were used to detect and measure the compositions of the gas mixture. In order to achieve the three-phase (H-L_w-V) equilibrium state and to measure the equilibrium compositions, the high-pressure equilibrium cell was filled with an excess amount of water (100 cm³), which could not be completely converted into gas hydrate at a specified pressure and temperature. The pressure of the system was maintained at the desired pressure using a micro-flow syringe pump (ISCO Model 500D; Teledyne, USA). Once gas hydrate nucleation and growth occurred at specified temperatures, the system was left for 24 h to reach the three-phase (H-L_w-V) equilibrium state at each pressure and temperature condition. When the system reached a constant state, the vapor phase was circulated through a high-pressure metering pump to equilibrate both compositions of the equilibrium cell and the loop, and then, it was analyzed using a gas chromatograph. After evacuating the vapor phase from the equilibrium cell using a vacuum pump at the temperature of liquid nitrogen, the hydrate phase was dissociated at 298.15 K, and the composition of retrieved gas from the hydrate phase was also analyzed by a gas chromatograph.

Gas uptakes and compositional changes in the vapor phase during the gas hydrate formation process were measured under an isothermal and isobaric conditions. The reaction time was counted immediately after the nucleation of hydrate crystals. The gas uptake measurement was conducted in a batch system with 100 cm³ of water. The pressure was kept constant using a micro-flow syringe pump (ISCO Model 500D; Teledyne, USA), and the volume of the gas used to supplement the pressure of the reactor was recorded with a regular time interval of 10 min. Next, the volume of consumed gas was converted into the number of moles of gas molecules consumed per the number of moles of water in the reactor. During the hydrate formation, the vapor phase composition was also analyzed using the gas chromatograph (7890A; Agilent Technologies, USA) with a time interval of 10 min. All the measurements were conducted at least three times, and the average value was taken.

Chapter 3. Gas Hydrate-based F-gases Separation

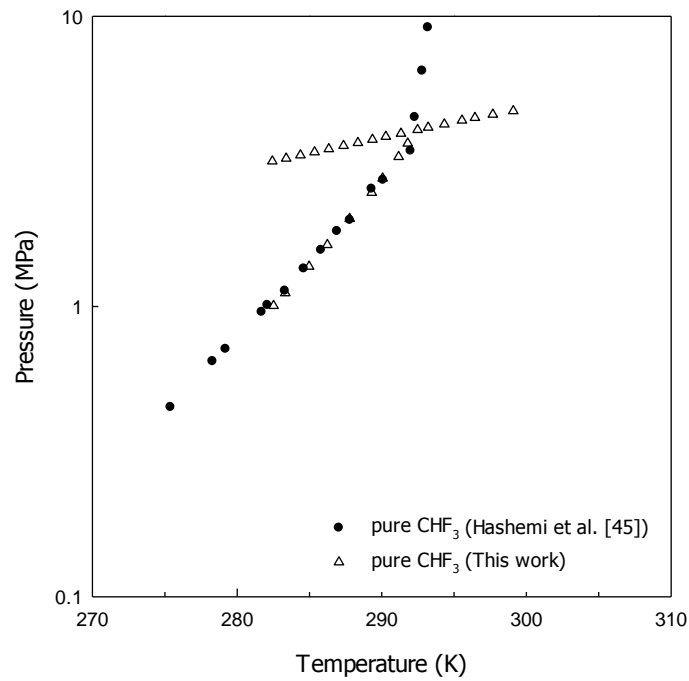
3.1. Gas Hydrate Formation with Pure CHF₃ and C₂F₆ Gases

3.1.1. Abstract

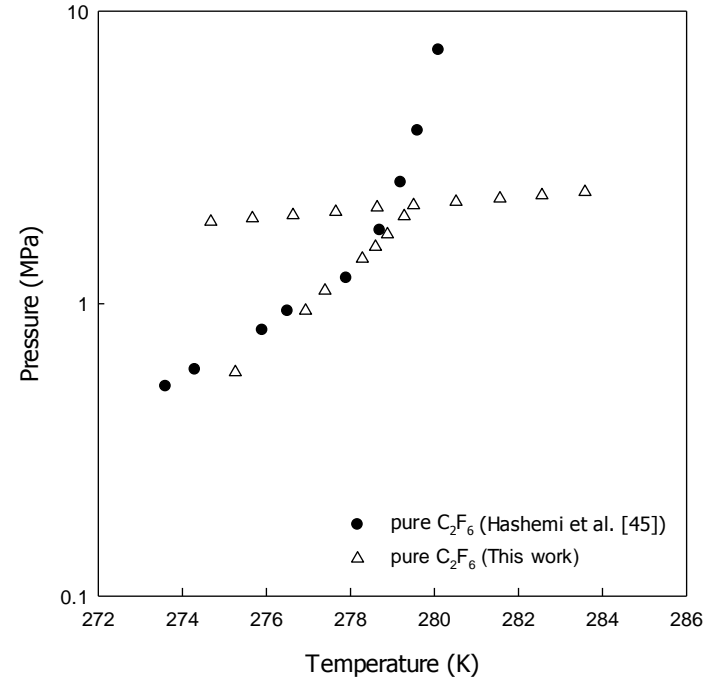
In this study, gas hydrate-based fluorinated gas (F-gas) separation is proposed as a novel method to capture F-gases. This study investigates the thermodynamic, structural, and cage filling characteristics of the gas hydrates formed by two representative F-gases (CHF₃ and C₂F₆) in order to verify the feasibility of the F-gas separation using gas hydrate formation. The three-phase (gas hydrate (H) – liquid water (L_w) – vapor (V)) equilibria of the pure CHF₃ and C₂F₆ hydrates are measured in order to examine the hydrate formation conditions. The PXRD patterns reveal the structure of the CHF₃ hydrate and the C₂F₆ hydrate as a cubic structure I (sI) and structure II (sII), respectively. The enclathration of CHF₃ and C₂F₆ molecules in each pure CHF₃ and C₂F₆ hydrate is confirmed through ¹³C and ¹⁹F NMR analyses. In-situ Raman measurements are used to monitor the growth process of pure CHF₃ hydrates, and they reveal the CHF₃ molecules trapped in the sI large (5¹²6²) cages as well as in the sI small (5¹²) cages. The computational study also demonstrates that CHF₃ is encaged in both small (5¹²) and large (5¹²6²) cages of the sI hydrate, whereas C₂F₆ only occupies the large (5¹²6⁴) cages of the sII hydrate.

3.1.2. Thermodynamic Phase Equilibria

The three-phase (H–L_w–V) equilibria of the CHF₃ + water and C₂F₆ + water systems were measured in order to determine the stability conditions of the pure CHF₃ and C₂F₆ hydrates in the temperature range of 270–300 K and the pressure range of 0.5–5 MPa. The upper end point of the H–L_w–V equilibrium line is the upper quadruple point (Q₂) where four phases of the hydrate (H)–liquid water (L_w)–liquid F-gas (L_{F-gas})–vapor (V) coexist. For the four phases to be in equilibrium at Q₂, the four neighboring three-phase equilibrium lines of H–L_w–V, H–L_{F-gas}–V, H–L_{F-gas}–L_w, and L_{F-gas}–L_w–V must intersect at this point. In order to confirm the locations of the experimentally measured Q₂, two additional three-phase equilibrium lines of H–L_{F-gas}–V and L_{F-gas}–L_w–V were measured in this study. As depicted in Figure 3.1.1 (a) and (b), three experimentally measured three-phase equilibrium lines for both the CHF₃ + water and C₂F₆ + water systems merged precisely at Q₂; the three-phase equilibrium data measured in this study were in good agreement with previous studies of the CHF₃ + water system [43-45]. In particular, the H–L_w–V equilibrium data obtained in this study are shown with those reported by Hashemi et al. [45]. All measured equilibrium data of the CHF₃ + water and C₂F₆ + water systems are given in Tables 3.1.1 and 3.1.2, respectively. It should be noted that the Q₂ of the C₂F₆ hydrate (279.5 K and 2.17 MPa) was located significantly below that of the CHF₃ hydrate (292.5 K and 4.07 MPa). Accordingly, the H–L_w–V equilibrium line of the C₂F₆ hydrate was located at limited pressure and temperature ranges compared to the CHF₃ hydrate. The hydrate phase equilibria of the CHF₃ + water and C₂F₆ + water systems can provide insights into the enclathration of these F-gases in the gas hydrate lattices on a qualitative basis. However, in order to identify the precise structure of each clathrate hydrate and to quantify the cage occupancy of the F-gases in each hydrate structure, microscopic analyses such as PXRD, NMR, and Raman spectroscopy, combined with molecular simulations, are required.



(a)



(b)

Figure 3.1.1. (a) H-L_W-V, H-L_{CHF₃}-V, L_W-L_{CHF₃}-V equilibria of the pure CHF₃ + water system.

(b) H-L_W-V, H-L_{C₂F₆}-V, L_W-L_{C₂F₆}-V equilibria of the pure C₂F₆ + water system.

Table 3.1.1. Hydrate phase equilibrium data of the CHF_3 + water system.

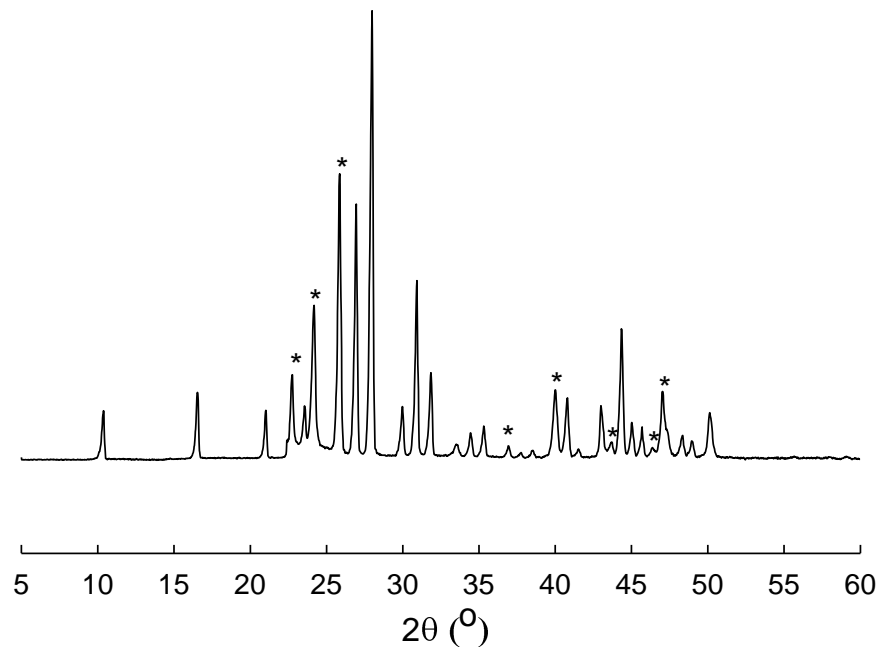
H - L _w - V		H - L _{CHF₃} - V		L _w -L _{CHF₃} -V	
T (K)	P (MPa)	T (K)	P (MPa)	T (K)	P (MPa)
283.3	1.11	282.4	3.17	293.2	4.14
285.0	1.38	283.4	3.24	294.3	4.25
286.2	1.63	284.4	3.32	295.5	4.38
287.8	2.01	285.3	3.41	296.4	4.47
289.3	2.47	286.3	3.49	297.7	4.59
290.1	2.77	287.3	3.58	299.1	4.72
291.2	3.28	288.3	3.67		
291.8	3.65	289.4	3.76	H - L _w - L _{CHF₃} - V	
		290.3	3.85	T (K)	P (MPa)
		291.3	3.95	292.5	4.07

Table 3.1.2. Hydrate phase equilibrium data of the C_2F_6 + water system.

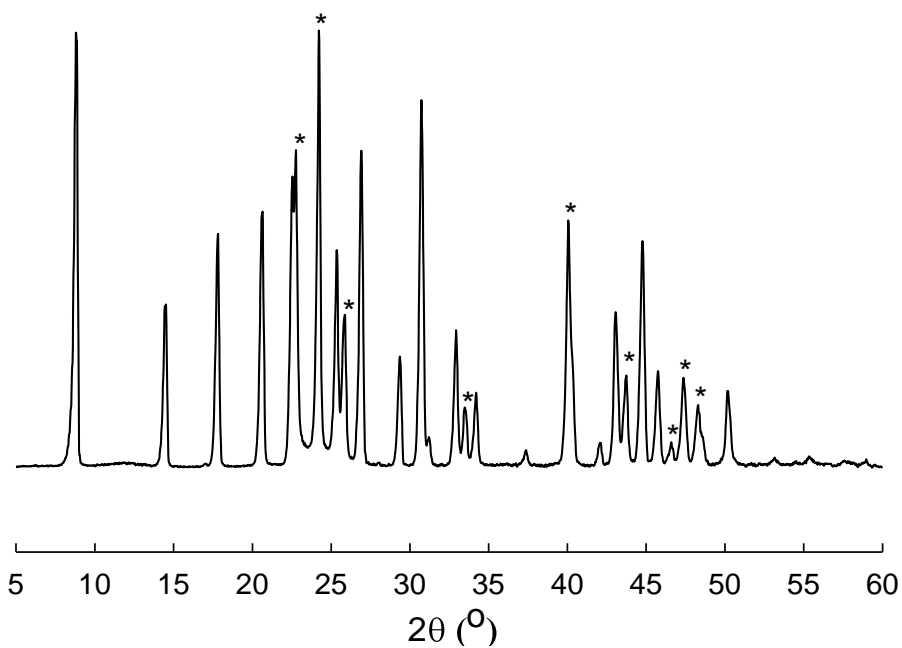
H - L _w - V		H - L _{C₂F₆} - V		L _w -L _{C₂F₆} -V	
T (K)	P (MPa)	T (K)	P (MPa)	T (K)	P (MPa)
275.3	0.58	274.7	1.91	280.5	2.23
276.9	0.95	275.7	1.96	281.6	2.29
277.4	1.11	276.6	2.01	282.6	2.35
278.3	1.43	277.6	2.06	283.6	2.41
278.6	1.57	278.6	2.13		
278.9	1.72			H - L _w - L _{C₂F₆} - V	
279.3	1.99			T (K)	P (MPa)
				279.5	2.17

3.1.3. Microscopic Analyses on Pure CHF₃ and C₂F₆ Hydrates

The structures and refined cell parameters of the pure CHF₃ and C₂F₆ hydrates were revealed through powder X-ray diffraction (PXRD). Figure 3.1.2 presents the PXRD patterns of both pure CHF₃ and C₂F₆ hydrates. The pure CHF₃ hydrate was identified as a cubic sI (*Pm3n*) with a unit cell parameter of 11.91 Å. The molecular size of CHF₃ was approximately 5.12 Å [46], which is slightly larger than the diameter of the sI small (5¹²) cages [1]. Therefore, the CHF₃ molecules were expected to primarily occupy the large (5¹²6²) cages of the sI hydrate. In contrast, the pure C₂F₆ hydrate was verified as a cubic sII (*Fd3m*) with a unit cell parameter of 17.15 Å. The C₂F₆ molecules had a molecular size of 6.1 Å [47]; thus, they were expected to only be captured in the sII large (5¹²6⁴) cages.



(a)



(b)

Figure 3.1.2. (a) PXRd patterns of the pure CHF_3 hydrate ($Pm\bar{3}n$, $a = 11.91 \text{ \AA}$).

(b) PXRd patterns of the pure C_2F_6 hydrate ($Fd\bar{3}m$, $a = 17.15 \text{ \AA}$).

Asterisks (*) indicate hexagonal ice (Ih).

The enclathration of the CHF_3 and C_2F_6 molecules in the clathrate hydrates was confirmed through the ^{13}C and ^{19}F MAS NMR spectroscopies [48]. Figure 3.3.3 (a) presents the ^{13}C spectra of the CHF_3 gas and CHF_3 hydrate measured at 240 K, which exhibit a quartet signal due to the J-coupling with the three ^{19}F nuclei. The CHF_3 gas resonated at 119.1, 116.4, 113.7, and 111.0 ppm, whereas the CHF_3 hydrate signals were significantly broadened and appeared at slightly different resonance frequencies of 119.1, 117.1, 114.8, and 111.4 ppm. Figure 3.3.3 (b) illustrates the ^{19}F spectra of CHF_3 gas and CHF_3 hydrate measured at 240 K, and it also exhibits a doublet at -88.4 and -88.6 ppm due to the J-coupling with a ^1H nucleus. It should be noted that both ^{13}C and ^{19}F spectra of the CHF_3 molecules enclathrated in the hydrates exhibited broader resonance peaks than the gaseous CHF_3 molecules. The broader line-widths indicate a nanoscopic heterogeneous environment for the CHF_3 molecules enclathrated in the hydrates and/or the reduction of molecular motion, which indicates the enclathration of the CHF_3 molecules in the hydrate cages. The broader line-widths obscure the accuracy of the chemical shifts and result in the poorer spectral resolution. This makes it difficult to distinguish the CHF_3 molecules in the cages in different sizes if the chemical shift difference between them is smaller than the line-widths. Figure 3.3.4 (a) and (b) present the ^{13}C and ^{19}F spectra of the C_2F_6 molecules in both gas and hydrate phases. The ^{13}C spectra in Figure 3.3.4 (a) exhibited a quartet at 119.6, 116.8, 114.0, and 111.3 ppm due to the J-coupling to the three ^{19}F nuclei directly bonded to the observed ^{13}C in the C_2F_6 hydrate, and each peak of the quartet was split into a quartet due to the J-coupling to the three ^{19}F nuclei bonded to the neighboring carbon. Similar to the ^{13}C spectra of CHF_3 , the ^{13}C spectra of the C_2F_6 hydrate demonstrated slight peak shifts and broadened peak shapes compared with those of the C_2F_6 gas due to the nanoscopic heterogeneous environment for the C_2F_6 molecules enclathrated in the hydrates and/or the reduction of the molecular motion, which confirmed the enclathration of the C_2F_6 molecules in the clathrate hydrates. The distortion of the peak intensity and chemical shifts was more evident in the ^{13}C spectra for the CHF_3 hydrates, which indicates the contribution of dipolar interactions with the protons and more easily broken molecular symmetry of CHF_3 in the hydrate. The ^{19}F spectra presented in Fig. 3.3.4 (b) also confirmed the capture of the C_2F_6 molecules in the clathrate hydrate phase with the presence of one broader peak than that of the C_2F_6 gas but at the same chemical shift of -97.7 ppm for the C_2F_6 gas.

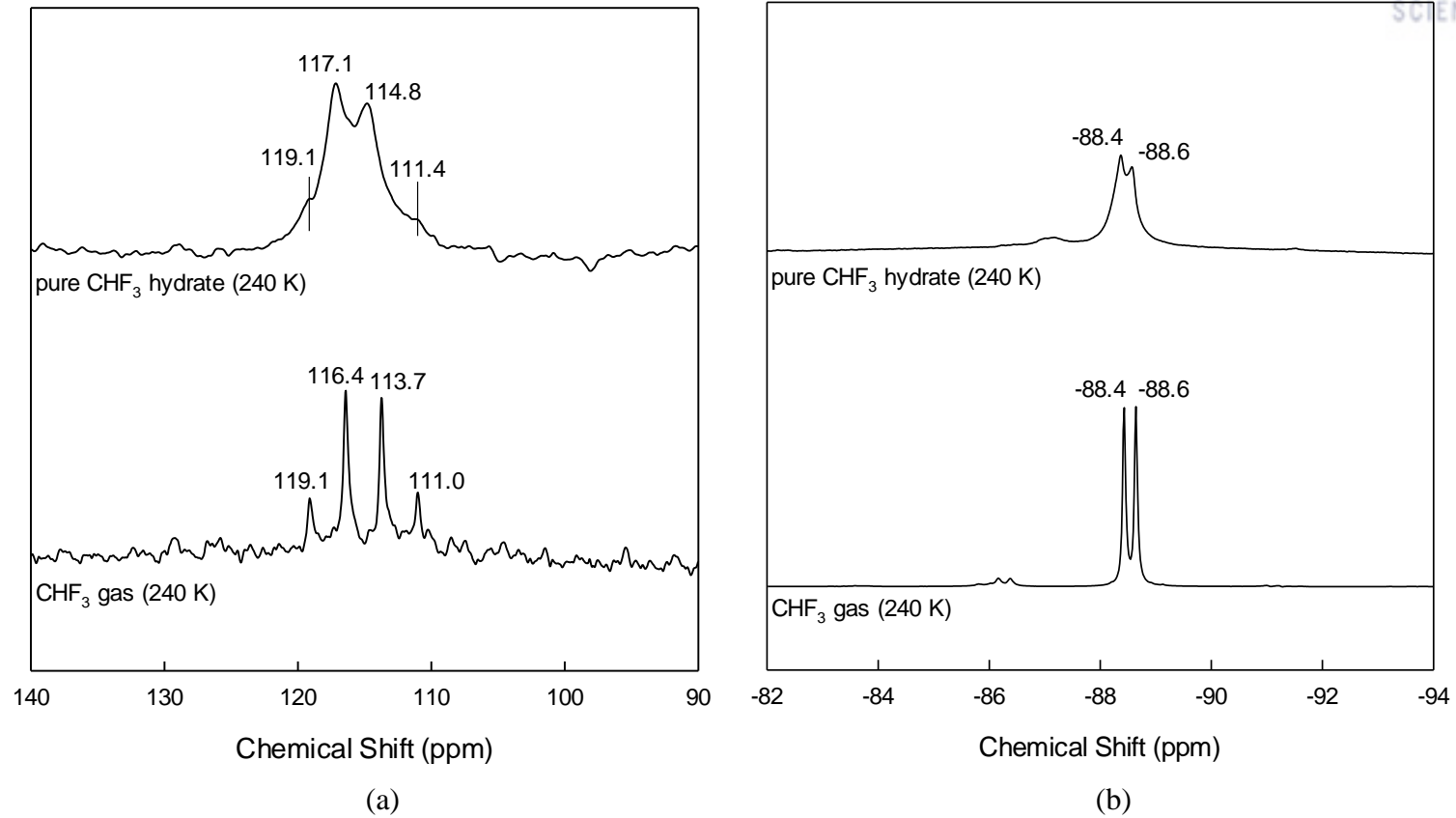


Figure 3.1.3. (a) ^{13}C MAS NMR spectra of CHF_3 gas and pure CHF_3 hydrate at 240 K.
 (b) ^{19}F MAS NMR spectra of CHF_3 gas and pure CHF_3 hydrate at 240 K.

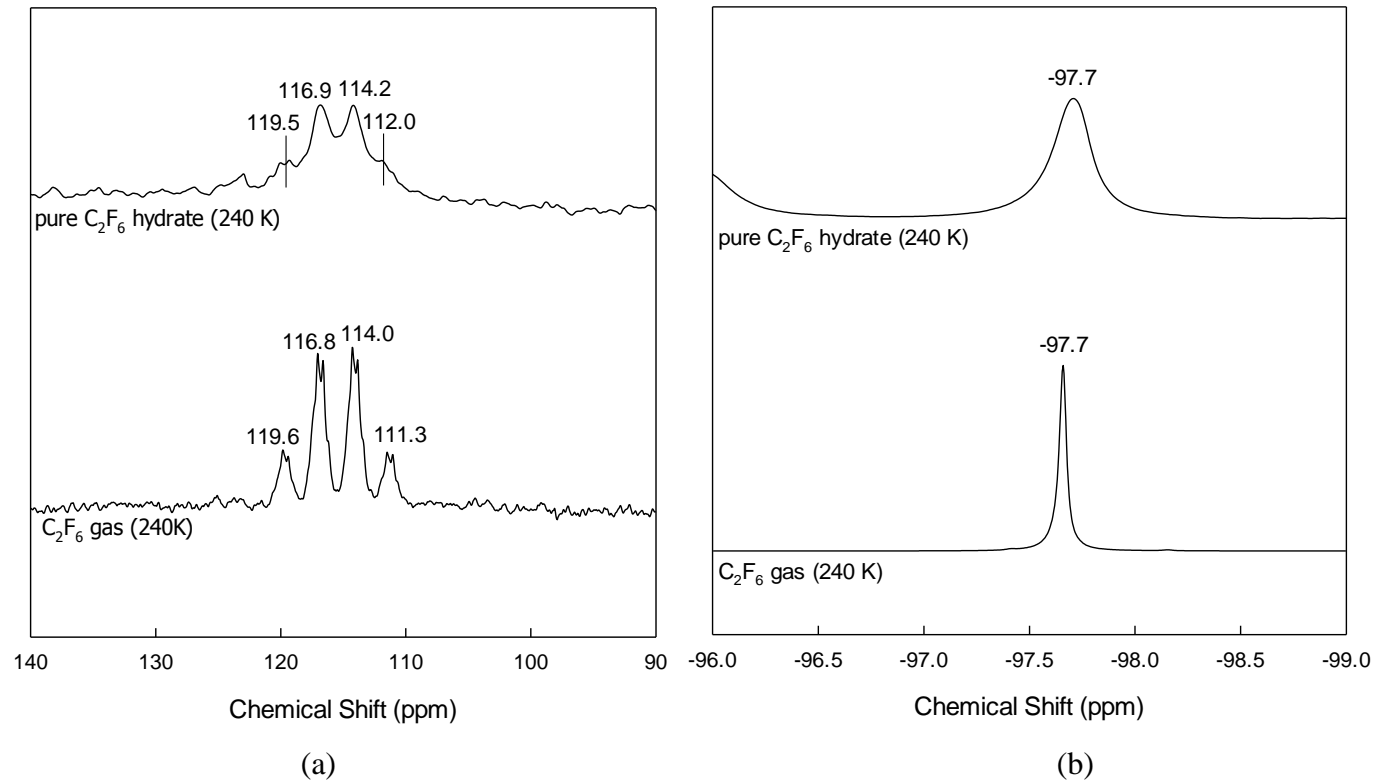


Figure 3.1.4. (a) ^{13}C MAS NMR spectra of C_2F_6 gas and pure C_2F_6 hydrate at 240 K.

(b) ^{19}F MAS NMR spectra of C_2F_6 gas and pure C_2F_6 hydrate at 240 K.

In order to further investigate the hydrate formation process and enclathration of the F-gas molecules, in situ Raman spectroscopy was used for the CHF₃ hydrate. Because some Raman peaks from CHF₃ overlapped with those from H₂O, D₂O was used to obtain the precise Raman peaks of the C-H stretching mode for the enclathrated CHF₃ molecules [49, 50]. Fig. 3.3.5 (a) presents the real-time Raman spectra for the C-H stretching mode of the CHF₃ molecules enclathrated in the hydrate cages that consist of D₂O molecules. After the completion of the CHF₃ hydrate formation, the final Raman spectrum for the C-H stretching mode is depicted in Fig. 3.3.5 (b). The C-H symmetric stretching mode of the gaseous CHF₃ was reported to exhibit one Raman peak at 3036 cm⁻¹ [51]. However, the C-H symmetric stretching mode of the enclathrated CHF₃ in the hydrate cages exhibited two Raman peaks: one large peak at 3038 cm⁻¹ and one small peak at 3059 cm⁻¹.

In order to examine the cage filling characteristics of the pure CHF₃ hydrate, the Raman spectrum range from 3000 cm⁻¹ to 3100 cm⁻¹ was deconvoluted using a Voigt function. As indicated by Uchida et al. [49, 50], the large peak at 3038 cm⁻¹ can be assigned to the CHF₃ molecules captured in the sI large (5¹²6²) cages, while the small peak at 3059 cm⁻¹ can be assigned to the CHF₃ molecules in the sI small (5¹²) cages. There has been controversy surrounding the occupation of the CHF₃ molecules in the sI small (5¹²) cages because the molecular size of CHF₃ is slightly larger than the diameter of the sI small (5¹²) cages [1, 46, 49, 50, 52]. However, the Raman spectrum in Fig. 3.3.5 (b) clearly demonstrates that the CHF₃ molecules are enclathrated in the small (5¹²) cages as well as in the large (5¹²6²) cages of the sI hydrate. After the deconvolution of the Raman spectrum, the area ratio of the CHF₃ molecules in the large (5¹²6²) and small (5¹²) cages (A_L/A_S) of the pure CHF₃ hydrate was 20.1 ± 1.8 , which is equivalent to the cage occupancy ratio (θ_L/θ_S) of 6.7 ± 0.6 . The Raman spectra presented in Fig. 3.3.5 (a) and (b) clearly indicate that the CHF₃ molecules can also occupy the small (5¹²) cages of the sI hydrate, even though their cage occupancy in the sI small (5¹²) cages is significantly lower than that in the sI large (5¹²6⁴) cages.

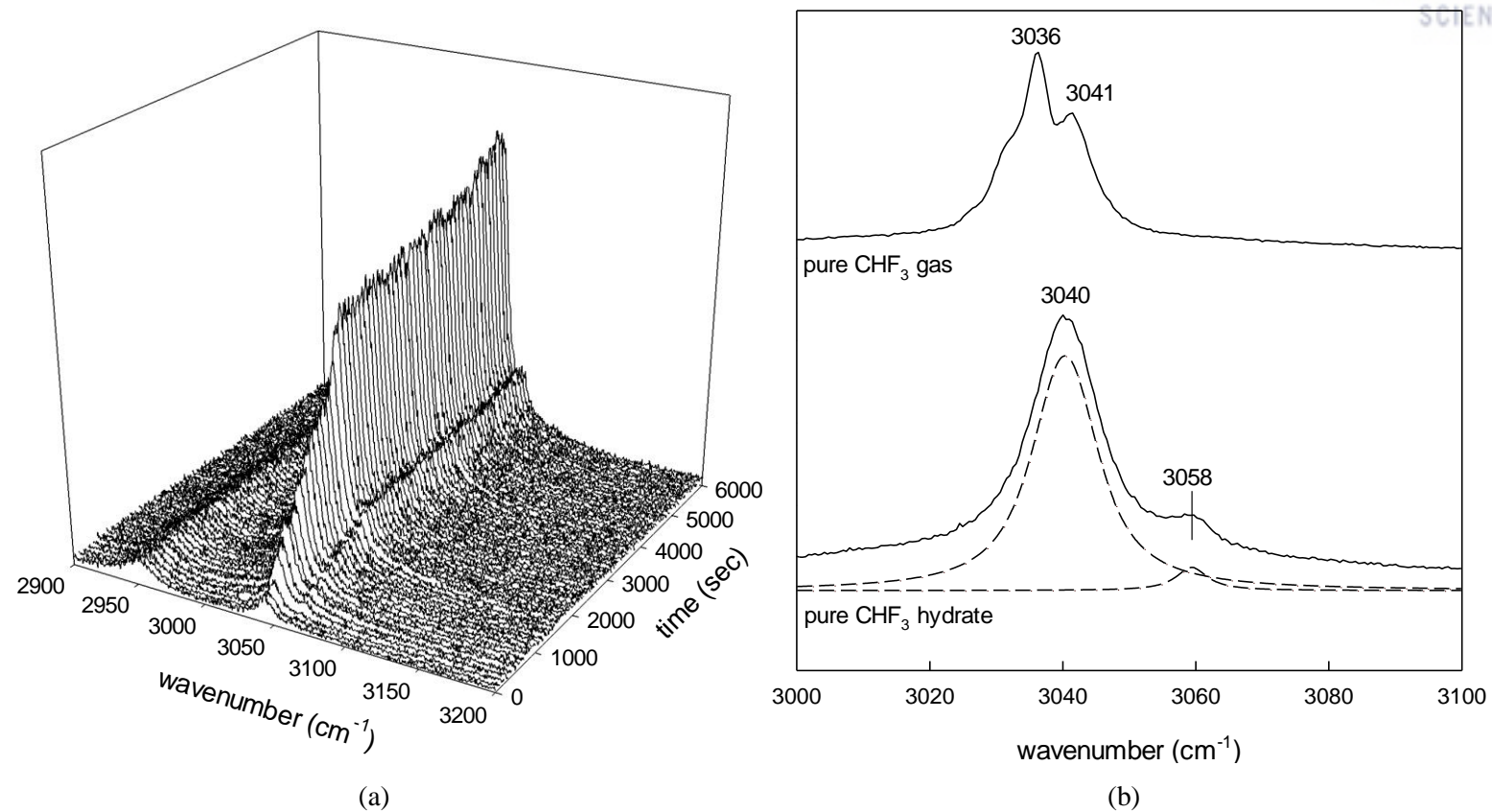


Figure 3.1.5. (a) Real-time Raman spectra for the C-H stretching mode of pure CHF₃ hydrate at 278.15 K and 2.5 MPa.

(b) Final Raman spectrum of the C-H stretching mode for pure CHF₃ hydrate.

3.1.4. Computational Methods and Results

The water frameworks were extracted from the gas hydrate structures [53]. In order for the density functional theory (DFT) calculation to obtain the optimized water structures, the unit cell systems were used: a cubic structure for the sI hydrate and a rhombohedral structure for the sII hydrate (Figure 3.1.6), which consisted of 46 and 34 water molecules, respectively. In order to predict the enclathration of the gas molecules, water-cluster models from the optimized unit cells were used. In order for the grand canonical Monte Carlo (GCMC) simulations to estimate the occupancies in the sI and sII hydrates, the unit cells were extended to the supercell systems of $3 \times 3 \times 3$, which consisted of 54 small cages (5^{12}) and 162 large cages ($5^{12}6^2$) for the sI hydrate, and 108 small cages (5^{12}) and 54 large cages ($5^{12}6^4$) for the sII hydrate. In particular, for the GCMC study, the lattice parameters of the optimized sI and sII hydrates were adjusted based on the experimental lattice parameters.

The unit cells of the hydrate structures were optimized using a quantum mechanical calculation package CASTEP [54, 55] with generalized gradient approximations (GGA) – the Perdew-Burke-Ernzerhof (PBE) functional [56] and on-the-fly pseudopotential. The energy cut-off was set to 610.0 eV with a $2 \times 2 \times 2$ k-point grid. The Mulliken partial charges for atoms were obtained from the population analysis. In order to observe the enclathration of CHF_3 and C_2F_6 in the water-cluster models, DMol3 [57, 58] with the GGA-PBE functional was used. Spin-polarization was adopted with a basis set of DNP 4.4 level. In order to predict the cage occupancies of CHF_3 and C_2F_6 in the sI and sII hydrates, the GCMC simulations using Metropolis [59] and configurational-bias [60] algorithms was performed through applying the COMPASS force field [61] to the enclathrated systems. According to the data of the hydrate phase equilibria from the experiment, the thermodynamic conditions were set to 287.8 K and 2.01 MPa for the sI hydrate and 278.6 K and 1.57 MPa for the sII hydrate. All GCMC simulations were conducted five times in order to produce averaged results. Each simulation consisted of an equilibration of 107 Monte Carlo (MC) steps and a production of 107 MC steps.

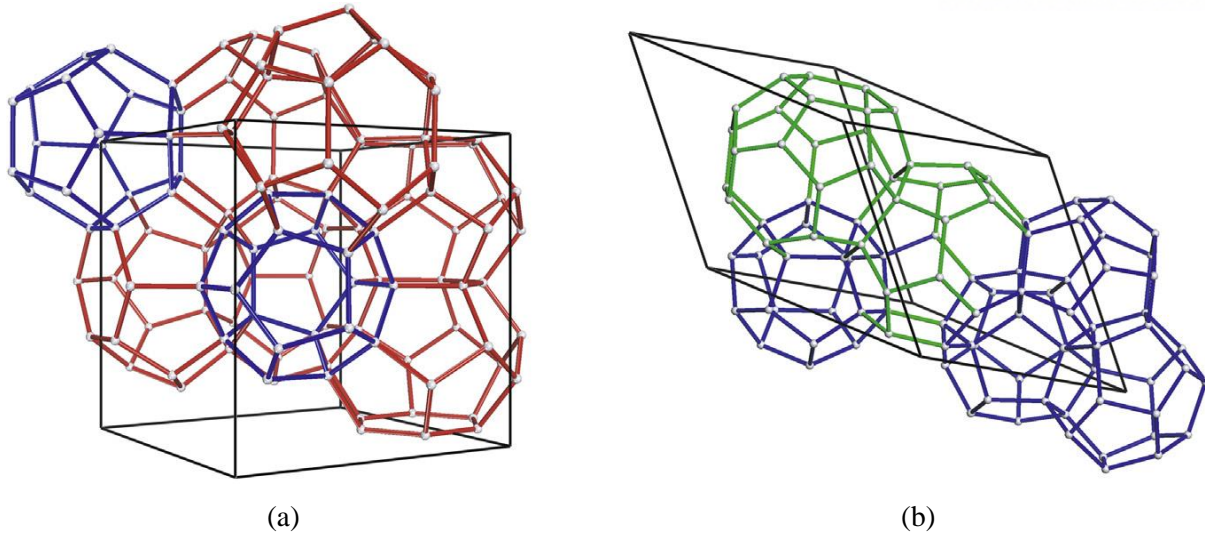


Figure 3.1.6. Optimized structures for unit cells of (a) sI hydrate (cubic) and (b) sII hydrate (rhombohedral).

In sI hydrate, there are 6 large cages ($5^{12}6^2$) and 2 small cages (5^{12}) indicated by red and blue colors, respectively. In sII hydrate, there are 2 large cages ($5^{12}6^4$) and 4 small cages (5^{12}) indicated by green and blue colors, respectively. White spheres indicate oxygen atoms. (For interpretation of the references to colour in this figure legend, the reader is referred to the web version of this article.)

Before estimating the occupancies of the CHF_3 gas hydrate, the possibility of enclathrating CHF_3 and C_2F_6 in the hydrate cages was first investigated using DFT calculations (Fig. 3.1.7). The CHF_3 molecules were occupied in both the small (5^{12}) and large ($5^{12}6^2$) cages of sI. However, the C_2F_6 molecules were only encaged in the large ($5^{12}6^4$) cages of sII because the occupation of the C_2F_6 molecules in the small (5^{12}) cages could break the hydrogen bonding of the water molecules due to their large molecular size (Fig. 3.1.7 (d)). Due to the enclathration of the guest molecules, the expansion of the cages caused enlargement of the lattice parameter of the gas hydrates. The order of expansion agreed well with experimental results: the large ($5^{12}6^2$) cage of the empty sI hydrate expanded by approximately 3%, which resulted in the enlargement of the lattice parameter from 11.56 Å to 11.90 Å (i.e. similar to 11.91 Å from the experiment) and the large ($5^{12}6^4$) cage of the empty sII hydrate expanded by approximately 2%, which resulted in the enlargement of the lattice parameter from 11.89 Å to 12.13 Å, which is equivalent to 17.15 Å of the unit cell in the cubic sII hydrate (i.e. similar to 17.15 Å from the experiment). The enlarged lattice parameters were used in the GCMC simulation to estimate the occupancies of the guest molecules. As described in Table 3.1.3, CHF_3 occupied 12% of the small (5^{12}) cages and 100% of the large ($5^{12}6^2$) cages of the sI hydrate, whereas C_2F_6 could not occupy the small (5^{12}) cages, but occupied 97.6% of the large ($5^{12}6^4$) cage of the sII hydrate. The occupancy ratio (θ_L/θ_S) of CHF_3 was estimated to be 8.3 ± 1.4 , which was comparable with the experimental result. The nonbonding interaction energies (i.e. van der Waals and electrostatic energies) between the gas molecules and relaxed water framework were calculated in order to elucidate the results of the disproportional occupancies (i.e. θ_S in sI and θ_L in sII). Fig. 3.1.8 (a) presents the interaction energies of the CHF_3 molecules in the sI hydrate in terms of θ_S . Note that the energy was calculated through maintaining θ_L as unity. The sI hydrate system was favored in the range of $\theta_S = 0.08$ – 0.16 , which corresponded to the average occupancy (i.e. 0.12). Fig. 3.1.8 (b) presents the interaction energies of C_2F_6 , which decreased constantly as θ_L increased until it reached 0.976. As seen in the energy trend, the 100% occupancy for C_2F_6 in the large ($5^{12}6^4$) cage was expected, but the maximum occupancy was estimated to be 97.6% with the current GCMC scheme based on the random insertion.

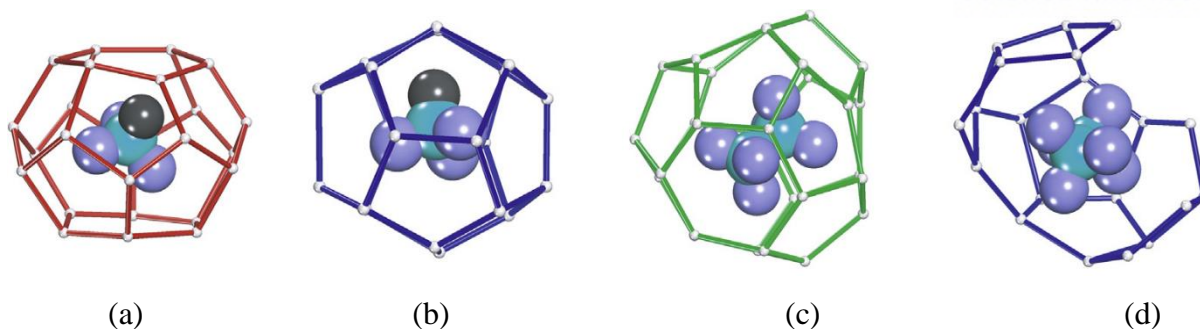


Figure 3.1.7. Optimized structure for CHF_3 and C_2F_6 hydrate cage by DFT calculations. .
 (a) and (b) represent CHF_3 in large ($5^{12}6^2$) and small cages (5^{12}) of sI hydrate, respectively.
 (c) and (d) represent C_2F_6 in large ($5^{12}6^4$) and small (5^{12}) cages of sII hydrate, respectively. Black, cyan, and light purple colors represent hydrogen, carbon, and fluorine atoms, respectively. (For interpretation of the references to colour in this figure legend, the reader is referred to the web version of this article.)

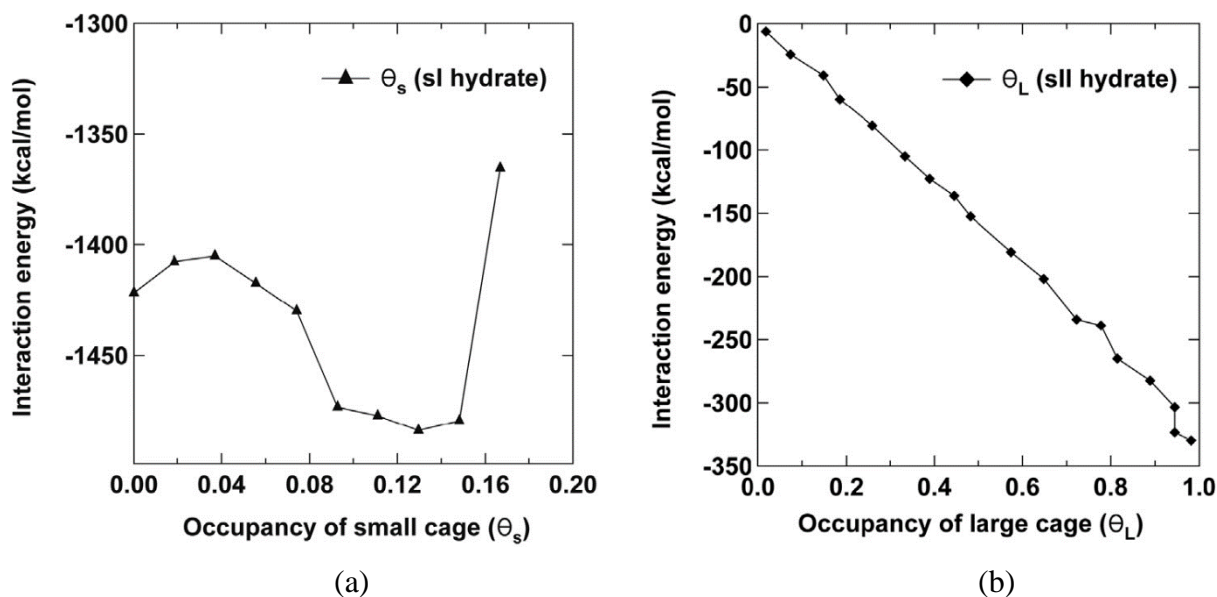


Figure 3.1.8. Interaction energies (kcal/mol) in terms of (a) the occupancy of small cage (5^{12}) of CHF_3 in sI hydrate and (b) the occupancy of large cage ($5^{12}6^4$) of C_2F_6 in sII hydrate.

Table 3.1.3. Occupancies of gas molecules for small and large cages in sI and sII hydrates of the (3 × 3 × 3) supercell system. The numbers in parentheses represent average numbers of enclathrated gas molecules over the total number of each cage in sI and sII hydrates, respectively.

Type	Occupancy for small cages (θ_s)	Occupancy for large cages (θ_L)
sI	0.12 ± 0.02 ((6.4 ± 1.14)/54)	1.000 (162/162)
sII	0.0 (0/108)	0.976 ± 0.01 ((52.7 ± 0.58)/54)

3.1.5. Conclusions

In this study, the thermodynamic, structural, and cage filling characteristics of pure CHF₃ and C₂F₆ hydrates were investigated as a first step in the hydrate-based F-gas separation. The three phase (H–L_W–V, H–L_W–L_{F-gas}, and L_W–L_{F-gas}–V) equilibria measurements demonstrated that both pure CHF₃ and C₂F₆ hydrates provided relatively mild hydrate forming conditions, which implies that both CHF₃ and C₂F₆ molecules can be readily captured in the hydrate lattices. The PXRD analyses revealed that the pure CHF₃ hydrate was sI (*Pm3n*) with a lattice parameter of 11.91 Å, whereas the pure C₂F₆ hydrate was sII (*Fd3m*) with a lattice parameter of 17.15 Å.

The ¹³C and ¹⁹F NMR spectroscopic results confirmed the enclathration of the CHF₃ and C₂F₆ molecules in each hydrate structure through the resonance peak shift and broadening of the guest molecules enclathrated in the hydrate phase. The time-dependent growth process of the CHF₃ hydrate was monitored via in situ Raman spectroscopy. The deconvolution of the final Raman spectrum of the CHF₃ hydrate revealed that the cage occupancy ratio (θ_L/θ_S) of the CHF₃ molecules in the large (5¹²6²) and small (5¹²) cages of sI was 6.7 ± 0.6 , even though the molecular size of CHF₃ was almost the same as, or slightly larger than, that of the small (5¹²) cages of the sI hydrate. The cage filling behavior of CHF₃ and C₂F₆ was also predicted by the DFT calculations, which demonstrated that CHF₃ could be captured in the small (5¹²) and large (5¹²6²) cages of the sI hydrate, whereas C₂F₆ was only enclathrated in the large (5¹²6⁴) cages of the sII hydrate. Furthermore, the GCMC simulations revealed that the cage occupancy ratio (θ_L/θ_S) of CHF₃ in the sI hydrate was 8.3 ± 1.4 , which was in good agreement with the experimental result. The experimental and computational results including the phase behavior, structure identification, and cage-specific guest distribution clearly demonstrated the enclathration of both CHF₃ and C₂F₆ molecules in the gas hydrate lattices; thus, this indicates significant potential for hydrate-based F-gas separation.

3.2. Gas Hydrate-based CHF₃ Separation from CHF₃ + N₂ Mixture Gas

3.2.1. Abstract

In this study, the feasibility of gas hydrate-based greenhouse gas (CHF₃) separation was investigated with a primary focus on thermodynamic, structural, and cage-filling characteristics of CHF₃ + N₂ hydrates. The three-phase (hydrate (H)–liquid water (L_w)–vapor (V)) equilibria of CHF₃ (10%, 20%, 40%, 60%, and 80%) + N₂ + water systems provided the thermodynamic stability conditions of CHF₃ + N₂ hydrates. Powder X-ray diffraction revealed that the structure of the CHF₃ + N₂ hydrates was identified as sI (*Pm3n*) for all the CHF₃ concentration ranges considered in this study. A pressure–composition diagram obtained at two different temperature conditions (279.15 and 283.15 K) demonstrated that 40% CHF₃ could be enriched to 88% CHF₃ by only one step of hydrate formation and that separation efficiency was higher at the lower temperature. Furthermore, Raman spectroscopy revealed that CHF₃ molecules preferentially occupy large (5¹²6²) cages of the structure I (sI) hydrate during CHF₃ + N₂ hydrate formation. The overall experimental results clearly demonstrated that the hydrate-based separation process can offer highly concentrated CHF₃ and would be more effective for recovering CHF₃ from exhaust gas when it constitutes a hybrid system with existing separation methods.

3.2.2. Thermodynamic Phase Equilibria

Because the main purpose of this study is to suggest a novel method to separate CHF_3 by forming gas hydrate from $\text{CHF}_3 + \text{N}_2$ gas mixtures, which are usually emitted from semiconductor industries, the thermodynamic validity of the gas hydrate-based separation process should be verified first. Therefore, the three-phase (H-L_w-V) equilibria of the $\text{CHF}_3 + \text{N}_2 + \text{water}$ systems with various CHF_3 concentrations (10%, 20%, 40%, 60%, and 80%) in the temperature range of 275–289 K and pressure range of 0.7–11.5 MPa were measured, and the results are presented in Figure 3.2.1 and Table 3.2.1. Also, the H-L_w-V equilibrium data of pure CHF_3 hydrate, which were measured in our previous study, and those of pure N_2 hydrate are also presented in Figure 3.2.1 to examine the effect of CHF_3 concentrations on the thermodynamic stability of the $\text{CHF}_3 + \text{N}_2$ gas hydrates [62, 63]. As shown in Figure 3.2.1, the H-L_w-V equilibrium curves of the $\text{CHF}_3 + \text{N}_2 + \text{water}$ systems were located generally nearer to that of the $\text{CHF}_3 + \text{water}$ system than that of the $\text{N}_2 + \text{water}$ system. This is because N_2 forms the sII hydrate at very high pressure conditions, occupying both small (5^{12}) and large ($5^{12}6^4$) cages, due to its small molecular size, whereas CHF_3 forms the sI hydrate, primarily occupying large ($5^{12}6^2$) cages and partly occupying small (5^{12}) cages [48-50, 62, 63]. Therefore, as the CHF_3 concentration in the vapor phase increased, the H-L_w-V equilibria of the $\text{CHF}_3 + \text{N}_2 + \text{water}$ systems became thermodynamically more stable as a result of the increased enclathration of a large-sized molecular guest (CHF_3). The extremely large equilibrium pressure difference between pure N_2 hydrate and pure CHF_3 hydrate and the significant equilibrium line shift of the $\text{CHF}_3 + \text{N}_2$ hydrates to the stabilized regions with an increase in the CHF_3 concentration, as shown in Figure 3.2.1, imply that CHF_3 molecules can be selectively captured in the hydrate phase and, thus, can be separated from the gas mixture through gas hydrate formation.

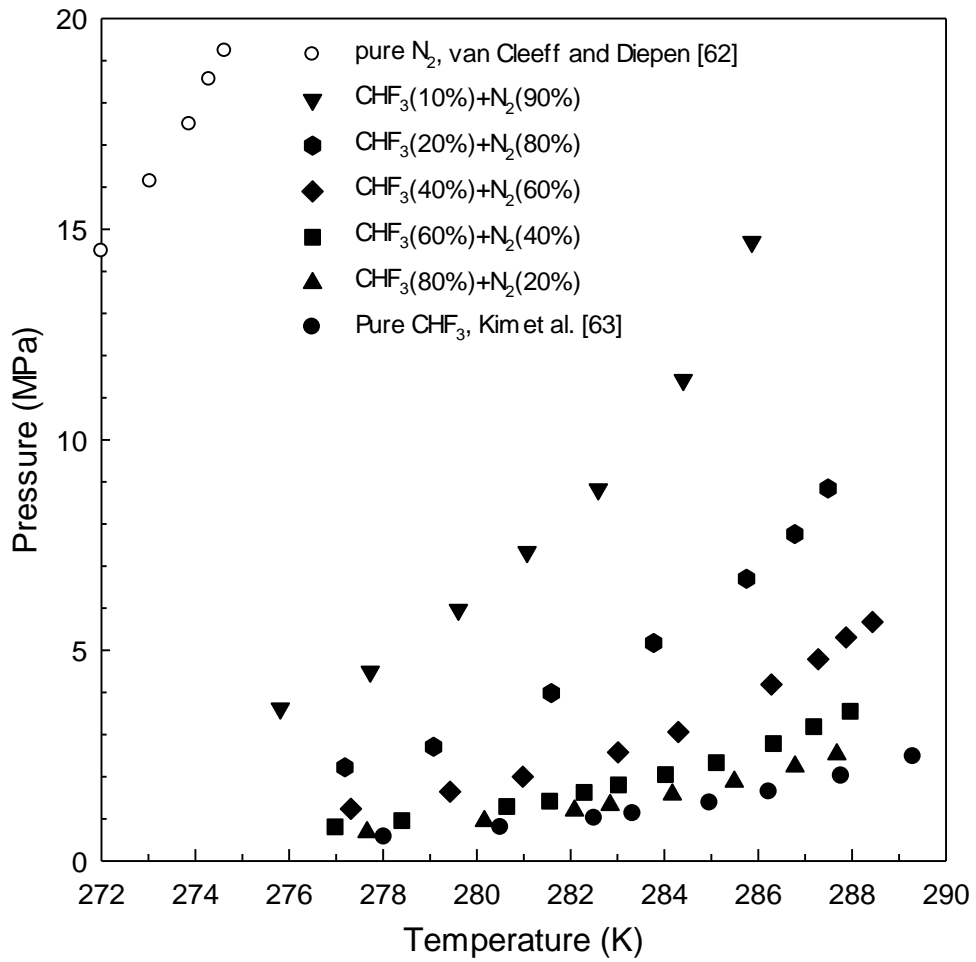


Figure 3.2.1. Hydrate phase equilibria of $\text{CHF}_3 + \text{N}_2 + \text{water}$ mixtures.

Table 3.2.1. Hydrate phase equilibrium data of the $\text{CHF}_3 + \text{N}_2 + \text{water}$ system.

CHF_3 (80%) + N_2		CHF_3 (60%) + N_2		CHF_3 (40%) + N_2		CHF_3 (20%) + N_2		CHF_3 (10%) + N_2	
T (K)	P (MPa)	T (K)	P (MPa)	T (K)	P (MPa)	T (K)	P (MPa)	T (K)	P (MPa)
277.7	0.68	277.0	0.81	277.3	1.24	277.2	2.22	275.8	3.62
280.2	0.95	278.4	0.96	279.4	1.64	279.1	2.71	277.7	4.49
282.1	1.20	280.6	1.29	281.0	2.00	281.6	3.99	279.6	5.96
282.8	1.33	281.6	1.42	283.0	2.58	283.8	5.17	281.1	7.33
284.2	1.58	282.3	1.63	284.3	3.06	285.8	6.70	282.6	8.82
285.5	1.88	283.0	1.80	286.3	4.19	286.8	7.76	284.4	11.42
286.8	2.24	284.0	2.05	287.3	4.79	287.5	8.84	285.9	14.70
287.7	2.53	285.1	2.33	287.9	5.31				
		286.3	2.79	288.4	5.67				
		287.2	3.19						
		288.0	3.55						

3.2.3. Thermodynamic and Kinetic Examination on Separation Efficiency

In order to examine the separation efficiency of the hydrate-based method, a pressure–composition diagram of the $\text{CHF}_3 + \text{N}_2$ hydrates at 279.15 and 283.15 K is presented in Figure 3.2.3. For equilibrium composition measurements of the vapor and hydrate phases, the experiment was conducted in the presence of excess water in order to create the three-phase (H–L_w–V) equilibrium state when the hydrate formation process was completed. At the final equilibrium state, there exist three phases (hydrate (H), liquid water (L_w), and vapor (V)) and three components (CHF_3 , N_2 , and water), and accordingly, the number of degrees of freedom for this system becomes two. Therefore, the equilibrium compositions of the vapor and hydrate phases are automatically determined depending on the pressure condition at a specific temperature. It should be noted that the vapor phase compositions in Figure 3.2.3 can also be roughly estimated from the hydrate phase equilibrium lines of the $\text{CHF}_3 + \text{N}_2 + \text{water}$ mixtures depicted in Figure 3.2.1 because the pressure–composition diagram in Figure 3.2.3 was obtained on the basis of the three-phase (H–L_w–V) equilibrium states. Figure 3.2.3, which presents CHF_3 compositions of both vapor and hydrate phases according to the pressure conditions at a specific temperatures, can also provide the number of steps required for the desired CHF_3 concentration through the hydrate-based CHF_3 separation process. For example, at 279.15 K, a gas mixture having 40% CHF_3 can form gas hydrates at 1.7 MPa, and the corresponding hydrate phase will contain 88% CHF_3 . Furthermore, one additional step of hydrate formation at a much lower pressure will provide almost pure CHF_3 . It was also found from the pressure–composition diagram that the higher CHF_3 separation efficiency was achievable at a lower temperature.

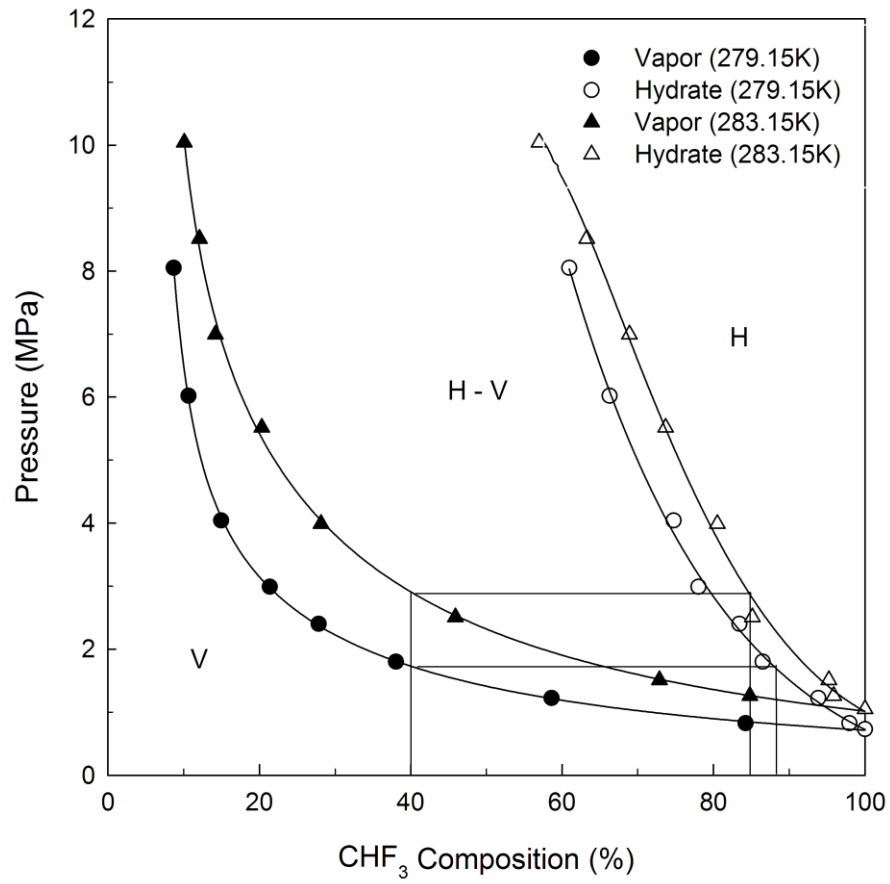


Figure 3.2.3. Pressure-composition diagram of $\text{CHF}_3 + \text{N}_2$ hydrates at 279.15 K and 283.15 K.^b

^bStandard uncertainties u are $u(\text{composition}) = 0.3 \%$ and $u(P) = 0.02 \text{ MPa}$.

Measurements for gas uptake and compositional change in the vapor phase were performed under isobaric conditions (2.5 MPa ($\Delta P = 1.0$ MPa) and 3.5 MPa ($\Delta P = 2.0$ MPa)) at a fixed temperature (279.15 K), using a CHF_3 (40%) + N_2 (60%) gas mixture, in order to observe the kinetic behavior of the $\text{CHF}_3 + \text{N}_2$ hydrates, which can be one of the important process factors that needs to be considered for the actual process. Gas uptake during the formation process of the $\text{CHF}_3 + \text{N}_2$ hydrate is shown in Figure 3.2.4. The accumulated amount of gas consumed during $\text{CHF}_3 + \text{N}_2$ hydrate formation is expected to be equivalent to the total amount of gas captured in the hydrate phase. As shown in Figure 3.2.4, the rate of gas consumption during gas hydrate formation was significantly higher at 3.5 MPa than at 2.5 MPa. A higher driving force induced a higher rate of hydrate growth and a larger gas uptake during gas hydrate formation.

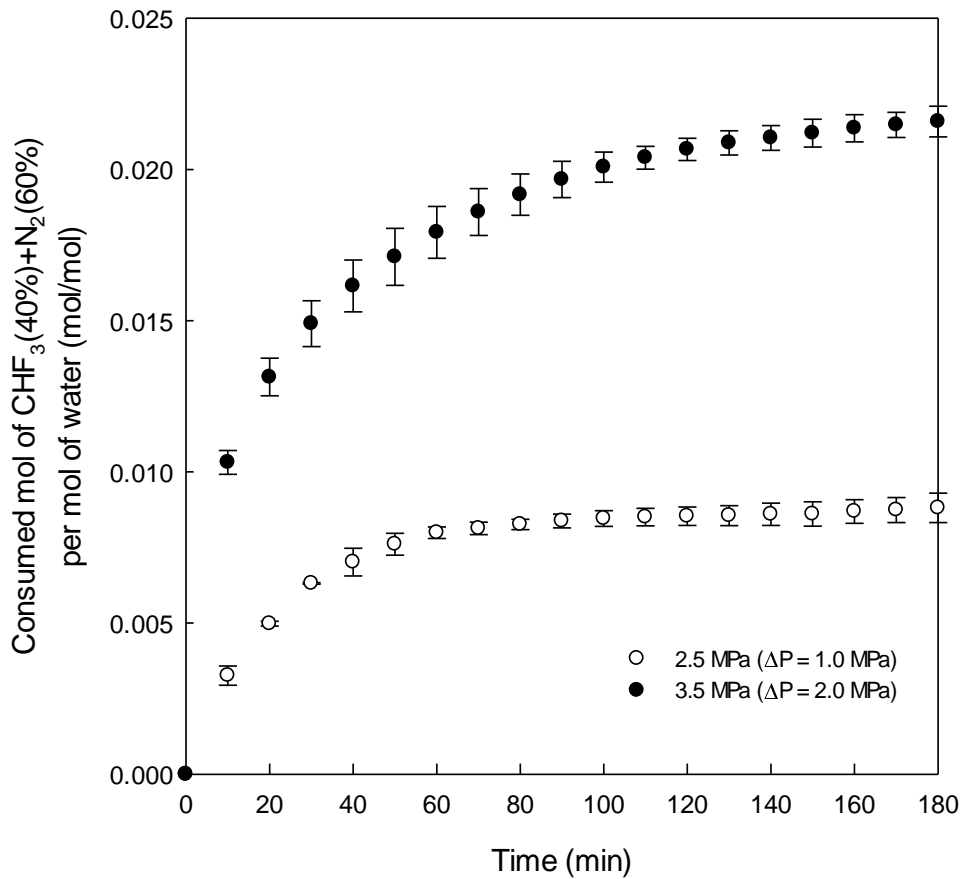


Figure 3.2.4. Gas uptake for two different pressure conditions (2.5 and 3.5 MPa) during CHF_3 (40%) + N_2 (60%) hydrate formation at 279.15 K.

Figure 3.2.5 shows the CHF₃ concentration changes in the vapor phase during gas hydrate formation at two different pressure conditions (2.5 and 3.5 MPa) at 279.15 K. The two systems with an initial vapor composition of 40% CHF₃ diverged into two different final vapor compositions depending on pressure conditions (2.5 and 3.5 MPa). As can be expected from Figure 3.2.4, a lower final CHF₃ vapor composition and a higher rate of vapor composition change were observed at a higher pressure condition. The final CHF₃ compositions at given pressure and temperature conditions shown in Figure 3.2.5 were in good agreement with those that were estimated from the phase equilibrium curves of the CHF₃ + N₂ hydrates depicted in Figure 3.2.1. Figures 3.2.4 and 3.2.5 indicated that a higher pressure driving force for hydrate formation leads to a higher hydrate growth rate at the initial stage, larger gas uptake, and higher conversion of water into gas hydrate. They also demonstrated that the hydrate formation process of the CHF₃ (40%) + N₂ (60%) hydrate is generally completed within 100 min.

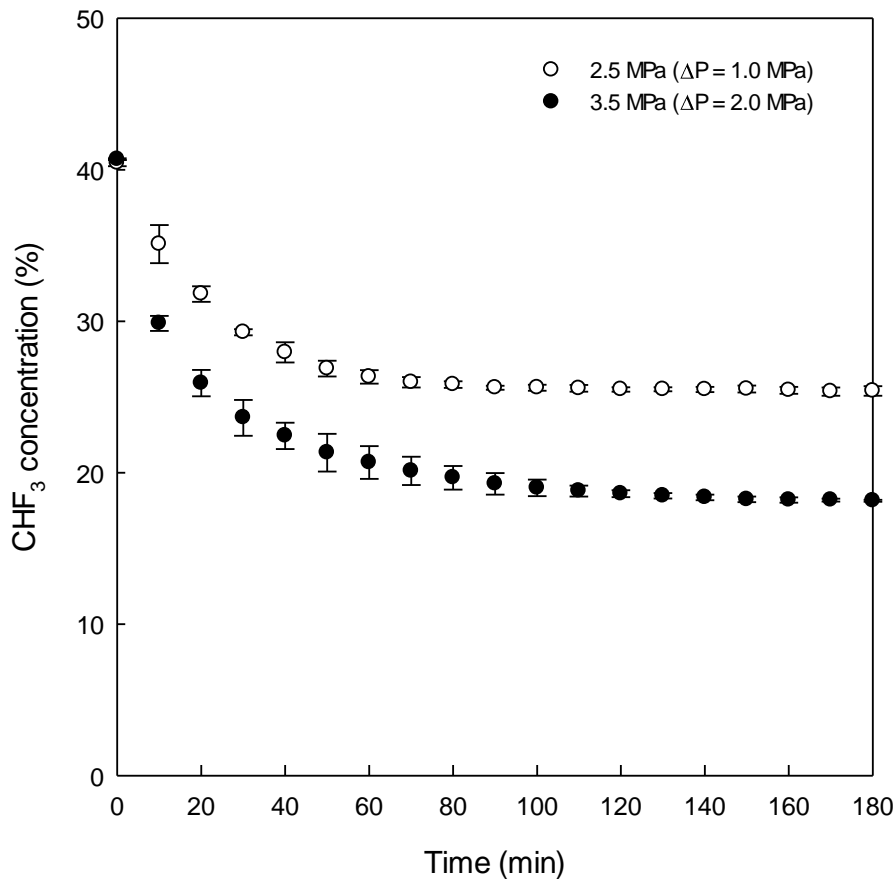


Figure 3.2.5. Composition change in the vapor phase for two different pressure conditions (2.5 and 3.5 MPa) during CHF₃ (40%) + N₂ (60%) hydrate formation at 279.15 K.

3.2.4. Crystal Structures and Cage-filling Characteristics of CHF₃ + N₂ Hydrates

The hydrate crystal structures and unit cell parameters of the CHF₃ + N₂ hydrates with various CHF₃ concentrations (10%, 20%, 40%, 60%, and 80%) were determined using PXRD. The PXRD patterns of the CHF₃ + N₂ hydrates, as well as the pure CHF₃ hydrate, are presented in Figure 3.2.2. In our previous study, the structure of pure CHF₃ hydrate was revealed as sI (*Pm3n*), with a unit cell parameter of 11.91 Å, whereas pure N₂ hydrate is known to form the sII (*Fd3m*) hydrate [1, 63]. All CHF₃ + N₂ hydrates considered in this study were identified as sI (*Pm3n*) hydrates with lattice parameters of 11.91 Å (CHF₃ 80%), 11.90 Å (CHF₃ 60%), 11.87 Å (CHF₃ 40%), 11.87 Å (CHF₃ 20%), and 11.87 Å (CHF₃ 10%). The sI hydrate formation of the CHF₃ + N₂ gas mixtures, even at low CHF₃ concentrations, is attributable to the preferential occupation of CHF₃ molecules in the hydrate phase. CHF₃ molecules are more selective guests of the hydrate cages than N₂ molecules and prefer large (5¹²6²) cages to small (5¹²) cages in the sI hydrate due to their relatively large molecular size. Therefore, they can dominate the structure of the CHF₃ + N₂ hydrates even at low CHF₃ concentrations. Also, the lattice parameters of the CHF₃ + N₂ hydrates slightly decreased as the CHF₃ concentration decreased, which can be explained by the decreased cage occupancy of CHF₃ in the small (5¹²) cages of the sI hydrate at a lower CHF₃ concentration.

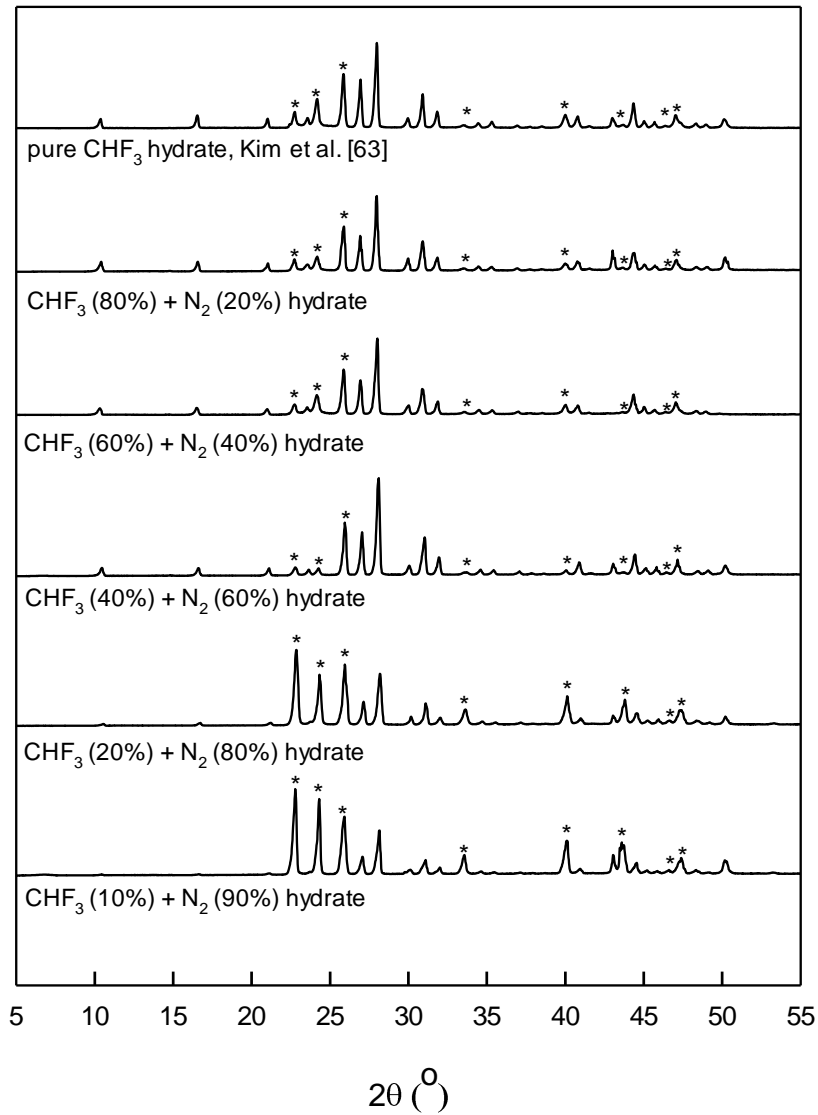


Figure 3.2.2. PXRD patterns of CHF₃ + N₂ hydrates.

Asterisks (*) indicate hexagonal ice (Ih).

In-situ Raman spectroscopy was used to further investigate the enclathration behavior of CHF₃ molecules in the gas hydrates during the hydrate formation. The C–H symmetric stretching mode of gaseous CHF₃ molecules was reported to appear primarily at 3036 cm⁻¹ [51, 63]. However, two major Raman peaks from the C–H symmetric stretching mode of enclathrated CHF₃ molecules in pure CHF₃ hydrate were observed at 3038 and 3059 cm⁻¹, which correspond to CHF₃ molecules captured in the large (5¹²6²) and small (5¹²) cages of the sI hydrate, respectively, as revealed in our previous study [63]. Figure 3.2.6 (a) and (b) present the Raman spectra of the N–N stretching mode of N₂ molecules and C–H stretching mode of CHF₃ molecules from the CHF₃ + N₂ hydrates, respectively. In Figure 3.2.6 (a), the Raman peak from the N–N stretching mode of enclathrated N₂ molecules was observed at 2323 cm⁻¹, indicating that N₂ molecules were clearly captured in the hydrate phase for all the feed gas compositions [64]. In Figure 3.2.6 (b), two Raman peaks from the C–H symmetric stretching mode of enclathrated CHF₃ molecules of CHF₃ + N₂ hydrates were observed at 3038 and 3059 cm⁻¹, which were consistent with those from pure CHF₃ hydrate [50, 63]. Even though CHF₃ is a relatively poorer guest for the small (5¹²) cages when CHF₃ competes with N₂ for occupation of the small (5¹²) cages, due to the slightly larger molecular size of CHF₃ than the diameter of the small (5¹²) cages of sI hydrate, it was clearly confirmed from Raman spectra that CHF₃ molecules are captured in both the large (5¹²6²) and small (5¹²) cages of the CHF₃ + N₂ hydrates.

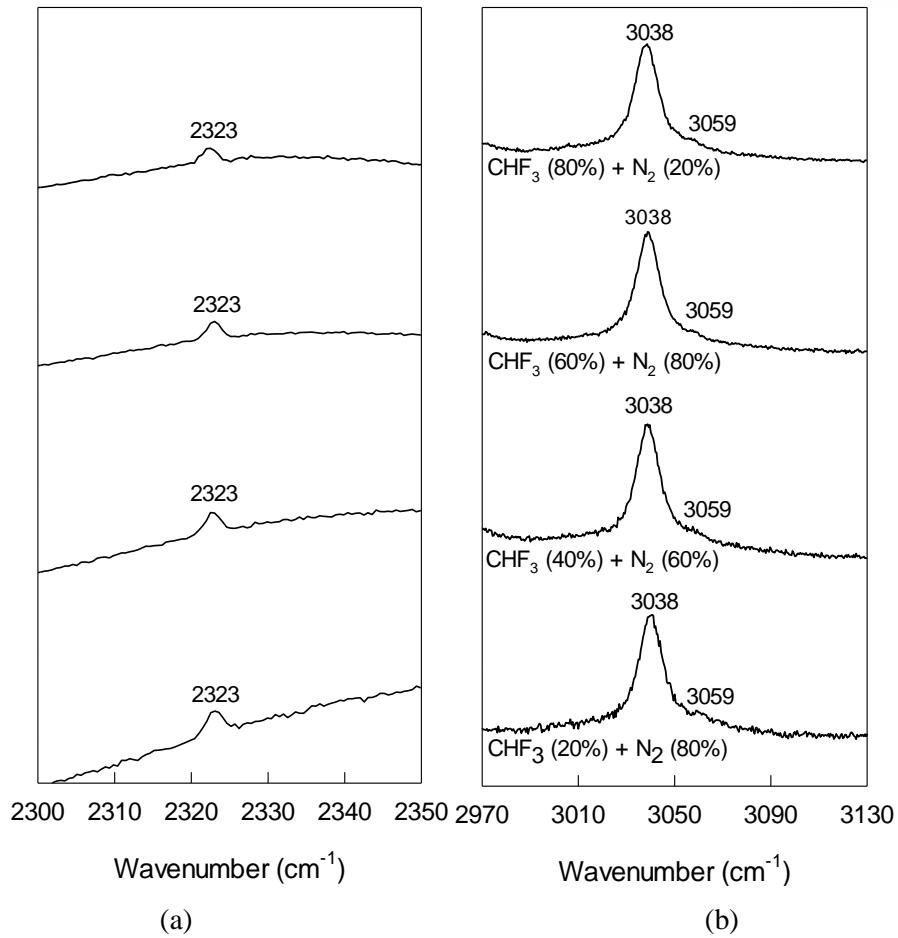
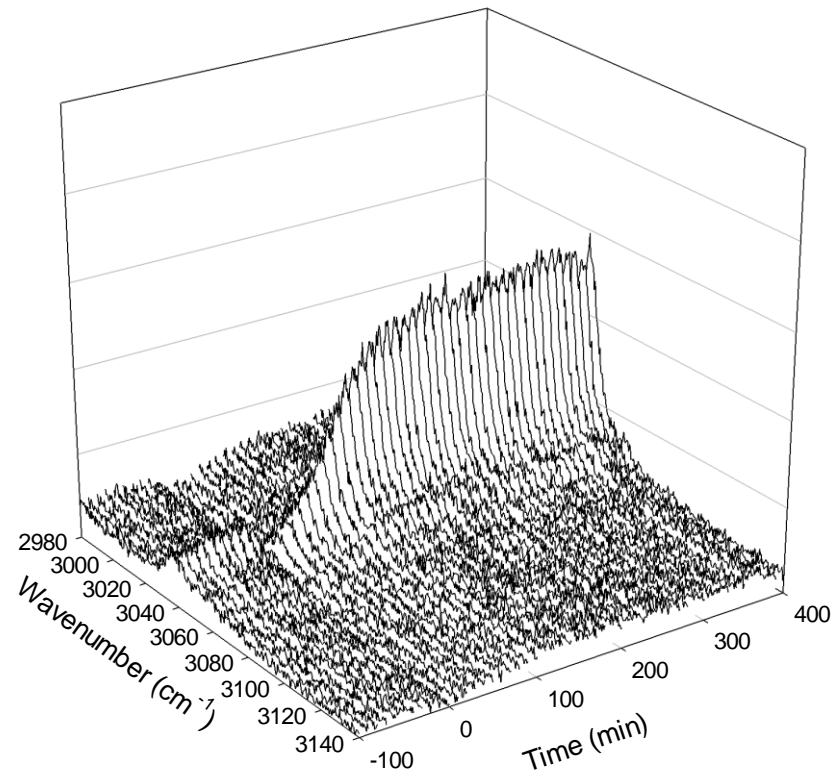


Figure 3.2.6. Raman spectra of $\text{CHF}_3 + \text{N}_2$ hydrates at 279.15 K and $\Delta P=1.0$ MPa.

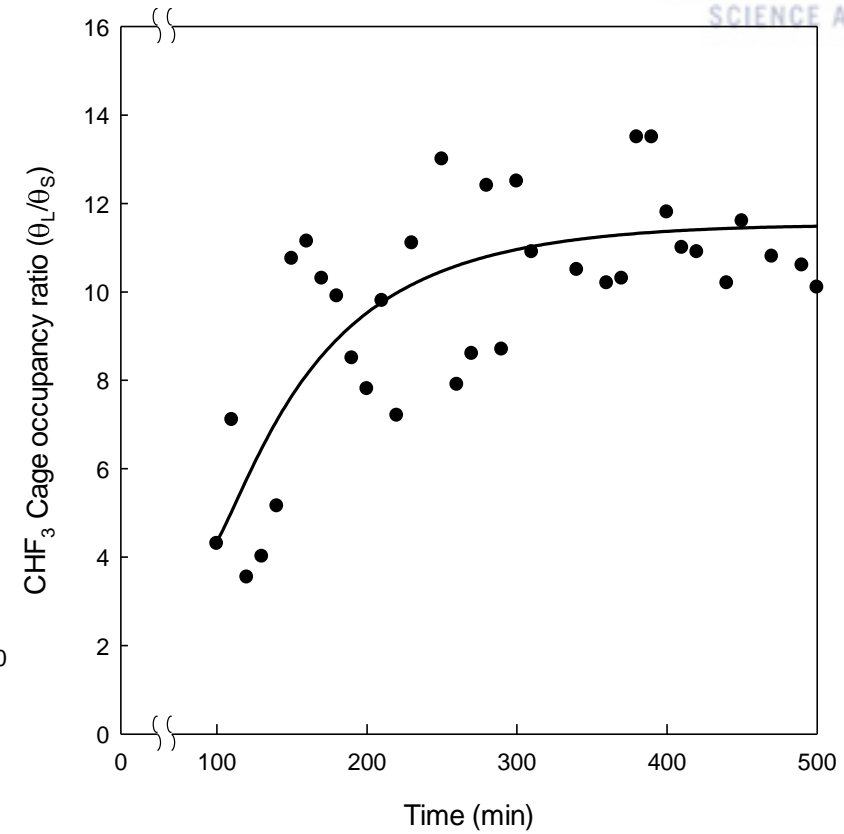
(a) N-N stretching mode of N_2 molecules.

(b) C-H stretching mode of CHF_3 molecules.

Figure 3.2.7 (a) presents real-time in situ Raman spectra collected during the growth process of the CHF₃ (40%) + N₂ (60%) hydrate at 279.15 K and 2.5 MPa ($\Delta P = 1.0$ MPa). The Raman peak of the C–H symmetric stretching mode for dissolved CHF₃ appeared at 3036 cm⁻¹. Then, the Raman peak intensity of dissolved CHF₃ suddenly became weakened at around 100 min, and two new Raman peaks at 3038 and 3059 cm⁻¹ started to grow, indicating the nucleation and subsequent growth of the CHF₃ (40%) + N₂ (60%) hydrate. The two Raman peaks at 3038 and 3059 cm⁻¹ continued to grow and reached a plateau after about 100 min from the beginning of the gas hydrate formation, which indicates that the CHF₃ (40%) + N₂ (60%) hydrate growth was almost completed. This is in good agreement with the results shown in Figures 3.2.3 and 3.2.4, which present the gas uptakes and the vapor composition changes. It should also be noted in Figure 3.2.7 (a) that the change in the growth of large (5¹²6²) cages was significantly more pronounced than that in the growth of small (5¹²) cages, implying that CHF₃ molecules have a strong preference for large (5¹²6²) cages over small (5¹²) cages during the CHF₃ + N₂ hydrate formation. The changes in the cage occupancy ratio (θ_L/θ_S) of CHF₃ molecules with respect to reaction time during the CHF₃ (40%) + N₂ (60%) hydrate formation are presented in Figure 3.2.7 (b). The cage occupancy ratio (θ_L/θ_S) was calculated from the area ratio of each Raman peak corresponding to large (5¹²6²) and small (5¹²) cages of sI hydrates, considering that large (5¹²6²) cages are three times more abundant than small (5¹²) cages in the unit cell of sI hydrates. The θ_L/θ_S values, which are significantly higher than 1.0 during the entire reaction time and the increasing behavior of the θ_L/θ_S values for the initial 100 min after hydrate nucleation, also clearly indicate the preferential occupation of CHF₃ molecules in the large (5¹²6²) cages of sI hydrate.



(a)



(b)

Figure 3.2.7. (a) Real time Raman spectra of the C-H stretching mode for CHF₃ (40%) + N₂ (60%) hydrate at 279.15 K and 2.5 MPa ($\Delta P=1.0$ MPa). (b) Cage occupancy ratio (θ_L/θ_S) of CHF₃ molecules captured in CHF₃ (40%) + N₂ (60%) hydrate at 279.15 K and 2.5 MPa ($\Delta P=1.0$ MPa).

3.2.5. Conclusions

A gas hydrate-based CHF₃ separation process has several advantages. First, it is environmentally friendly. The only material used for gas hydrate formation is water. Therefore, water is recycled for repeated use after dissociation of gas hydrate. Also, it has high separation efficiency. At 279.15 K, 40% CHF₃ can be enriched to 88% CHF₃ through only one step of hydrate formation and subsequent dissociation. Lastly, it is advantageous for CHF₃ reuse. Because this process does not involve chemical reactions and, thus, does not affect CHF₃ chemically, CHF₃ can be recovered without chemical decomposition or degradation. Also, the dissociation process is very simple: it entails just raising the temperature above the equilibrium one or just reducing pressure below the equilibrium one.

However, there are some points that need to be improved upon for actual application. For CHF₃ + N₂ gas mixtures with low CHF₃ concentrations, fairly high pressure is required for gas hydrate formation. In addition, the formation kinetics of the CHF₃ + N₂ hydrates seems to be slow, seeing that gas hydrate formation is generally completed after 100 min. Suitable hydrate promoters that can reduce hydrate formation pressure at a specified temperature and can enhance the hydrate formation rate should be explored and tested as a next step in order to improve the performance of the hydrate-based F-gas separation process. Although hydrate-based CHF₃ separation can offer highly concentrated CHF₃, several steps of hydrate formation and dissociation will be required to concentrate CHF₃ up to 100%. Therefore, a hybrid system coupled with a hydrate-based separation method and other separation methods can be devised to make the best use of the hydrate-based CHF₃ separation process. The conceptual diagram of the hybrid system for CHF₃ separation and recovery is shown in Figure 3.2.8. The exhaust gas with very low CHF₃ concentration (<1%) from emission sources first goes through an adsorption or membrane separation process to be enriched to 10%–20% CHF₃ [41, 65, 66]. Then, the first hydrate formation can concentrate the gas mixture up to 50%–60% CHF₃. The retrieved gas from the gas hydrate can be further enriched up to approximately 90% CHF₃ by the second hydrate formation. As a final step, pure (>99%) CHF₃ can be easily recovered by liquefaction for reuse.

In this study, the feasibility of gas hydrate-based F-gas separation was examined focusing primarily on the thermodynamic, structural, and cage-filling characteristics of the CHF₃ + N₂ hydrates, as well as separation efficiency. The overall experimental results obtained in this study clearly demonstrate that the gas hydrate-based CHF₃ separation process has a potential for application in actual emission sources by constituting a hybrid system coupled with other separation methods. However, further research into the means of lowering the hydrate formation pressure and increasing the hydrate formation rate needs to be done in order to secure the economic feasibility of the process.

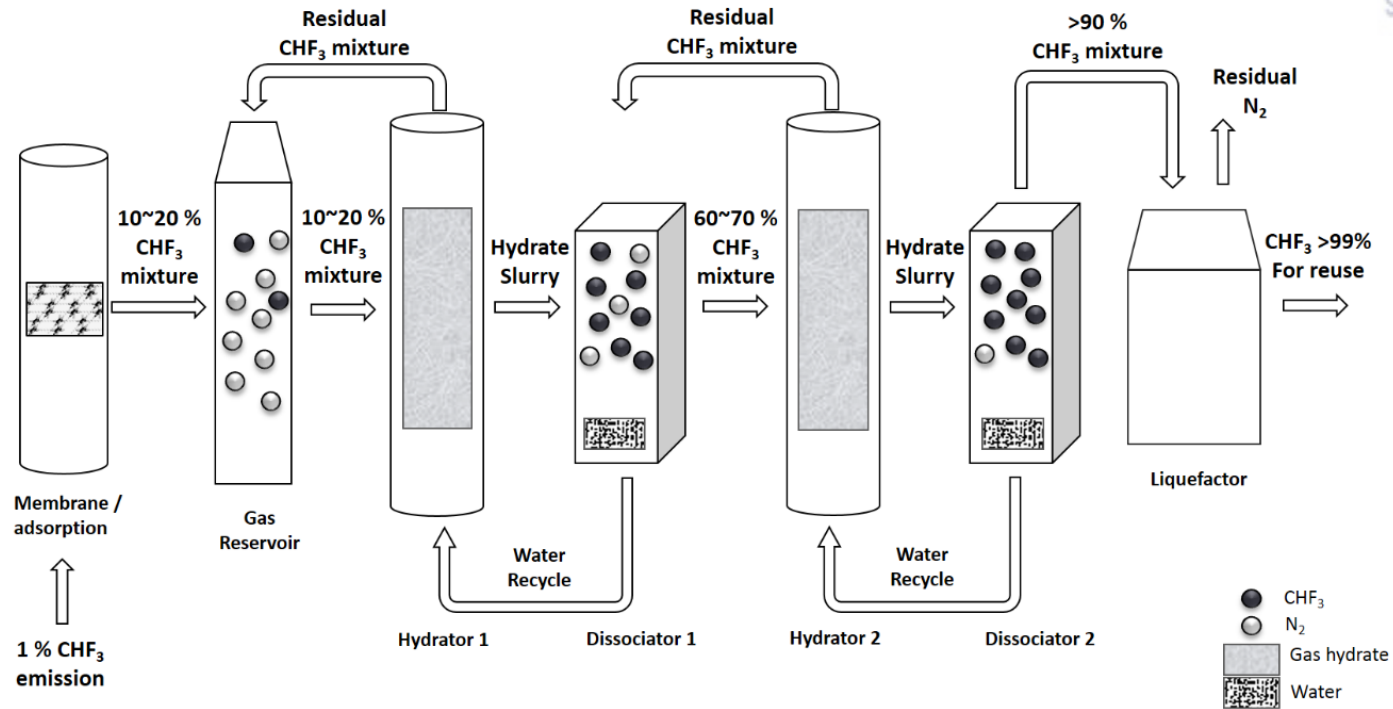


Figure 3.2.8. A hybrid system of gas hydrate-based CHF_3 separation process combined with membrane/adsorption and liquefaction processes.

3.3. The Azeotropic Behavior of $C_2F_6 + N_2$ Gas Hydrates

3.3.1. Abstract

C_2F_6 (hexafluoroethane, R116) is a fluorinated gas (F-gas) widely used in semiconductor industries, which also has a high global warming potential and a long atmospheric lifetime. In this study, the thermodynamic and structural characteristics of the $C_2F_6 + N_2$ gas hydrates were investigated for gas hydrate-based C_2F_6 separation from emission sources. This experiment measured the three-phase (hydrate, liquid water, and vapor [H-L_w-V]) equilibria of ternary C_2F_6 (10, 20, 40, 60, and 80%) + $N_2 + H_2O$ systems and indicated the possible existence of hydrate azeotropes at certain temperature ranges. Powder X-ray diffraction (PXRD) revealed that the ternary $C_2F_6 + N_2 + H_2O$ systems form structure II (sII) hydrates (*Fd3m*) for all C_2F_6 concentrations considered in this study. The pressure-composition diagram obtained at two different temperatures (275.15 K and 279.15 K) demonstrated that C_2F_6 is highly enriched in the hydrate phase at 275.15 K, whereas at 279.15 K, the $C_2F_6 + N_2 + H_2O$ systems have a hydrate azeotrope where the composition of the hydrate phase is the same as the composition of the vapor phase. The overall experimental results clearly indicate that hydrate-based C_2F_6 separation is thermodynamically feasible and the higher separation efficiency is achievable at lower temperature ranges.

3.3.2. Thermodynamic Phase Equilibria

The H-L_W-V equilibria of the ternary C₂F₆ + N₂ + H₂O systems with various C₂F₆ concentrations (10, 20, 40, 60, and 80%) were measured in the temperature range of 274 K to 282 K and in the pressure range of 0.5 MPa to 4.5 MPa. These results are presented in Figure 3.3.1 and Table 3.3.1. To examine the thermodynamic stability changes of the C₂F₆ + N₂ hydrates with the different C₂F₆ concentrations, the H-L_W-V equilibria of pure C₂F₆ hydrate were also included in Figure 3.3.1 [63]. However, the H-L_W-V equilibria of pure N₂ hydrate were not shown in Figure 3.3.1 because the equilibrium pressure of pure N₂ hydrate at a specified temperature is significantly higher than that of pure C₂F₆ hydrate [62]. When gas mixtures that consist of a large molecular gas and a small molecular gas form gas hydrates, the H-L_W-V equilibrium curves of the ternary gas hydrates are generally located between H-L_W-V equilibrium curves of each binary gas hydrate formed with a large molecular guest only and a small molecular guest only [8, 67]. As seen in Figure 3.3.1, the equilibrium pressure of the ternary C₂F₆ + N₂ + H₂O systems at a specified temperature gradually decreased with an increase in the concentration of a large molecular guest (C₂F₆) in the temperature range below 276.5 K. However, in the higher temperature ranges, some ternary C₂F₆ + N₂ + H₂O systems were more thermodynamically stable than the binary C₂F₆ + H₂O system. That is, in the temperature range above 276.5 K, the ternary gas hydrate composed of C₂F₆ (80%) + N₂ (20%) showed lower hydrate equilibrium pressures than the binary gas hydrate formed with pure C₂F₆ gas. This reversed behavior of H-L_W-V equilibria was also observed for the C₂F₆ (60%) + N₂ (40%) hydrate in the temperature range above 278.5 K. On the other hand, it was clear that the ternary gas hydrates with lower C₂F₆ concentrations (10% and 20%) were more thermodynamically unstable than the binary C₂F₆ + H₂O system for the entire temperature range, even though the H-L_W-V curves of these ternary gas hydrates were located far closer to that of the binary C₂F₆ + H₂O system than the binary N₂ + H₂O system. The hydrate phase equilibria shown in Figure 3.3.1 clearly indicate that the C₂F₆ + N₂ + H₂O systems can have a hydrate azeotrope at a certain temperature condition.

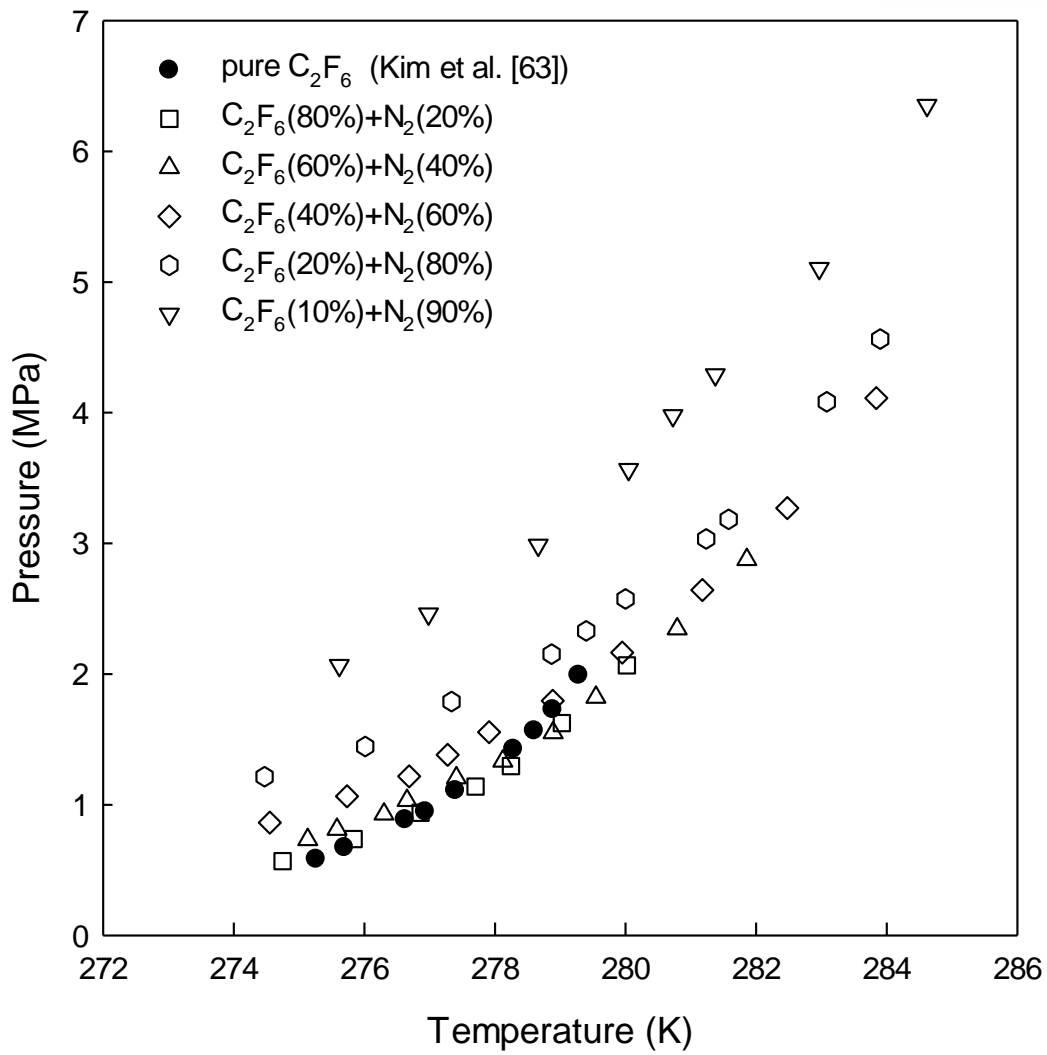


Figure 3.3.1. Three-phase (H-L_w-V) equilibria of pure C_2F_6 and $C_2F_6 + N_2$ hydrates.

Table 3.3.1. The three-phase (H-L_w-V) equilibria of the C₂F₆ + N₂ + H₂O systems.^a

C ₂ F ₆ (80%) + N ₂		C ₂ F ₆ (60%) + N ₂		C ₂ F ₆ (40%) + N ₂		C ₂ F ₆ (20%) + N ₂		C ₂ F ₆ (10%) + N ₂	
T/K	P/MPa	T/K	P/MPa	T/K	P/MPa	T/K	P/MPa	T/K	P/MPa
274.7	0.57	275.1	0.73	274.5	0.86	274.5	1.21	275.6	2.07
275.8	0.74	275.6	0.81	275.7	1.07	276.0	1.44	277.0	2.46
276.9	0.94	276.3	0.92	276.7	1.22	277.3	1.79	278.7	2.99
277.7	1.14	276.7	1.03	277.3	1.38	278.9	2.15	280.0	3.57
278.2	1.30	277.4	1.21	277.9	1.56	279.4	2.33	280.7	3.98
279.0	1.62	278.1	1.33	278.9	1.80	280.0	2.57	281.4	4.29
280.0	2.07	278.9	1.55	280.0	2.16	281.2	3.03		
		279.5	1.82	281.2	2.64	281.6	3.18		
		280.8	2.35						
		281.9	2.88						

^aStandard uncertainties u are $u(T) = 0.1$ K and $u(p) = 0.02$ MPa.

3.3.3. Structural Analyses through PXRD

The hydrate crystal structures and unit cell parameters of the $C_2F_6 + N_2$ gas hydrates with different C_2F_6 concentrations (10, 20, 40, 60, and 80%) were examined using PXRD and compared with those of pure C_2F_6 hydrate in Figure 3.3.2. Hexagonal ice (Ih) and solid C_2F_6 generated during the experimental procedure were also specifically indicated in Figure 3.3.2. Both pure C_2F_6 and pure N_2 hydrates were reported to form sII ($Fd3m$) [1, 63]. In this study, PXRD analyses revealed that all $C_2F_6 + N_2 +$ hydrates considered in this study were identified as cubic sII ($Fd3m$), with lattice parameters of 17.13 Å (C_2F_6 80%), 17.13 Å (C_2F_6 60%), 17.14 Å (C_2F_6 40%), 17.15 Å (C_2F_6 20%), and 17.15 Å (C_2F_6 10%). C_2F_6 can occupy only large ($5^{12}6^8$) cages of sII due to its large molecular size, while N_2 can fill both small (5^{12}) and large ($5^{12}6^8$) cages. The $C_2F_6 + N_2$ hydrates with higher C_2F_6 concentrations were expected to have larger lattice parameters because large-sized C_2F_6 molecules, which are preferentially enclathrated in the hydrate phase, can contribute in a more dominant fashion to the expansion of the ternary hydrates' unit cells. However, PXRD analyses demonstrated that C_2F_6 concentrations have no clear relationship with lattice parameters of $C_2F_6 + N_2$ gas hydrates.

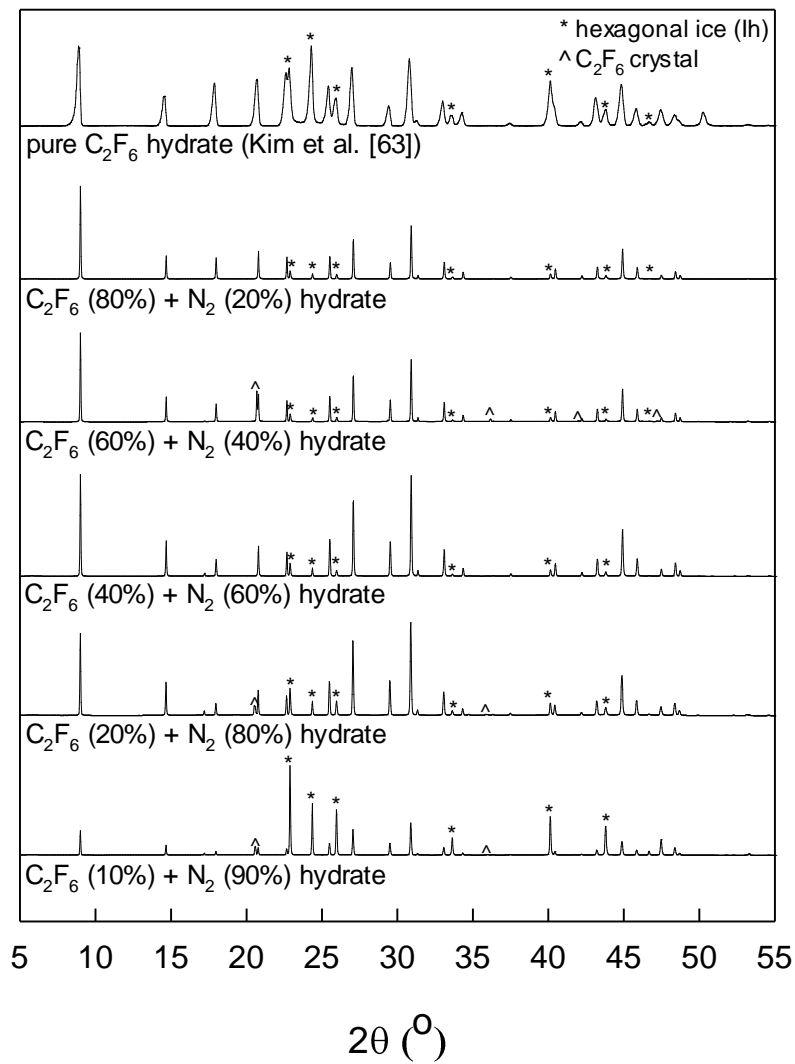


Figure 3.3.2. PXRD patterns of pure C₂F₆ and C₂F₆ + N₂ hydrates at 123.15 K.

Asterisks (*) indicate hexagonal ice (Ih).

3.3.4. Pressure-Composition Analyses

To verify the hydrate azeotrope of the ternary $C_2F_6 + N_2 + H_2O$ system at a certain temperature and to observe the selective partition of C_2F_6 between the gas hydrate phase and the vapor phase, a pressure-composition diagram of the $C_2F_6 + N_2 + H_2O$ systems was obtained at 275.15 K and 279.15 K (Figure 3.3.3 and Table 3.3.2). At the H-L_w-V equilibrium state, there are three phases—hydrate, liquid water, and vapor—and three components— C_2F_6 , N_2 , and H_2O —in the system. Thus, the system has two degrees of freedom. That is, the equilibrium composition of the hydrate and vapor phases is adjusted and determined accordingly when the pressure and temperature of the system is fixed. The vapor phase compositions can be approximated from the thermodynamic equilibrium curves of $C_2F_6 + N_2$ hydrates (shown in Figure 3.3.1) because the pressure-composition diagram (shown in Figure 3.3.3) was obtained from the HLW- V equilibrium. In Figure 3.3.3, the ternary $C_2F_6 + N_2 + H_2O$ systems at 275.15 K demonstrated a usual behavior of the phase composition change according to pressure conditions. For example, at 275.15 K, the $C_2F_6 + N_2$ gas hydrate (whose vapor phase composition is 22% C_2F_6) has a hydrate equilibrium pressure of 1.9 MPa; thus, the resulting composition in the hydrate phase was 53% C_2F_6 . It is evident that for any initial C_2F_6 compositions, gas hydrate formation resulted in more concentrated C_2F_6 in the hydrate phase at 275.15 K. However, at 279.15 K, where a hydrate azeotrope of the ternary $C_2F_6 + N_2 + H_2O$ system was suspected to appear (as shown in Figure 3.3.1), the existence of the hydrate azeotrope was clearly confirmed through the pressure-composition diagram of $C_2F_6 + N_2$ hydrates in Figure 3.3.3. At 279.15 K, C_2F_6 was found to be enriched in the hydrate phase at high pressure ranges. However, in Figure 3.3.3, as pressure decreased, the vapor phase composition of $C_2F_6 + N_2$ hydrates became identical to the hydrate phase composition. As was seen in Figure 3.3.1, at 279.15 K, the equilibrium pressures of C_2F_6 (60%) + N_2 (40%) and C_2F_6 (80%) + N_2 (20%) hydrates nearly overlapped each other and were lower than that of pure C_2F_6 hydrate. Therefore, it was clearly confirmed from Figure 3.3.1 and 3.3.3 that the ternary $C_2F_6 + N_2 + H_2O$ system forms a hydrate azeotrope at 279.15 K.

Several previous studies reported that some ternary systems, such as methane + propane + H_2O , krypton + propane + H_2O , HFC- 32 + HFC-134a + H_2O , and methane + ethylene + H_2O form hydrate azeotropes at certain temperatures [68-71]. While the specific reason for the occurrence of hydrate azeotropes is not yet clear, their occurrence can be attributed to the nature and structure of crystalline hydrates, the competing effect of guest molecules with different sizes, and the temperature effect on cage occupancies of guest molecules. The experimental results of this study clearly indicate that, in the case of $C_2F_6 + N_2$ gas mixtures, C_2F_6 can be significantly enriched through gas hydrate formation at lower temperature ranges where the hydrate azeotropes do not occur, and the $C_2F_6 + N_2 + H_2O$ systems form sII hydrates for all C_2F_6 concentrations considered in this study.

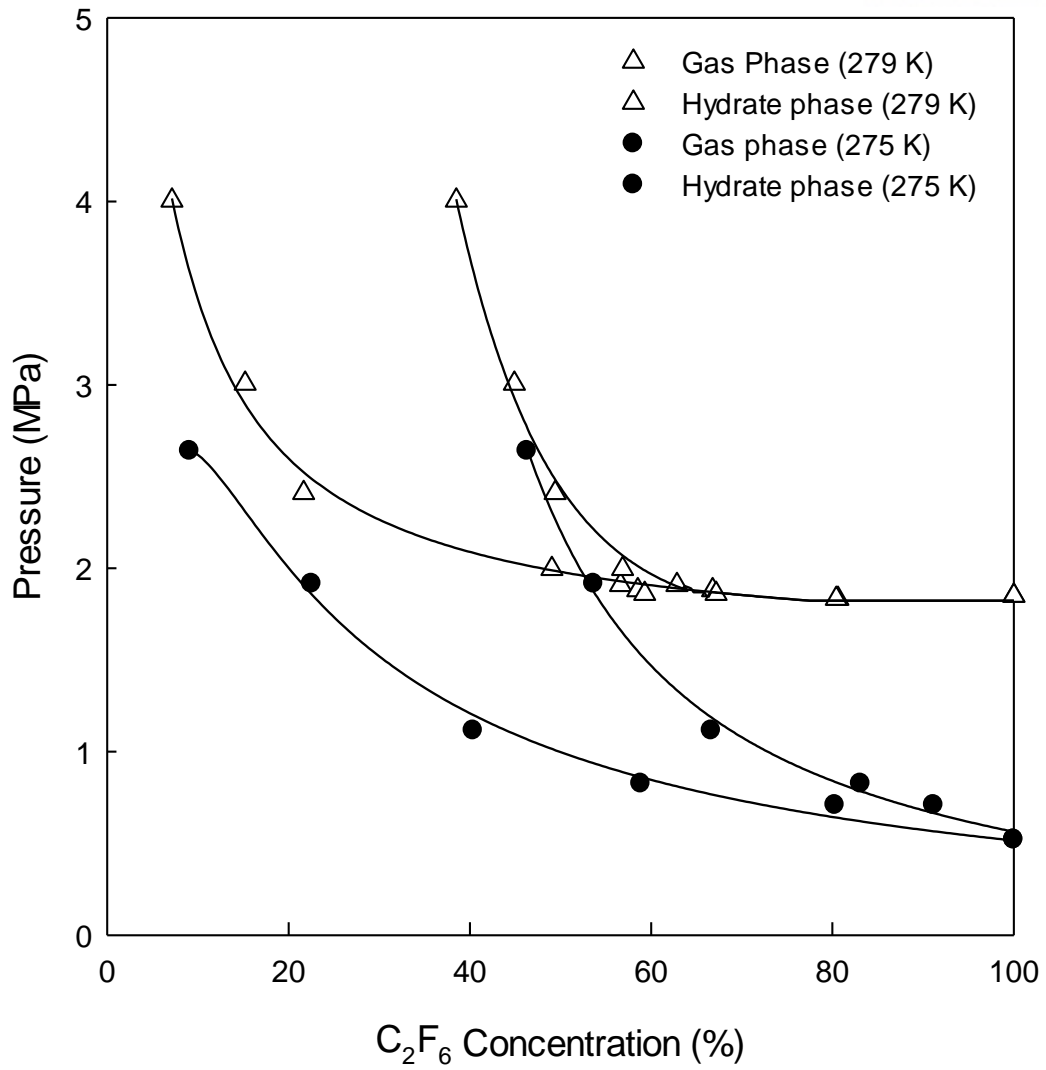


Figure 3.3.3. Pressure-composition diagram of C₂F₆ + N₂ + H₂O systems at 275.15 K and 279.15 K.

Table 3.3.2. Pressures and compositions of $C_2F_6 + N_2 + H_2O$ systems at 275.15 K and 279.15 K.^a

279.15 K			275.15 K		
Pressure (MPa)	C_2F_6 in vapor phase (mol%)	C_2F_6 in hydrate phase (mol%)	Pressure (MPa)	C_2F_6 in vapor phase (mol%)	C_2F_6 in hydrate phase (mol%)
1.85	100	100	0.52	100	100
1.83	80.6	80.4	0.71	80.3	91.1
1.86	59.3	67.2	1.92	22.6	53.7
1.88	58.5	66.8	0.83	58.9	83.1
1.91	56.6	62.9	1.12	40.4	66.7
2.00	49.1	56.9	2.64	9.1	46.3
2.41	21.7	49.4			
3.00	15.2	44.9			
4.01	7.12	38.5			

^aStandard uncertainties u are $u(\text{composition}) = 0.3$ mol%, $u(P) = 0.02$ MPa and $u(T) = 0.1$ K.

3.3.5. Conclusions

In this study, the thermodynamic and structural characteristics of $C_2F_6 + N_2$ hydrates were examined for hydrate-based C_2F_6 separation. The H-L_w-V equilibria revealed that the ternary $C_2F_6 + N_2 + H_2O$ systems could have hydrate azeotropes at certain temperature ranges ($T > 276.5$ K). PXRD patterns identified the crystalline structure of $C_2F_6 + N_2$ hydrates as sII (*Fd3m*) for all experimental C_2F_6 concentrations (10, 20, 40, 60, and 80%). The C_2F_6 separation efficiency was examined through a pressure-composition diagram at two different temperatures (275.15 K and 279.15 K). At 275.15 K, C_2F_6 was found to be highly enriched in the hydrate phase for all C_2F_6 concentration ranges. However, at 279.15 K, the ternary $C_2F_6 + N_2 + H_2O$ systems showed a hydrate azeotrope, where the vapor phase composition is identical to the hydrate phase composition. The overall experimental results including hydrate phase equilibria, crystalline hydrate structure, and C_2F_6 separation efficiency are expected to be helpful for future studies about the development of the gas hydrate-based C_2F_6 separation process.

3.4. NF₃ Hydrate Formation and its Microscopic Properties

3.4.1. Abstract

F-gases are man-made gases that are utilized mainly in the semiconductor industry and in refrigeration systems. Because F-gases have a high potential of contributing to global warming, various methods, including gas hydrate-based F-gas separation, for separating and recovering F-gases have been widely studied. However, gas hydrate formation with NF₃ has not been well studied in spite of its extremely high global warming potential (12,700) and its long atmospheric lifetime (740 years). In this study, the enclathration of NF₃ in gas hydrate lattices was investigated, with a focus on phase equilibria and guest distribution. The three-phase (gas hydrate (H) - liquid water (Lw) - vapor (V)) equilibria of NF₃ hydrate were measured to observe the stability conditions for NF₃ hydrate. The crystal structure of NF₃ hydrate was identified as cubic sI (*Pm3n*) with a lattice parameter of 11.87 Å through powder X-ray diffraction (PXRD). In addition, the cage-filling behavior of NF₃ hydrate was examined through both PXRD and *in situ* Raman spectroscopy. This revealed that the large (5¹²6²) cages were fully occupied by NF₃ molecules whereas the small (5¹²) cages were less populated. The results obtained in this study would be helpful for understanding the cage-specific occupation of F-gas molecules in sI hydrate and devising possible gas hydrate-based F-gas separation methods.

3.4.2. Thermodynamic Phase Equilibria

The three-phase (hydrate (H)–liquid water (L_w)–vapor (V)) equilibria of the NF_3 + water system were measured to determine the thermodynamically stable regions of NF_3 hydrate. Although a couple of phase equilibrium points of NF_3 hydrate (273.15K and 1.67 ± 0.02 MPa and 233.15 K and 0.37 ± 0.02 MPa), which correspond to the lower limit of H- L_w -V equilibrium points and one of hydrate (H) – ice (I) – vapor (V) equilibrium points, respectively, were reported in the literature [72], the three-phase (H- L_w -V) equilibrium data of NF_3 hydrate for wide pressure and temperature ranges have not been provided. In this study, the three-phase (H- L_w -V) equilibria of NF_3 hydrate were measured in a temperature range of 274.15–284.15 K and a pressure range of 1.7–6.8 MPa. The data are presented in Figure 3.4.1 and Table 3.4.1. Figure 3.4.1 confirmed that the previous equilibrium point (273.15K and 1.67 ± 0.02 MPa [72]) would be on an extension of the H- L_w -V equilibrium curve measured in this study. Through the three-phase (H- L_w -V) equilibrium data obtained in this study, NF_3 was found to have relatively higher hydrate equilibrium pressures at any given temperature than that of other F-gases such as SF_6 and CHF_3 [30, 63]. Because F-gases are mixed with N_2 for use in the semiconductor industry and N_2 hydrate has extremely high equilibrium pressures [62], it is expected from Figure 3.4.1 that NF_3 + N_2 mixtures will require high pressures for gas hydrate formation. Considering that F-gas separation using gas hydrates is based on the equilibrium pressure difference between F-gases and N_2 , the data presented in Figure 3.4.1 suggest that gas hydrate-based NF_3 separation from the exhaust gas associated with the semiconductor industry might occur under higher-pressure conditions and the NF_3 separation efficiency could be lower than that of other F-gases such as SF_6 and CHF_3 .

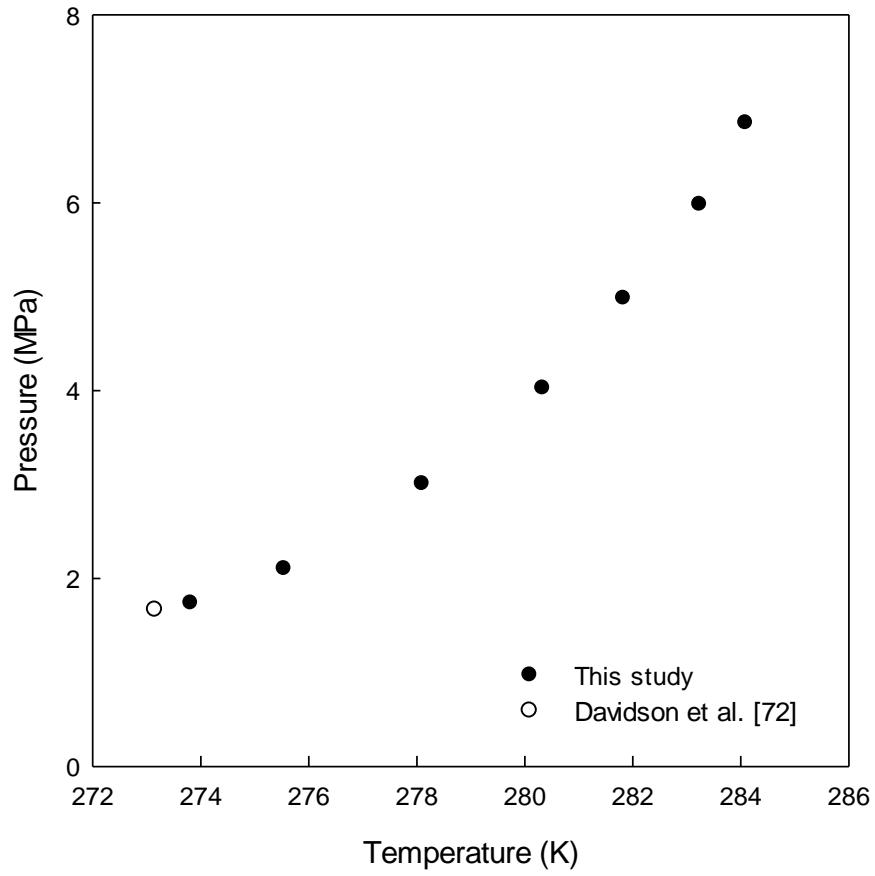


Figure 3.4.1. Three-phase (H-L_w-V) equilibria of pure NF₃ hydrate

Table 3.4.1. Hydrate phase equilibrium data of the NF_3 + water system^a.

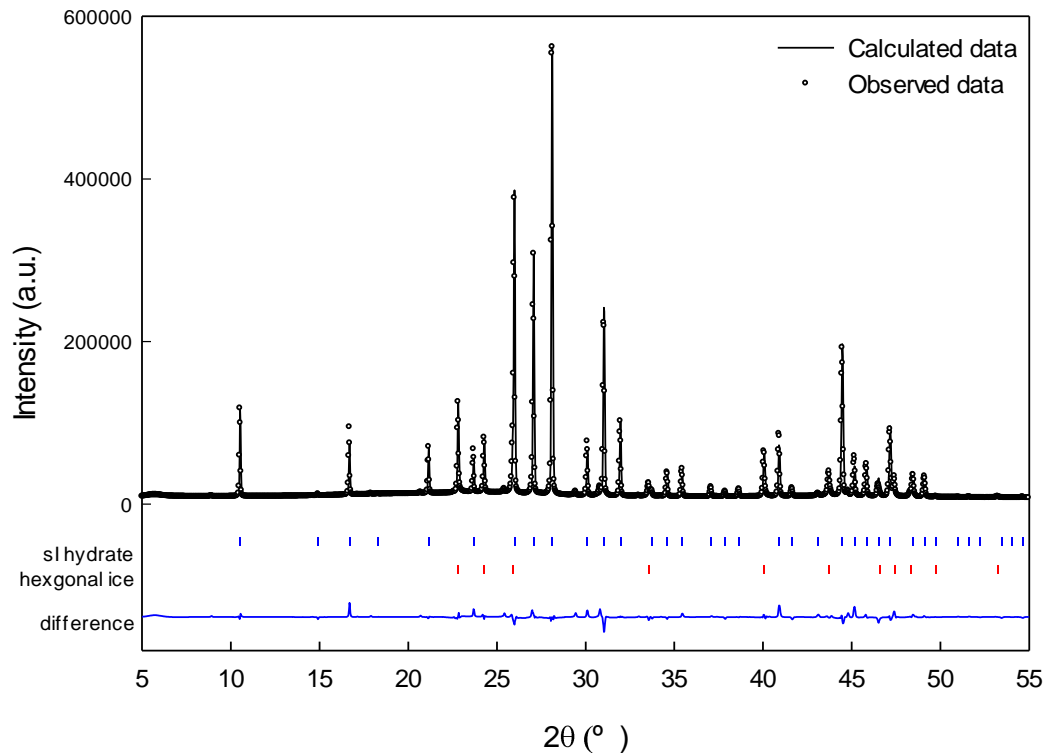
H-L_w-V	
T (K)	P (MPa)
284.1	6.85
283.2	5.99
281.8	4.98
280.3	4.03
278.1	3.01
275.5	2.11
273.8	1.74

^aStandard uncertainties u are $u(T) = 0.1$ K and $u(p) = 0.02$ MPa.

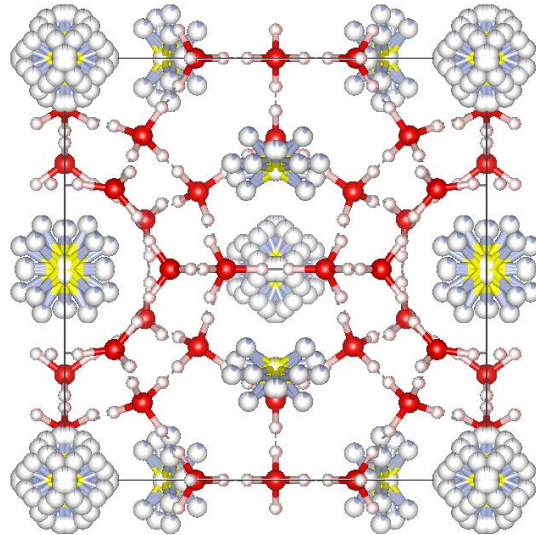
3.4.3. Microscopic Analyses on Pure NF₃ Hydrate

To identify the crystal structure and the lattice parameter of NF₃ hydrate, the PXRD patterns of NF₃ hydrate depicted in Figure 3.4.2 (a) were analyzed through the Fullprof program. The crystal structure of NF₃ hydrate was identified as cubic sI (*Pm3n*) with a lattice parameter of 11.87 Å, which was in good agreement with the result of the previous study [72].

The cage occupancy and distribution of NF₃ molecules in the hydrate phase were also analyzed with the Rietveld refinement of the PXRD patterns. An assumption that an NF₃ molecule is located at the center of a hydrate cage can lead to an inaccurate calculation for NF₃ cage occupancy because NF₃ molecules are asymmetric and polar. In particular, higher errors can be expected for the NF₃ cage occupancy in the large (5¹²6²) cages of sI because of their larger space in which NF₃ molecules can move around as compared to the space in small (5¹²) cages. In this study, the direct space method using the crystallography program (FOX) was adopted for refinement to calculate thermodynamically the optimal position and angle of the guest molecules in hydrate cages. This method was suggested and verified in the prior study to optimize the calculation of the cage occupancy and distributions of guest molecules in the hydrate structure [48, 73-75]. The structure of NF₃ hydrate was analyzed using modified guest positions (FOX program) and rigid body constraints. The PXRD patterns were well refined as a cubic *Pm3n* structure (sI), and the reliability factor R_{wp} was 13.2%. The cage occupancy resulting from the Rietveld refinement was found to be $\theta_s = 0.28$ for the small (5¹²) cages and $\theta_L = 0.99$ for the large (5¹²6²) cages. The crystal structure of NF₃ hydrate and the displacement of NF₃ molecules in sI (*Pm3n*) hydrate lattices are presented in Figure 3.4.2 (b), which demonstrates that NF₃ molecules show full symmetry in the cages of sI (*Pm3n*) hydrate. The displacement of NF₃ molecules in the small (5¹²) cages is negligible because of the lack of space for NF₃ molecules to move around in the small (5¹²) cages despite the relatively larger displacement of NF₃ molecules in the large (5¹²6²) cages.



(a)



(b)

Figure 3.4.2. (a) PXR D patterns of pure NF_3 hydrate at 133.15 K. The vertical tick marks represent the calculated sI hydrate and hexagonal ice.

(b) The displacement of NF_3 molecules in sI ($Pm\bar{3}n$) hydrate lattices.

The cage-filling behavior of NF_3 molecules in the hydrate phase was analyzed through Raman spectroscopy. First, the Raman spectrum of NF_3 gas was measured at 298.15 K and 2.0 MPa. NF_3 gas molecules exhibited four representative Raman peaks at 494, 646, 910, and 1031 cm^{-1} , as shown in Figure 3.4.3 [76]. However, for a more detailed and precise observation of the cage-filling characteristics of NF_3 molecules in gas hydrates, one specific Raman peak from gaseous NF_3 molecules located at 646 cm^{-1} was selected because of its stronger peak intensity compared to that of other Raman peaks from NF_3 molecules. As seen in Figure 4, gaseous NF_3 shows a shoulder peak at 644 cm^{-1} , whose intensity decreases as the temperature decreases [77]. NF_3 hydrate exhibited two Raman peaks (one major peak at 642 cm^{-1} and the other minor one at 650 cm^{-1}) in the range of 600–680 cm^{-1} . It should be noted that NF_3 hydrate has no noticeable shoulder peak at around 642 cm^{-1} . Considering the cage ratio of sI hydrate ($Pm\bar{3}n$) and the molecular size of NF_3 , the large peak at 642 cm^{-1} can be assigned to NF_3 molecules captured in the large ($5^{12}6^2$) cages, while the small peak at 650 cm^{-1} indicates NF_3 molecules in small (5^{12}) cages.

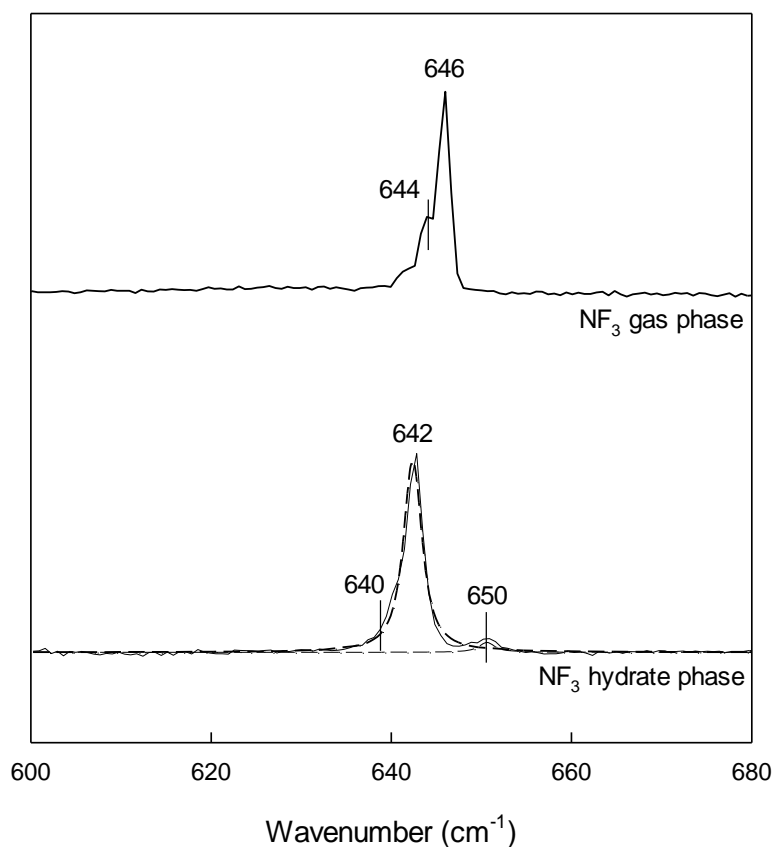


Figure 3.4.3. Raman spectra of pure NF_3 hydrate and its deconvolution

Considering that large ($5^{12}6^2$) cages are three times more abundant than small (5^{12}) cages in the unit cell of sI hydrates, the cage occupancy ratio (θ_L/θ_S) can be calculated from the area ratio (A_L/A_S) of each peak from the Raman spectrum. To obtain the A_L/A_S from the Raman peak, the Raman spectrum of NF_3 hydrate in Figure 3.4.3 was de-convoluted by using the Voigt function. After de-convolution, the A_L/A_S

of NF_3 molecules enclathrated in the large ($5^{12}6^2$) and small (5^{12}) cages of the NF_3 hydrate was found to be 20.54 ± 4.65 , which corresponds to the θ_L/θ_S of 6.84 ± 1.55 . The cage occupancies of NF_3 molecules in the large ($5^{12}6^2$) and small (5^{12}) cages of sI can be calculated by incorporating the cage occupancy ratio (θ_L/θ_S) into the following thermodynamic equation, which involves the chemical potential of water molecules in the sI hydrate:

$$\mu_w(h) - \mu_w(h^0) = \frac{RT}{23} [3\ln(1 - \theta_{L,\text{NF}_3}) + \ln(1 - \theta_{S,\text{NF}_3})] \quad (1)$$

where $\mu_w(h^0)$ is the chemical potential of water molecules in the hypothetical empty hydrate cages and θ_S and θ_L are the fractional cage occupancies of small (5^{12}) and large ($5^{12}6^2$) cages of sI hydrate, respectively [78]. When the clathrate hydrate is in equilibrium with ice, $\mu_w(\text{ice}) - \mu_w(h^0)$ becomes $-\Delta\mu_w^\circ$ and the $\Delta\mu_w^\circ$ is the chemical potential of the empty lattice relative to the ice. The $\Delta\mu_w^\circ$ value for sI hydrate used in this study is 1,297 J/mol [78]. The resulting cage occupancies were found to be $\theta_S = 0.14$ and $\theta_L = 0.96$. The cage occupancy obtained from the combination of the Raman spectrum and the thermodynamic equation was generally in good agreement with that obtained from the Rietveld refinement of the PXRD data. It can be clearly seen from the experimental results that NF_3 molecules prefer to occupy the large ($5^{12}6^2$) cages rather than the small (5^{12}) cages in sI hydrate.

3.4.4. Conclusions

In this study, the thermodynamic, structural, and cage-filling characteristics of NF_3 hydrate were investigated. The three-phase (H-L_w-V) equilibria measured at a temperature range of 274.15–284.15K and a pressure range of 1.7–6.8 MPa revealed that the binary NF_3 + water system forms NF_3 hydrate at relatively higher-pressure conditions. This suggests that the gas hydrate-based separation of NF_3 occurs at higher pressures compared to that of other F-gases like SF_6 and CHF_3 . The NF_3 hydrate was identified as cubic sI ($Pm\bar{3}n$) with a lattice parameter of 11.87Å. In addition, through the Rietveld refinement of the PXRD patterns, the cage occupancy of the NF_3 molecules in the sI hydrate was analyzed as $\theta_s = 0.28$ and $\theta_L = 0.99$. Cage-filling behavior was also examined using Raman spectroscopy. The Raman spectrum of NF_3 hydrate demonstrated the occupation of NF_3 molecules in both small (5^{12}) and large ($5^{12}6^2$) cages of sI hydrate, and the de-convolution of the Raman peaks resulted in a cage occupancy of $\theta_s = 0.14$ and $\theta_L = 0.96$. The overall results of the experiment, including thermodynamic phase equilibria, crystal lattice analyses, and the cage-filling characteristics of NF_3 hydrate, would be helpful for the future study of gas hydrate formation with various F-gases and its application to separation/recovery processes.

Chapter 4. Novel discoveries on sH hydrate forming F-gases

4.1 A New Discovery of Abnormal sH Hydrate Former: $c\text{-C}_4\text{F}_8$ Gas Molecules

4.1.1. Abstract

Clathrate hydrates are formed by hydrogen-bonded water molecules, which capture guest molecules inside cages, usually at high-pressure and low-temperature conditions. The crystal structures of clathrate hydrates are determined by the characteristics of the guest molecules. There are three representative clathrate hydrate structures: sI, sII, and sH. Among these, sH hydrates are known to form with large-sized hydrocarbons, which exist in a liquid phase, in the presence of small help gas molecules. However, no gaseous guests have ever been discovered that can form sH hydrates. Herein, we show that a large molecular fluorinated gas (octafluorocyclobutane, $c\text{-C}_4\text{F}_8$), can stabilize the crystal structure of sH hydrate by occupying large ($5^{12}6^8$) cages. The shift of thermodynamic equilibrium curves for octafluorocyclobutane ($c\text{-C}_4\text{F}_8$) + methane (CH_4) clathrate hydrates according to $c\text{-C}_4\text{F}_8$ concentrations verified that $c\text{-C}_4\text{F}_8$ existed in a gas phase under three-phase (clathrate hydrate (H) - liquid water (L_w) – vapor (V)) equilibrium conditions. The inclusion of $c\text{-C}_4\text{F}_8$ molecules in sH clathrate hydrate in the presence of CH_4 molecules was clearly demonstrated through powder X-ray diffraction (PXRD) and ^{13}C NMR spectroscopy. The discovery of a gaseous sH former, $c\text{-C}_4\text{F}_8$, contributes to broadening clathrate hydrate science and engineering by expanding target components for sH hydrates, and also offers excellent potential in various applications of sH hydrates, especially in clathrate hydrate-based gas separation.

4.1.2. Thermodynamic Phase Equilibria

The three-phase (H-L_w-V) equilibrium curves of pure CH₄, c-C₄F₈ (2.0%) + CH₄ (98.0%), and c-C₄F₈ (5.0%) + CH₄ (95.0%) clathrate hydrates are shown in Figure 4.1.1 and Table 4.1.1. Figure 4.1.1 clearly demonstrates that the phase equilibrium curves of the c-C₄F₈ + CH₄ clathrate hydrates are thermodynamically more stabilized when compared with that of pure CH₄ clathrate hydrate [79], implying that a large molecular guest, c-C₄F₈, is incorporated in the clathrate hydrates. In addition, the observation of a shift in the thermodynamic equilibrium curves in accordance with c-C₄F₈ concentrations indicated that c-C₄F₈ was a gaseous guest for clathrate hydrates under H-L_w-V equilibrium conditions. With a very few exceptions of solid-phase or water-miscible liquid-phase sH formers, all sH formers reported to date are water-immiscible liquids [1, 80, 81]. Thus, the system (H-L_w-L_{Hc}-V) is univariant as determined by the Gibbs phase rule, thereby resulting in no shift in thermodynamic equilibrium curves at different concentrations of sH formers. Here, we present the first gaseous sH former, c-C₄F₈, by demonstrating that the H-L_w-V system of the c-C₄F₈ + CH₄ clathrate hydrates is divariant.

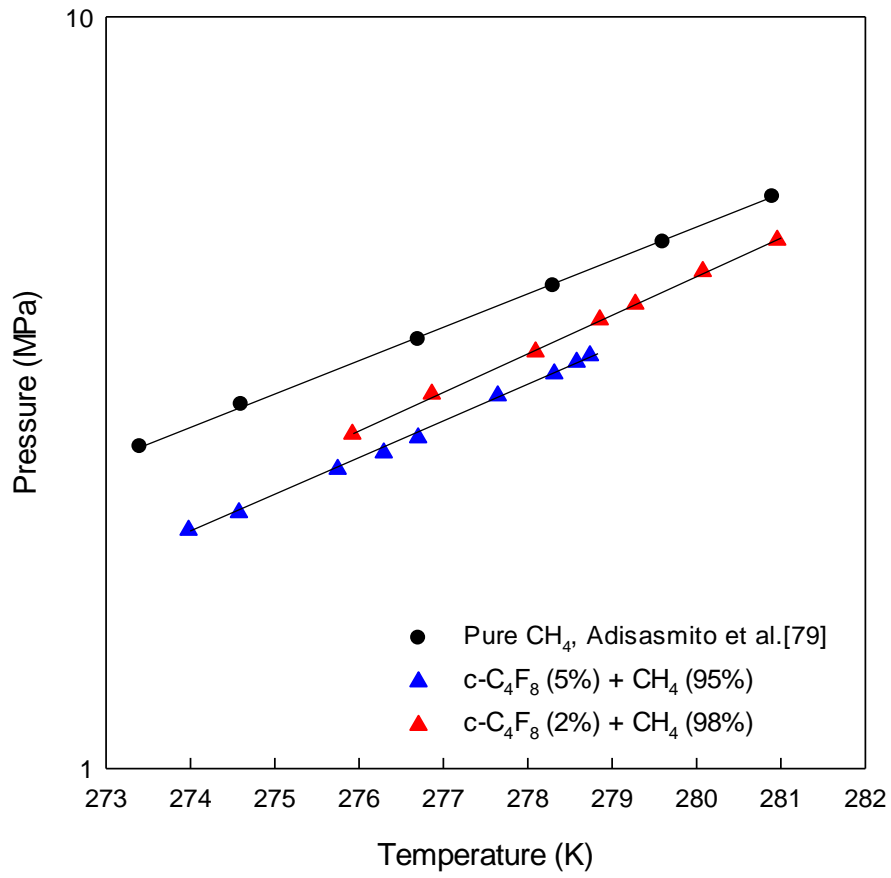


Figure 4.1.1. Three-phase (H-L_w-V) equilibria of c-C₄F₈ + CH₄ hydrates

Table 4.1.1. Thermodynamic Phase equilibria of c-C₄F₈ + CH₄ hydrates

c-C ₄ F ₈ (5.0%) + CH ₄ (95.0%)		c-C ₄ F ₈ (2.0%) + CH ₄ (98.0%)	
T (K)	P (MPa)	T (K)	P (MPa)
274.0	2.08	278.9	3.96
274.6	2.19	279.3	4.15
275.7	2.50	280.1	4.59
276.3	2.63	281.0	5.06
276.7	2.75		
277.6	3.13		
278.3	3.35		
278.6	3.47		
278.7	3.54		

4.1.3. Microscopic Demonstration of sH Hydrate Formation

The formation of sH clathrate hydrate with a $c\text{-C}_4\text{F}_8 + \text{CH}_4$ gas mixture was confirmed through PXRD and ^{13}C NMR spectroscopy. Figure 4.1.2 shows the PXRD patterns of the $c\text{-C}_4\text{F}_8$ (5.0%) + CH_4 (95.0%) clathrate hydrate, which were refined using the Fullprof program. As revealed by PXRD patterns, clathrate hydrate samples consisted of three crystal phases: sI ($Pm\bar{3}n$), sH ($P6/mmm$), and hexagonal ice (Ih, $P63/mmc$). Here, sH originated from $c\text{-C}_4\text{F}_8$ (5.0%) + CH_4 (95.0%) clathrate hydrate, whereas sI was derived from pure CH_4 hydrate, which was formed from residual CH_4 gas. The lattice parameters of sH clathrate hydrate ($P6/mmm$) are $a = b = 12.18 \text{ \AA}$, $c = 9.99 \text{ \AA}$, whereas those of sI clathrate hydrate ($Pm\bar{3}n$) are $a = b = c = 11.85 \text{ \AA}$.

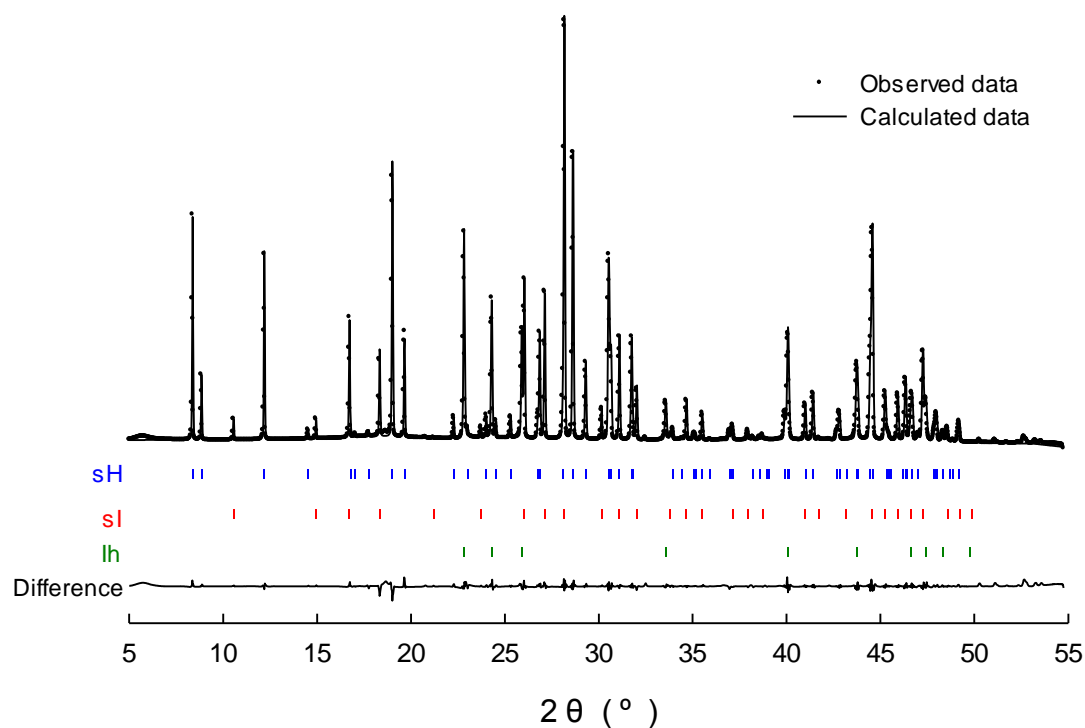


Figure 4.1.2. PXRD patterns of $c\text{-C}_4\text{F}_8$ (5.0%) + CH_4 (95.0%) hydrate.

Asterisks (*) indicate hexagonal ice (Ih).

As cage-dependent ^{13}C NMR peaks for enclathrated CH_4 molecules can be an effective indicator of each clathrate hydrate structure [77], the formation of sH from the $\text{c-C}_4\text{F}_8$ (5.0%) + CH_4 (95.0%) gas mixture was further confirmed by ^{13}C NMR spectroscopy. In Figure 4.1.3, the resonance peaks appearing at -4.5 and -4.9 ppm indicate that CH_4 molecules captured in small (5^{12}) and medium ($4^35^66^3$) cages of sH clathrate hydrates formed from the $\text{c-C}_4\text{F}_8$ + CH_4 gas mixture, respectively. The area ratio of the medium ($4^35^66^3$) to small (5^{12}) cages for CH_4 molecules enclathrated in sH clathrate hydrates after deconvolution of the peaks was 0.67, indicating that both small (5^{12}) and medium ($4^35^66^3$) cages of sH were almost fully occupied by CH_4 molecules, whereas the large ($5^{12}6^8$) cages were occupied only by $\text{c-C}_4\text{F}_8$ molecules. On the other hand, the resonance peaks at -4.3 and -6.6 ppm showed CH_4 molecules captured in small (5^{12}) and large ($5^{12}6^2$) cages of sI clathrate hydrates, respectively. The area ratio of the large ($5^{12}6^2$) to small (5^{12}) cages for CH_4 molecules after deconvolution was approximately 3.35, which clearly supports sI clathrate hydrate formation from residual CH_4 gas. Although small (5^{12}) cages are common among both sI and sH clathrate hydrates, the chemical shift (-4.5 ppm) of CH_4 molecules in the small (5^{12}) cages of sH is distinguishable from that (-4.3 ppm) in the small (5^{12}) cages of sI due to the slight difference in the size and environment of the cages. The PXRD patterns and ^{13}C NMR spectrum clearly demonstrate that $\text{c-C}_4\text{F}_8$ participated in forming sH clathrate hydrate in the presence of CH_4 as a help gas.

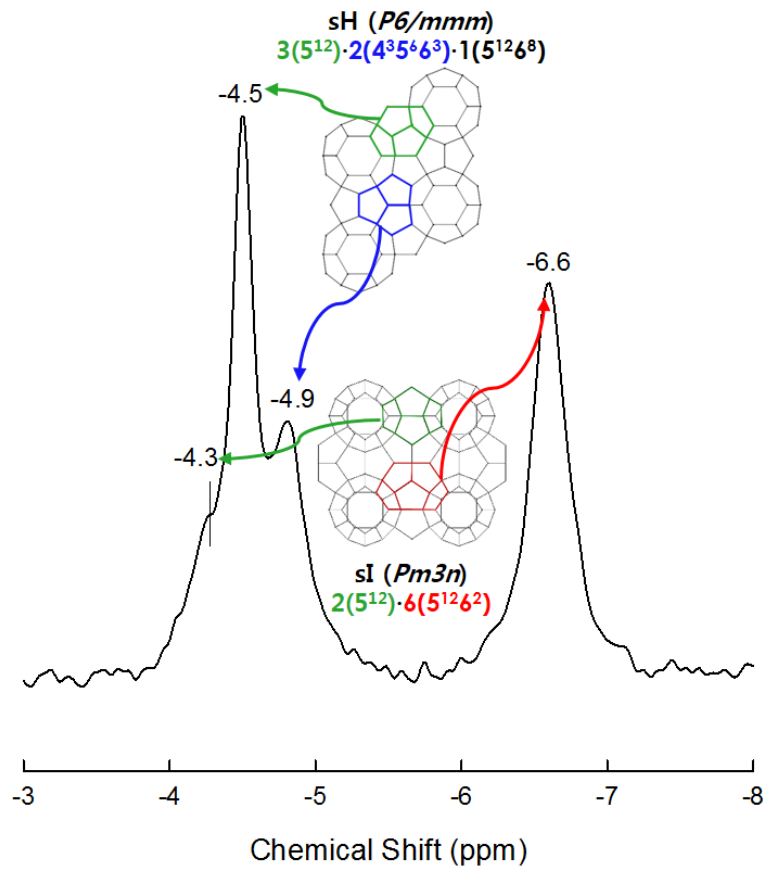


Figure 4.1.3. ^{13}C NMR spectroscopy of c- C_4F_8 (5.0%) + CH_4 (95.0%) mixture hydrate

4.1.4. Conclusions

The experimental results clearly verify the novel discovery of a gaseous sH hydrate and its occupation in the unit cell of sH, as illustrated in Figure 4.1.4. The phase equilibria of $c\text{-C}_4\text{F}_8 + \text{CH}_4$ clathrate hydrates indicated that the thermodynamic stability of the sH $c\text{-C}_4\text{F}_8 + \text{CH}_4$ clathrate hydrates was increased by the inclusion of $c\text{-C}_4\text{F}_8$ molecules when compared with that of sI formed from CH_4 molecules alone. Moreover, the equilibrium curve shift of clathrate hydrates according to $c\text{-C}_4\text{F}_8$ concentrations demonstrated enclathration of $c\text{-C}_4\text{F}_8$ as a gaseous sH former. The PXRD and ^{13}C NMR results revealed the coexistence of sH ($P6/mmm$) and sI ($Pm3n$) in clathrate hydrates formed from $c\text{-C}_4\text{F}_8 + \text{CH}_4$ gas mixtures, indicating that $c\text{-C}_4\text{F}_8$ is entrapped in large ($5^{12}6^8$) cages of sH in the presence of CH_4 , which acts as a help gas and occupies small (5^{12}) and medium ($4^35^66^3$) cages of sH.

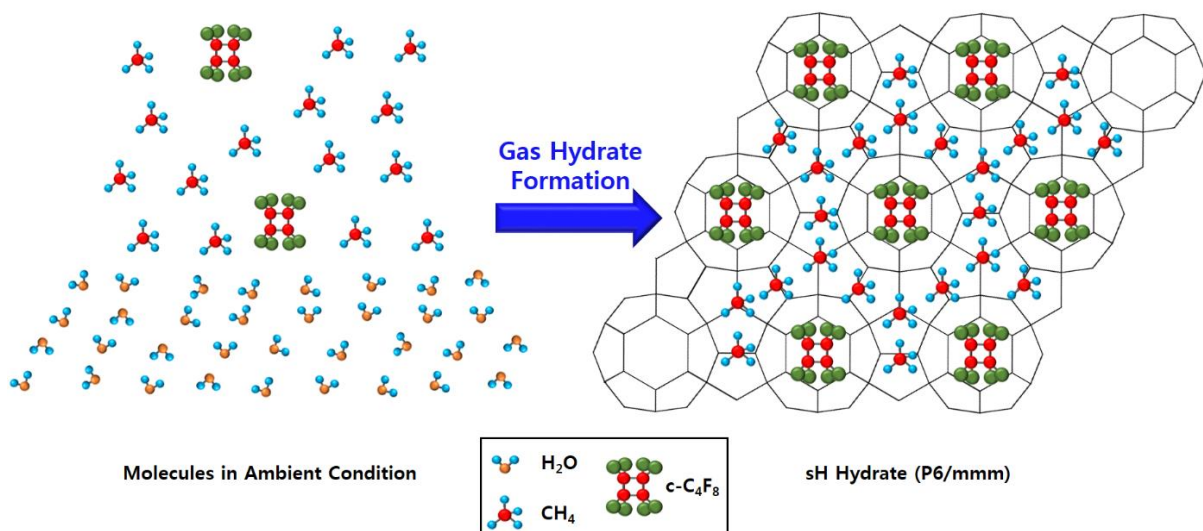


Figure 4.1.4. The conceptual diagram clathrate hydrate formation with gas-phase sH hydrate former

This letter reports the first experimental demonstration that large-sized gas molecules can be sH hydrate formers in the presence of suitable help gas molecules. The discovery in this study can contribute to significant advances in clathrate hydrate science and engineering. The findings provide new insight into the enclathration behavior of clathrate hydrates. The experimental results prove that large-sized fluorinated gases, such as $c\text{-C}_4\text{F}_8$, which were not thought to be captured in clathrate hydrate cages, can be target components of clathrate-based gas separation. The discovery illustrates that the stereotypical idea that liquid-phase hydrocarbons are always necessary for sH clathrate hydrate formation needs to be reconsidered. In other words, this study illustrates that sH clathrate hydrates can also be formed from pure water with gaseous mixtures. This study can be expected to have major implications for clathrate hydrate science and engineering, especially for clathrate hydrate-based gas separation by expanding target components for separation into large-sized fluorinated gases.

4.2. An Investigation on Dual (sH/sII) Hydrate Former: C₃F₈ Gas Molecules

4.2.1. Abstract

This study demonstrates that C₃F₈ molecules can form gas hydrates, while it was supposed to be impossible due to the large molecular size of C₃F₈ (7.68 Å). From experimental attempts for gas hydrate formation of C₃F₈ with various other gases, it was discovered that C₃F₈ can be enclathrated in gas hydrate cages only in presence of suitable help gases (CH₄ and SF₆). Also, it was found that the gas hydrate structures formed by C₃F₈ and help gases were different respective to help gases. Therefore, this study investigated the thermodynamic and spectroscopic characteristics of each gas hydrate formed by C₃F₈ with two different help gases (CH₄ or SF₆). First, the three-phase equilibria (H – L_w – V) of the ternary systems (C₃F₈ (10%) + CH₄ (90%) + water and C₃F₈ (25, 50%) + SF₆ (75, 50%) + water) were measured. The phase equilibria curve shift compared to that of the binary system of pure CH₄ or SF₆ + water verified the incorporation of C₃F₈ molecules in gas hydrate cages. Moreover, phase equilibria curve shift according to different C₃F₈ concentration proves that C₃F₈ act as gas phase guest while being enclathrated in gas hydrate phase. The crystal structures of C₃F₈ (10%) + CH₄ (90%) and C₃F₈ (25, 50%) + SF₆ (75, 50%) hydrates were analyzed through PXRD patterns. Here, it was discovered that C₃F₈ (10%) + CH₄ (90%) gas mixture forms sH (*P6/mmm*) hydrate while there are coexisting sI hydrate formed by residual CH₄ gas. On the other hand, the crystal structure of C₃F₈ (25, 50%) + SF₆ (75, 50%) hydrates were identified as sII (*Fd3m*), for both C₃F₈ concentrations used in this study. Additionally, ¹³C NMR spectroscopy was conducted to solidify the sH hydrate formation with C₃F₈ (10%) + CH₄ (90%) gas mixture. The result proved the coexistence of sH and sI hydrates by expressing CH₄ peaks captured in both small (5¹²) and medium (4³5⁶6³) cages of sH (*P6/mmm*) hydrate and those captured in both small (5¹²) and large (5¹²6²) cages of sI (*Pm3n*) hydrate. Lastly, *in-situ* Raman spectroscopy was used to demonstrate the inclusion of C₃F₈ molecules in sH (*P6/mmm*) and sII (*Fd3m*) hydrates in presence of different help gases (CH₄ or SF₆). From the overall experimental results, it was demonstrated that C₃F₈ molecule is a dual hydrate former which can form different gas hydrate structures depending on help gases. By considering that it is not only the first discovery of a dual hydrate former of sII and sH hydrates, but also a discovery of gas phase sH hydrate former, this study holds a significant importance in gas hydrate science and is expected to be useful for potential gas hydrate applications.

4.2.2. Thermodynamic Phase Equilibria

C_3F_8 molecule is not able to form gas hydrate alone, due to its large molecular size (7.68 Å), whereas CH_4 and SF_6 molecules can form sI ($Pm3n$) and sII ($Fd3m$) hydrates alone, respectively. Since there are several cases where large molecular guests can be captured in gas hydrate phase with small help gas, at first, C_3F_8 molecule was also expected to be enclathrated in hydrate phase in presence of well-known help gases such as CH_4 , N_2 , CO_2 and so on [82-89]. Here, C_3F_8 formed gas hydrates only with CH_4 , while it did not involve in gas hydrate formation with other small help gases. Next, gas hydrate formation of C_3F_8 was tried with other gas hydrate formers with larger molecular sizes such as propane and THF, which occupy only large ($5^{12}6^4$) cages of sII hydrate [1]. However, they also couldn't make C_3F_8 molecules be enclathrated in gas hydrate phase. Lastly, gas hydrate formation of C_3F_8 molecules in presence of large-sized fluorinated molecules such as SF_6 and C_2F_6 , which are known to form sII hydrate and occupy only large ($5^{12}6^4$) cages, was tried [28, 30, 63, 87]. Finally, the thermodynamic phase equilibria proved that C_3F_8 plays a role in gas hydrate formation in presence of CH_4 and SF_6 molecules.

Here, Figure 4.2.1(a) and Table 4.2.1(a) present the three-phase (H-L_w-V) equilibria of the ternary system of C_3F_8 (10%) + CH_4 (90%) + water, while Figure 4.2.1(b) and Table 4.2.1(b) present that of the ternary system of C_3F_8 (25%, 50%) + SF_6 (75%, 50%) + water with two different C_3F_8 concentrations. It should be notified that the pressure condition examined in this study is below the liquefaction range of all three components (C_3F_8 , CH_4 and SF_6). Therefore, if C_3F_8 does not participate in gas hydrate formation, the three-phase (H-L_w-V) equilibria point should appear at the exact same point of pure CH_4 or SF_6 hydrate when the C_3F_8 fraction of the mixture gas is considered. However, Figure 4.2.1(a) and (b) shows three-phase (H-L_w-V) equilibria curve shift compared to that of the pure CH_4 or SF_6 + water system [87], demonstrating C_3F_8 participation in gas hydrate formation. Moreover, in Figure 4.2.1(b), the phase equilibria curve shift of C_3F_8 (50%) + SF_6 (50%) + water system from C_3F_8 (25%) + SF_6 (75%) + water system confirmed that C_3F_8 is a gas phase hydrate former. According the Gibb's phase rule ($F = C - P + 2$), the phase equilibria should be fixed regardless of C_3F_8 concentrations if C_3F_8 exist as liquid phase.

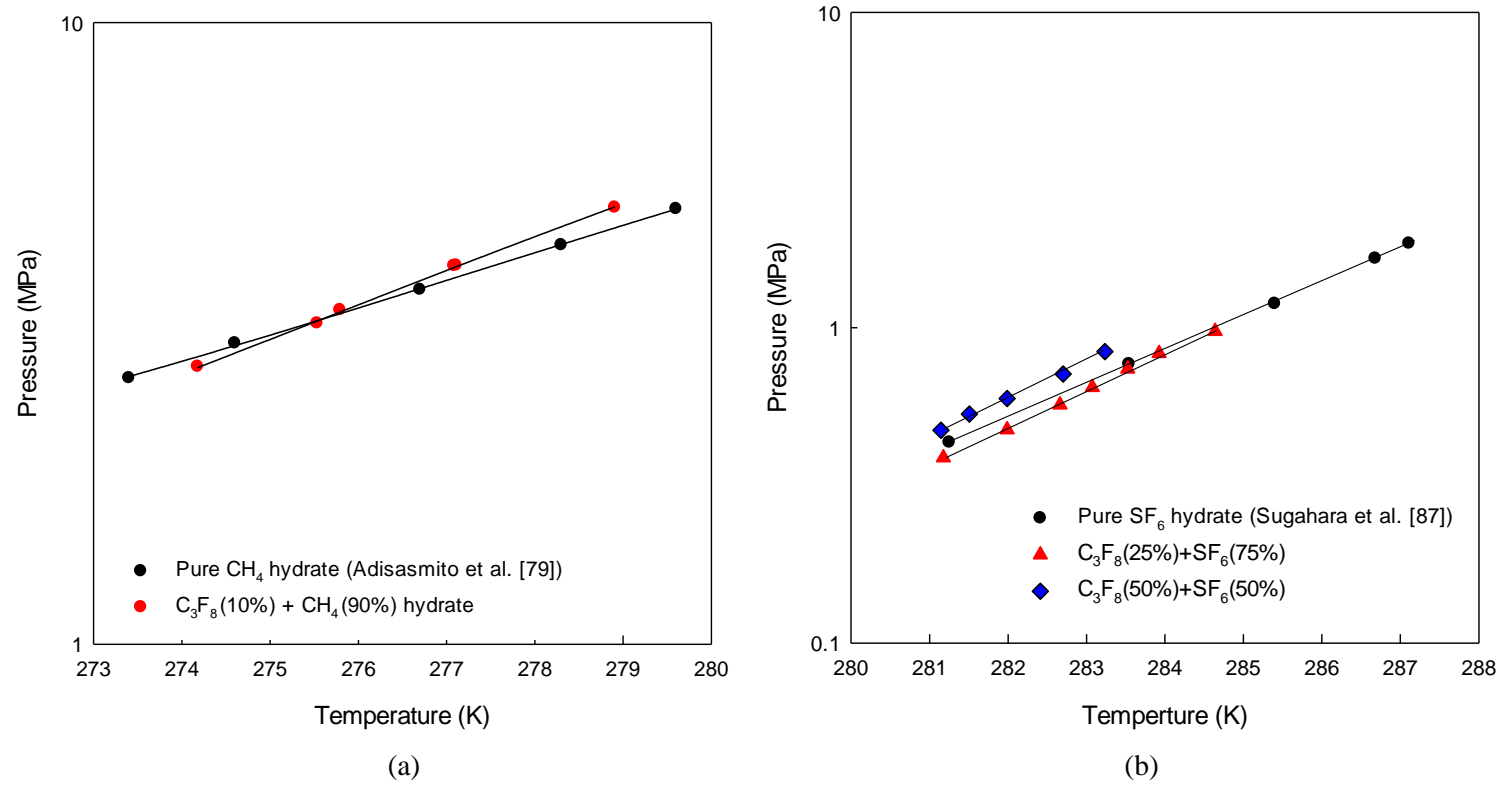


Figure 4.2.1. (a) Three-phase (H-L_w-V) equilibria of C₃F₈ (10%) + CH₄ (90%) hydrate.
 (b) Three-phase (H-L_w-V) equilibria of C₃F₈ (25%) + SF₆ (75%) and C₃F₈ (50%) + SF₆ (50%) hydrates.

Table 4.2.1. (a) Three-phase (H-L_w-V) equilibria of C₃F₈ + CH₄ hydrate

C₃F₈ (10%) + CH₄ (90%) hydrate	
T (K)	P (MPa)
274.2	2.80
275.5	3.29
275.8	3.45
277.1	4.06
277.1	4.07
278.9	5.05

(b) Three-phase (H-L_w-V) equilibria of C₃F₈ + SF₆ hydrates

C₃F₈ (25%) + SF₆ (75%) hydrate		C₃F₈(50%) + SF₆ (50%) hydrate	
T (K)	P (MPa)	T (K)	P (MPa)
281.2	0.39	281.1	0.47
282.0	0.48	281.5	0.53
282.7	0.57	282.0	0.60
283.1	0.65	283.2	0.84
283.5	0.74	282.7	0.71
283.9	0.83		
284.6	0.97		

4.2.3. Microscopic Analyses on sH Hydrate

Figure 4.2.2 shows the PXRD pattern of gas hydrate structures formed from C_3F_8 (10%) + CH_4 (90%) + water system, while Figure 4.2.3 (a) and (b) show those formed from C_3F_8 (25%) + SF_6 (75%) + water and C_3F_8 (50%) + SF_6 (50%) + water systems. In Figure 4.2.2, it is clearly revealed that C_3F_8 (10%) + CH_4 (90%) mixture gas formed sH ($P6/mmm$) hydrates with the crystal lattice parameter of $a=b=12.17 \text{ \AA}$, $c=10.03 \text{ \AA}$, while there also exists sI ($Pm\bar{3}n$) hydrate with the crystal lattice parameter of $a=b=c=11.86 \text{ \AA}$, which is formed from residual CH_4 gas. On the other hand, in Figure 4.2.3 (a) and (b), the crystal structures of C_3F_8 (25%) + SF_6 (75%) and C_3F_8 (25%) + C_2F_6 (75%) hydrates were identified as sII ($Fd\bar{3}m$), and their lattice parameters were determined as $a=b=c=17.14 \text{ \AA}$ and 17.20 \AA . These results tell that C_3F_8 can form two different gas hydrate structures of sH ($P6/mmm$) and sII ($Fd\bar{3}m$), according to help gases it forms with. Due to its large molecular size (7.68 \AA) of C_3F_8 , it was expected to be enclathrated in only large cages of sH hydrate ($5^{12}6^8$) or that of sII hydrate ($5^{12}6^4$).

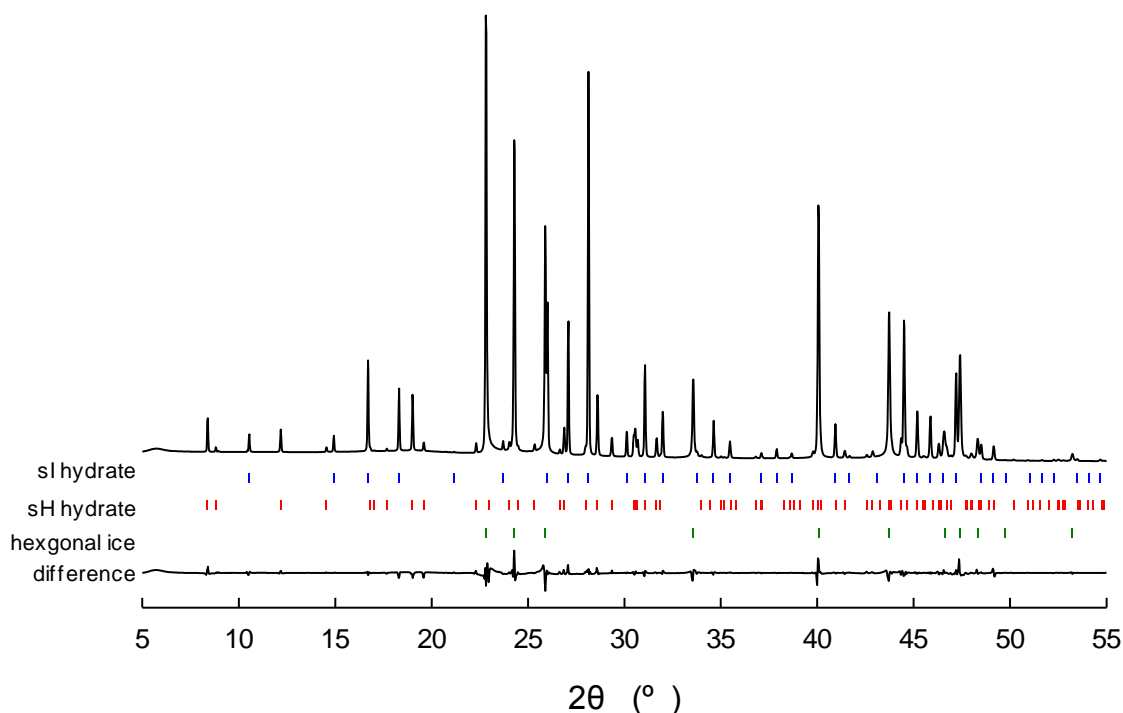
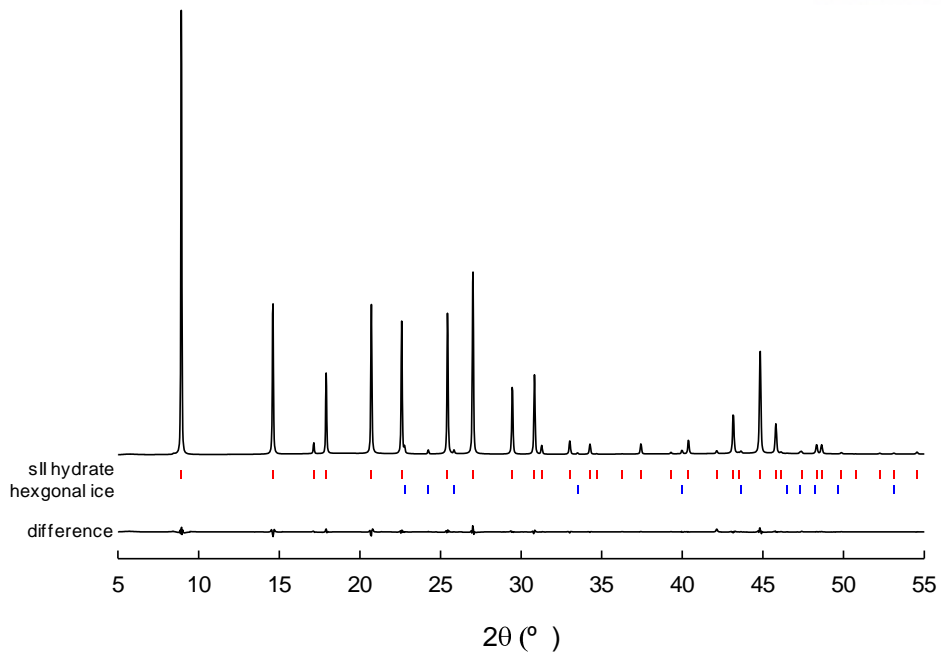
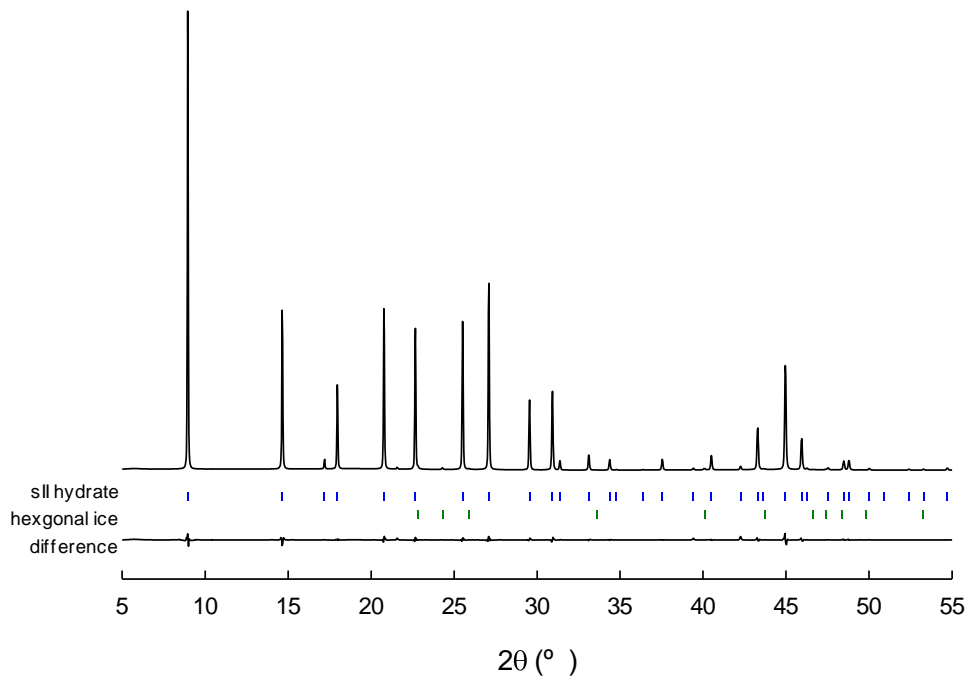


Figure 4.2.2. PXRD patterns of C_3F_8 (10%) + CH_4 (90%) hydrate at 123.15 K.



(a)



(b)

Figure 4.2.3. (a) PXRD patterns of C_3F_8 (25%) + SF_6 (75%) hydrate at 123.15 K.
 (b) PXRD patterns of C_3F_8 (50%) + SF_6 (50%) hydrate at 123.15 K.

^{13}C NMR spectroscopy was conducted to further demonstrate sH hydrate formation by C_3F_8 (10%) + CH_4 (90%) mixture gas. Figure 4.2.4 shows the ^{13}C NMR spectra of C_3F_8 (10%) + CH_4 (90%) hydrate. Here, there are four peaks in total which appear from CH_4 molecules in gas hydrate phase. First, peaks at -4.5 and -4.9 express CH_4 molecules captured in small (5^{12}) and medium ($4^35^66^3$) cages of sH ($P6/mmm$) hydrate [85]. From these peaks, it is clearly confirmed that C_3F_8 (10%) + CH_4 (90%) mixture gas formed sH hydrate, and C_3F_8 molecules must be enclathrated in sH large ($5^{12}6^8$) cages according to its large molecular size. Second, peaks at -4.3 and -6.7 represents CH_4 molecules captured in small (5^{12}) and large ($5^{12}6^2$) cages in sI ($Pm3n$) hydrate [85]. This result implies that there are pure CH_4 hydrate formed by residual CH_4 molecules which were not used for sH hydrate formation. Therefore, from the ^{13}C NMR spectra shown in Figure 4.2.4, the coexistence of sH ($P6/mmm$) and sI ($Pm3n$) hydrates formed by C_3F_8 (10%) + CH_4 (90%) gas mixture was demonstrated.

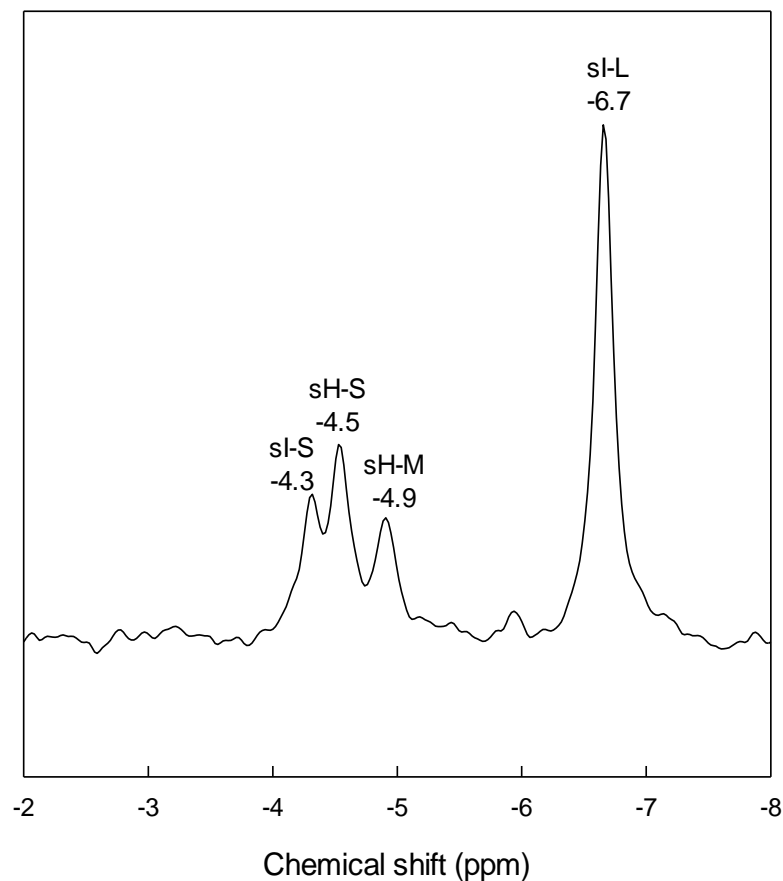


Figure 4.2.4. ^{13}C NMR spectra of C_3F_8 (10%) + CH_4 (90%) hydrate.

4.2.4. Observation of sII Hydrate Formation through *in-situ* Raman Spectroscopy

Raman spectroscopy was utilized to verify sH hydrate formation from C_3F_8 (10%) + CH_4 (90%) + water system, and *in-situ* Raman spectroscopy was conducted to observe the hydrate growth process with C_3F_8 (25, 50%) + SF_6 (75, 50%) gas mixture. Figure 4.2.5 compares peaks from CH_4 molecules before and after the hydrate formation. Before gas hydrate formation, gas phase CH_4 molecules which are dissolved in water are expressed at 2915 cm^{-1} . However, when gas hydrates are fully grown, there appear three peaks at 2904, 2914 and 2916 cm^{-1} . Here, two peaks at 2904 and 2916 cm^{-1} represent CH_4 molecules enclathrated in large ($5^{12}6^2$) and small (5^{12}) cages, while the other one at 2914 cm^{-1} represent those in small (5^{12}) and medium ($4^35^66^3$) cages in sH hydrate [85]. Therefore, sH hydrate formation from the C_3F_8 (10%) + CH_4 (90%) + water system was also verified from Raman spectroscopy result shown in Figure 4.2.6. Figure 4.2.7 (a) and (b) are the growth pattern and final Raman spectra of C_3F_8 (25%) + SF_6 (75%) hydrate, respectively. In both Figure 4.2.6 (a) and (b), three peaks appear at 770, 773 and 780 cm^{-1} , which designate SF_6 molecules in hydrate phase, SF_6 molecules dissolved in water and C_3F_8 molecules in hydrate phase, respectively [87, 90]. From Figure 4.2.6 (a), it is clearly confirmed from simultaneously growing peaks at 770 cm^{-1} and 780 cm^{-1} , that C_3F_8 molecules are being enclathrated with SF_6 molecules during the gas hydrate growth procedure. From Figure 4.2.6 (b), it is seen that C_3F_8 molecules are not preferred to SF_6 molecules for enclathration in sII hydrate large ($5^{12}6^4$) cages, considering the final peak intensity expressed by C_3F_8 and SF_6 molecules captured in hydrate phase. This is attributed to the competition between C_3F_8 and SF_6 molecules to occupy large ($5^{12}6^4$) cages of sII hydrate, while it is more unfavorable to C_3F_8 because of its larger molecular size.

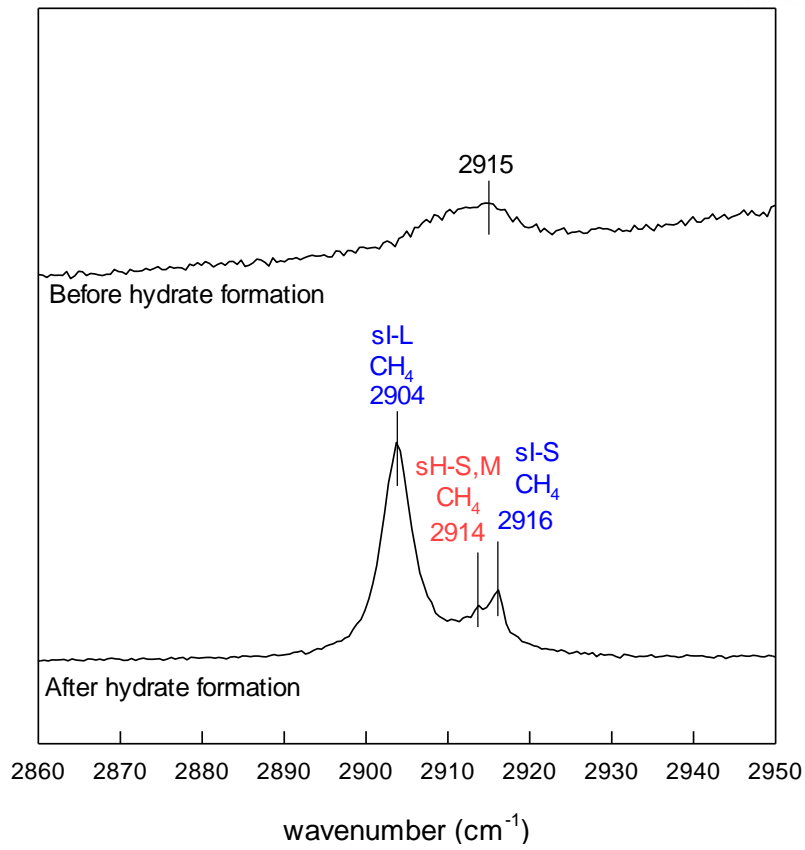


Figure 4.2.5. Raman spectra of C₃F₈ (10%) + CH₄ (90%) hydrate.

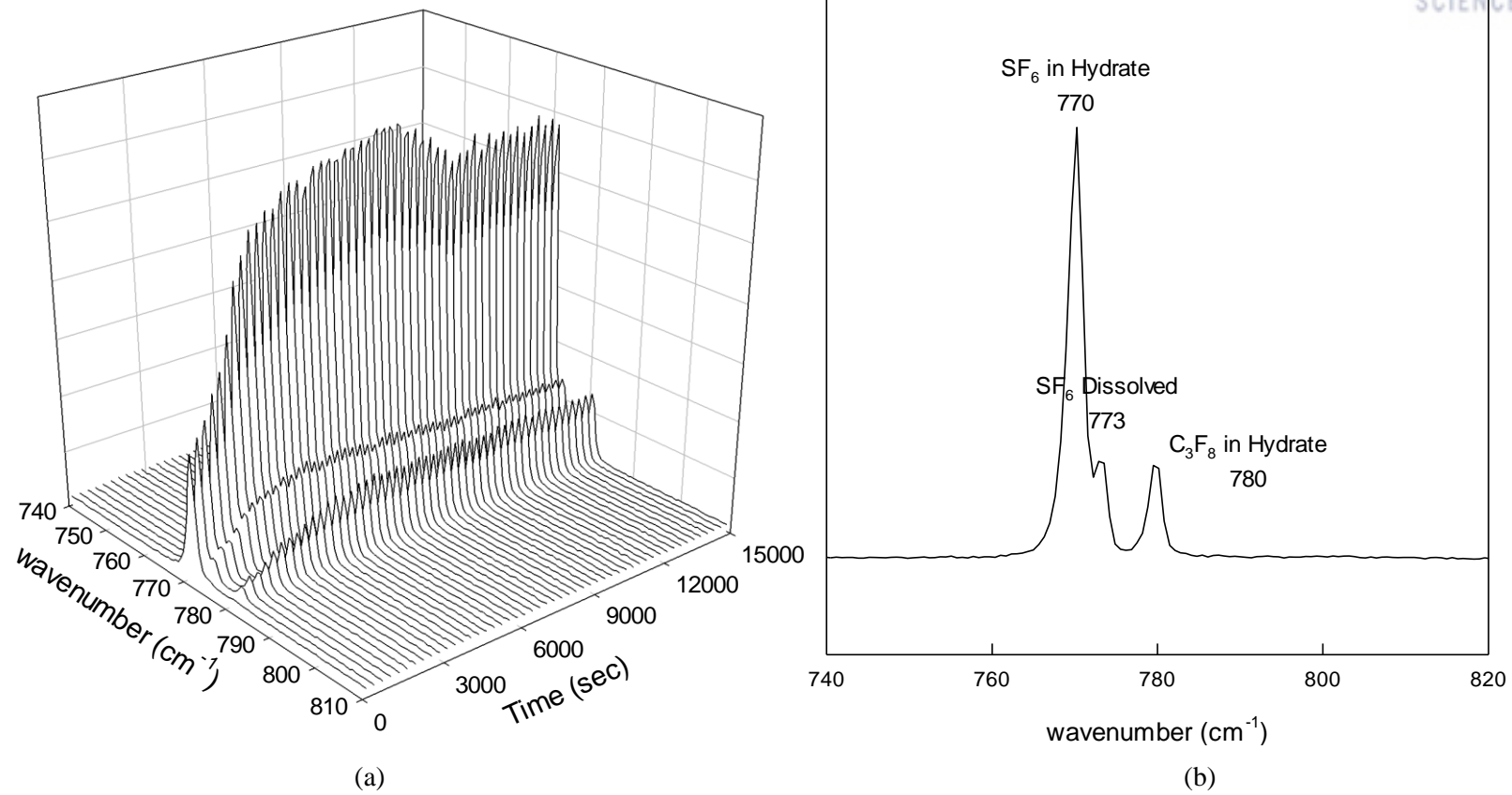


Figure 4.2.6. (a) Real time Raman spectra of C_3F_8 (25%) + SF_6 (75%) hydrate at 279.65 K and 1.05 MPa ($\Delta T=5$ K).

(b) Final Raman spectra of C_3F_8 (25%) + SF_6 (75%) hydrate at 279.65 K and 1.05 MPa ($\Delta T=5$ K).

4.2.5. Conclusions

In this study, the gas hydrate formation with C_3F_8 in presence of two different help gases (CH_4 and SF_6) were examined and the characteristics of formed gas hydrates were investigated. First, the three-phase (H-L_w-V) equilibria of $C_3F_8 + CH_4 +$ water and $C_3F_8 + SF_6 +$ water systems were measured. The thermodynamic phase equilibria suggested that C_3F_8 molecules participate in gas hydrate formation in presence of CH_4 or SF_6 molecules. Also, the thermodynamic equilibria curve shift with different C_3F_8 concentrations proved that C_3F_8 molecules exist as vapor phase, considering the Gibb's phase rule ($F = C - P + 2$). Next, the PXRD patterns of C_3F_8 (10%) + CH_4 (90%) and C_3F_8 (25, 50%) + SF_6 (75, 50%) hydrate crystals revealed that $C_3F_8 + CH_4$ gas mixture forms sH ($P6/mmm$) hydrate while $C_3F_8 + SF_6$ gas mixture forms sII ($Fd3m$) hydrate. From these results, it was verified that C_3F_8 can form both sH ($P6/mmm$) and sII ($Fd3m$) hydrates depending on help gas molecules. For sH hydrate formed from $C_3F_8 + CH_4$ mixture gas, it was expected that C_3F_8 molecules occupy large ($5^{12}6^8$) cages of sH hydrate while CH_4 molecules occupy small (5^{12}) and medium ($4^35^66^3$) cages considering the C_3F_8 molecular size. This suggestion was experimentally confirmed through ^{13}C NMR and Raman spectroscopy. From those spectroscopic results, CH_4 molecules were revealed to be enclathrated in both small (5^{12}) and medium ($4^35^66^3$) cages in sH hydrate, while there were CH_4 molecules captured in both small (5^{12}) and large ($5^{12}6^2$) cages in sI hydrate which was formed from residual CH_4 . The enclathration of C_3F_8 molecules in sII hydrate formation process in presence of SF_6 molecules as help gas was also demonstrated through *in-situ* Raman spectroscopy. Here, by observing the gas hydrate growth procedure, it was confirmed that the Raman peaks presented by C_3F_8 and SF_6 molecules increased simultaneously as gas hydrate growth proceeded. However, since C_3F_8 and SF_6 molecules are expected to compete to occupy large ($5^{12}6^4$) cages and it is more unfavorable for C_3F_8 because of its larger molecular size compared to SF_6 , the final Raman peak of C_3F_8 in hydrate phase appeared smaller than that of SF_6 . The overall experimental results obtained in this study gives a significant importance to gas hydrate science by discovering a dual former of sII and sH hydrates. The results are expected to be helpful to broaden the gas hydrate science and application fields.

Chapter 5. Conclusions and Future Perspectives

5.1. Conclusions

In this study, gas hydrate formation with representative fluorinated gases (CHF_3 , C_2F_6 and NF_3), and their potential application for gas hydrate-based fluorinated gas separation process were investigated with a primary focus on thermodynamic stability, spectroscopic characteristics, and cage-filling guest molecular behaviors. To obtain the fundamental thermodynamic stability range of gas hydrate phase formed with fluorinated gases, the three-phase (H-L_w-V) equilibria of pure F-gas (CHF_3 , C_2F_6 or NF_3) + water binary systems were measured, respectively. Also the three-phase (H-L_w-V) equilibria of F-gas (CHF_3 or C_2F_6) + N_2 + water ternary systems with various F-gas concentrations were examined to compare with the thermodynamic stability range of pure F-gas hydrates, and ultimately to estimate the feasibility of gas hydrate-based F-gas separation process. The microscopic properties of the representative three pure F-gas (CHF_3 , C_2F_6 and NF_3) hydrates and gas hydrates formed with those F-gases + N_2 mixture gases were investigated primarily through powder X-ray diffraction (PXRD), ^{13}C & ^{19}F NMR and (*in-situ*) Raman spectroscopy. The composition of gas and hydrate phases were analyzed via gas chromatography and compared to evaluate the separation efficiency of gas hydrate-based separation process. Lastly, computational calculation was conducted for specific F-gas hydrates, to elucidate the interactions between guest-guest or guest-host molecules.

This study also discovered new sH hydrate forming fluorinated gases (c- C_4F_8 and C_3F_8), in presence of suitable help gases (CH_4 or SF_6). Here, the three-phase (H-L_w-V) equilibria of F-gas (c- C_4F_8 or C_3F_8) + help gas (CH_4 or SF_6) + water ternary system were measured and compared with those of pure help gas (CH_4 or SF_6) + water binary system to thermodynamically demonstrate the participation of F-gases in gas hydrate formation process. Also, discovery of sH hydrate formation with large molecular F-gases (c- C_4F_8 and C_3F_8) was experimentally proved via various microscopic analyses such as PXRD, ^{13}C NMR and Raman spectroscopy.

From the thermodynamic and spectroscopic experimental results, it was concluded that gas hydrate-based separation process can be effectively applied for CHF_3 separation from CHF_3 + N_2 mixture gas. The thermodynamic stability range of CHF_3 + N_2 mixture gas hydrate gradually moved toward more favorable conditions (higher temperature and lower pressure) as CHF_3 concentration of the inlet gas increased. The crystal structure of pure CHF_3 and CHF_3 + N_2 mixture gas hydrates were examined as sI (*Pm3n*) regardless of CHF_3 concentrations used in this study. Also, the Raman spectroscopy revealed that CHF_3 molecules occupy both large ($5^{12}6^2$) and small (5^{12}) cages of sI (*Pm3n*) hydrate. The separation efficiency of CHF_3 molecules in hydrate phase by gas hydrate formation was directly evaluated by analyzing and comparing the compositions of gas phase versus hydrate phase using gas chromatography. Here, it was concluded that CHF_3 can be highly concentrated in gas hydrate phase (40%

CHF_3 can be concentrated up to 88% for example), and the separation efficiency becomes higher at lower temperature condition. From these results, a schematic suggestion for hybrid system of gas hydrate-based CHF_3 separation process combined with membrane/adsorption and liquefaction processes was devised.

On the other hand, gas hydrate-based separation process for C_2F_6 from $\text{C}_2\text{F}_6 + \text{N}_2$ mixture was revealed to be applicable only at low temperature conditions. From the thermodynamic phase equilibria, it was discovered that $\text{C}_2\text{F}_6 + \text{N}_2 + \text{water}$ ternary system shows azeotropic properties specifically at high temperature region and with high C_2F_6 concentration. Therefore, at high temperature region, separation of C_2F_6 in hydrate phase by gas hydrate formation was thermodynamically unfavorable. At low temperature condition (275.15 K), gas hydrate-based C_2F_6 separation was applicable as revealed from gradual thermodynamic equilibria curve movement according to increasing/decreasing C_2F_6 concentrations. From PXRD and Raman spectroscopy, the crystal structure of $\text{C}_2\text{F}_6 + \text{N}_2$ hydrates were identified as sII ($Fd3m$) regardless of the concentrations of C_2F_6 used in this study, with C_2F_6 occupying only large ($5^{12}6^4$) cages of sII ($Fd3m$) hydrates due to its large molecular size.

Lastly, fundamental thermodynamic and spectroscopic properties of pure NF_3 hydrate were examined in this study. Here, the thermodynamic stability condition of pure NF_3 hydrate was measured and concluded to be unfavorable for separation process, since NF_3 hydrate requires thermodynamically harsh conditions (high pressure and low temperature) to be formed. The crystal structure of pure NF_3 hydrate was examined as sI ($Pm3n$) and the NF_3 molecules were revealed to occupy both large ($5^{12}6^2$) and small (5^{12}) cages in hydrate phase.

The sH hydrate-forming gas-phase fluorinated molecules were first discovered in this study. In spite of the large molecular sizes of those fluorinated molecules (c- C_4F_8 and C_3F_8), they were proved to form gas hydrates if only there are suitable help gases such as CH_4 or SF_6 . The thermodynamic phase equilibria of c- $\text{C}_4\text{F}_8 + \text{CH}_4 + \text{water}$ system demonstrates c- C_4F_8 participation in gas hydrate formation by expressing the phase equilibria curve movement compared to that of pure $\text{CH}_4 + \text{water}$ system. Also, by showing different thermodynamic stability range according to different c- C_4F_8 concentrations, it was proved that there are three phases (gas hydrate (H), liquid water (L_w) and vapor (c- $\text{C}_4\text{F}_8 + \text{CH}_4$)) in the system, at each equilibria conditions. Since there have not been any vapor phase sH hydrate former (large molecule) known until present, this discovery has a significant importance for gas hydrate science. The formation of sH ($P6/mmm$) hydrate was confirmed through PXRD and ^{13}C NMR spectroscopy. Due to its large molecular size, c- C_4F_8 was revealed to only occupy large ($5^{12}6^8$) cages while CH_4 occupies medium ($4^35^66^3$) and small (5^{12}) cages.

C_3F_8 was also confirmed to form gas hydrate, but only with CH_4 or SF_6 as help gas, as demonstrated from the thermodynamic equilibria curve movement compared to those of the pure help gas (CH_4 or SF_6) hydrates. However, it was discovered through PXRD analysis that the crystal structure formed by $\text{C}_3\text{F}_8 + \text{help gas}$ (CH_4 or SF_6) was sH ($P6/mmm$) and sII ($Fd3m$) respectively. The ^{13}C NMR and Raman

spectroscopy proved the formation of sH ($P6/mmm$) hydrate from $C_3F_8 + CH_4$ mixture gas, by presenting CH_4 molecules captured in medium ($4^35^66^3$) and small (5^{12}) cages while C_3F_8 molecules are enclathrated in only large ($5^{12}6^8$) cages. On the other hand, the inclusion of C_3F_8 molecules in large ($5^{12}6^4$) cages of sII ($Fd3m$) hydrate phase in presence of SF_6 hydrate was demonstrated via in-situ Raman spectroscopy.

The overall experimental and computational results obtained in this study are expected to give insight for feasibility of gas hydrate-based separation process for various gases, and broaden the gas hydrate science by proposing newly discovered gas-phase sH hydrate formers.

5.2. Future Perspectives

From the results in Chapter 3.2 and 3.3, the feasibility of gas hydrate-based F-gas separation process was experimentally examined. However, the practical estimation on gas hydrate-based separation process by comparing with other separation methods or calculating the energy required to operate the process has not been proved through this study. Therefore, it is necessary to study how to pragmatize gas hydrate-based F-gas separation process in the real industrial field. As a part of it, this study investigated and compared the thermodynamic F-gas separation efficiency of gas hydrate-based separation process with that of liquefaction process, using CHF₃ as a representative example. Since F-gases are easily liquefied due to their low vapor pressures, liquefaction process is one of commonly used separation methods to gain highly purified F-gas in the industrial fields. Herein, the thermodynamic separation efficiency was calculated using pressure-composition diagram shown in Figure 3.2.3 and liquid-vapor equilibrium of CHF₃ + N₂ at specific temperature conditions [29, 91, 92]. Figure 5.2.1 (a) and (b) shows the CHF₃ recovery ratio in gas hydrate cages or liquid phase according to CHF₃ mole fractions in feed CHF₃ + N₂ gas mixture at an identical pressure condition (4.0 MPa) and two different temperature conditions (279.15 K and 283.15 K). It is clearly seen from the calculation that gas hydrate-based CHF₃ separation process starts to concentrate CHF₃ in hydrate phase at around 0.2 CHF₃ mole fraction, while liquefaction starts to be effective at least with 0.8 CHF₃ mole fraction in the feed gas. Also, it is seen that gas hydrate-based CHF₃ separation process can obtain pure CHF₃ recovery with about 0.8 CHF₃ mole fraction in the feed gas, while liquefaction requires pure CHF₃ to gain a full recovery of CHF₃. Figure 5.2.2 (a) and (b) compared the CHF₃ recovery ratio with identical CHF₃ mole fraction in feed gas at specific temperature conditions (279.15 K and 283.15 K). In Figure 5.2.2 (a), it is seen that CHF₃ starts to be concentrated in gas hydrate phase from about 2.0 MPa at 283.15 K, whereas liquefaction of CHF₃ + N₂ gas mixture with 0.4 mole fraction starts from 8.0 MPa. Also, while gas hydrate formation can obtain almost pure CHF₃ in the hydrate phase at high pressure condition (10MPa), the recovery ratio of CHF₃ through liquefaction is significantly low compared to gas hydrate formation method. From the calculation results shown above, it is concluded that gas hydrate-based separation process shows significantly higher CHF₃ recovery ratio compared to liquefaction process at identical pressure condition or with identical CHF₃ mole fraction in feed gas. Moreover, it is clearly demonstrated that lower temperature condition gives higher thermodynamic separation efficiency for both separation methods.

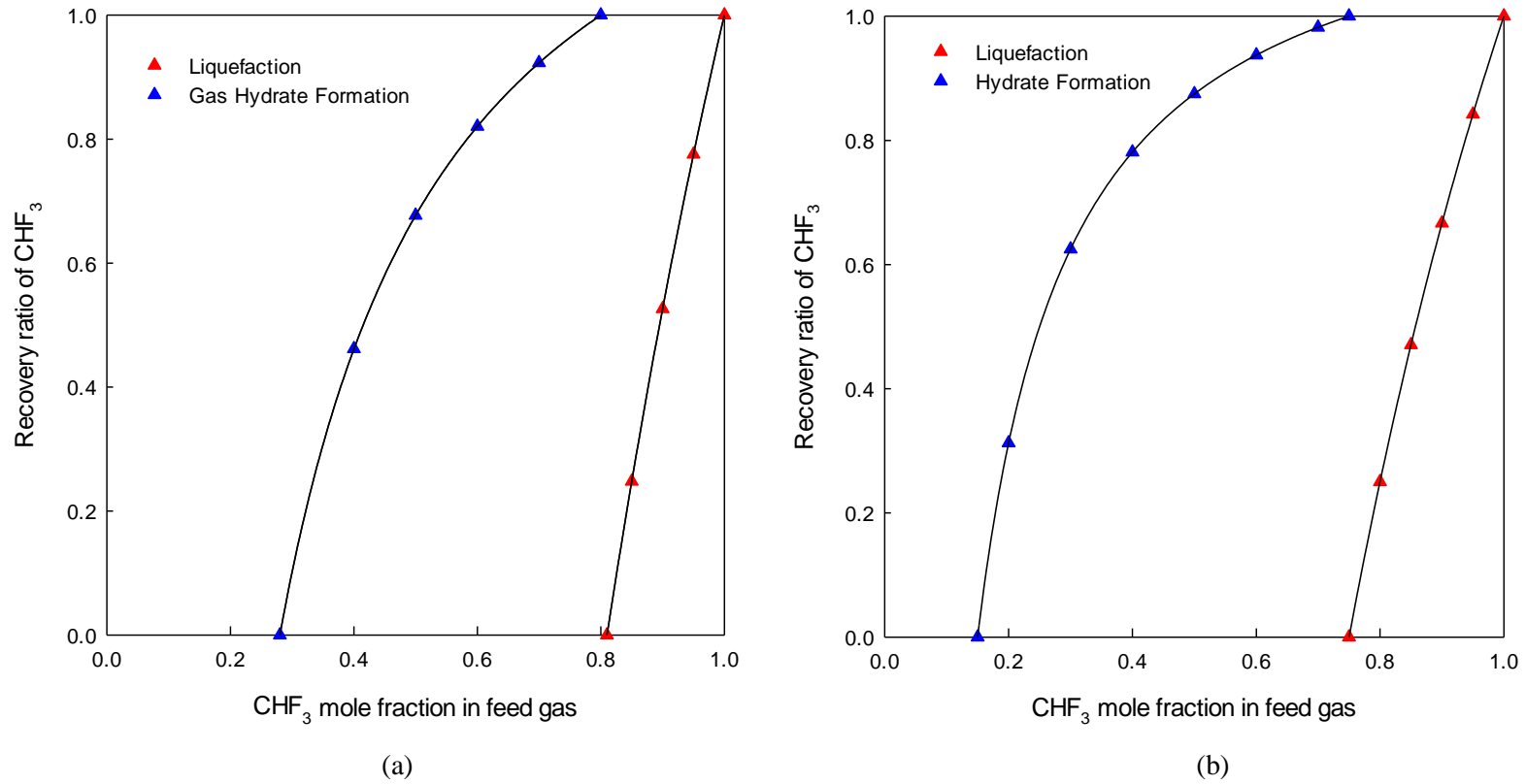


Figure 5.2.1. Comparison of thermodynamic CHF_3 separation efficiency between gas hydrate formation and liquefaction processes.

(a) Effect of CHF_3 mole fraction in feed gas at 283.15 K and 4.0 MPa.

(b) Effect of CHF_3 mole fraction in feed gas at 279.15 K and 4.0 MPa.

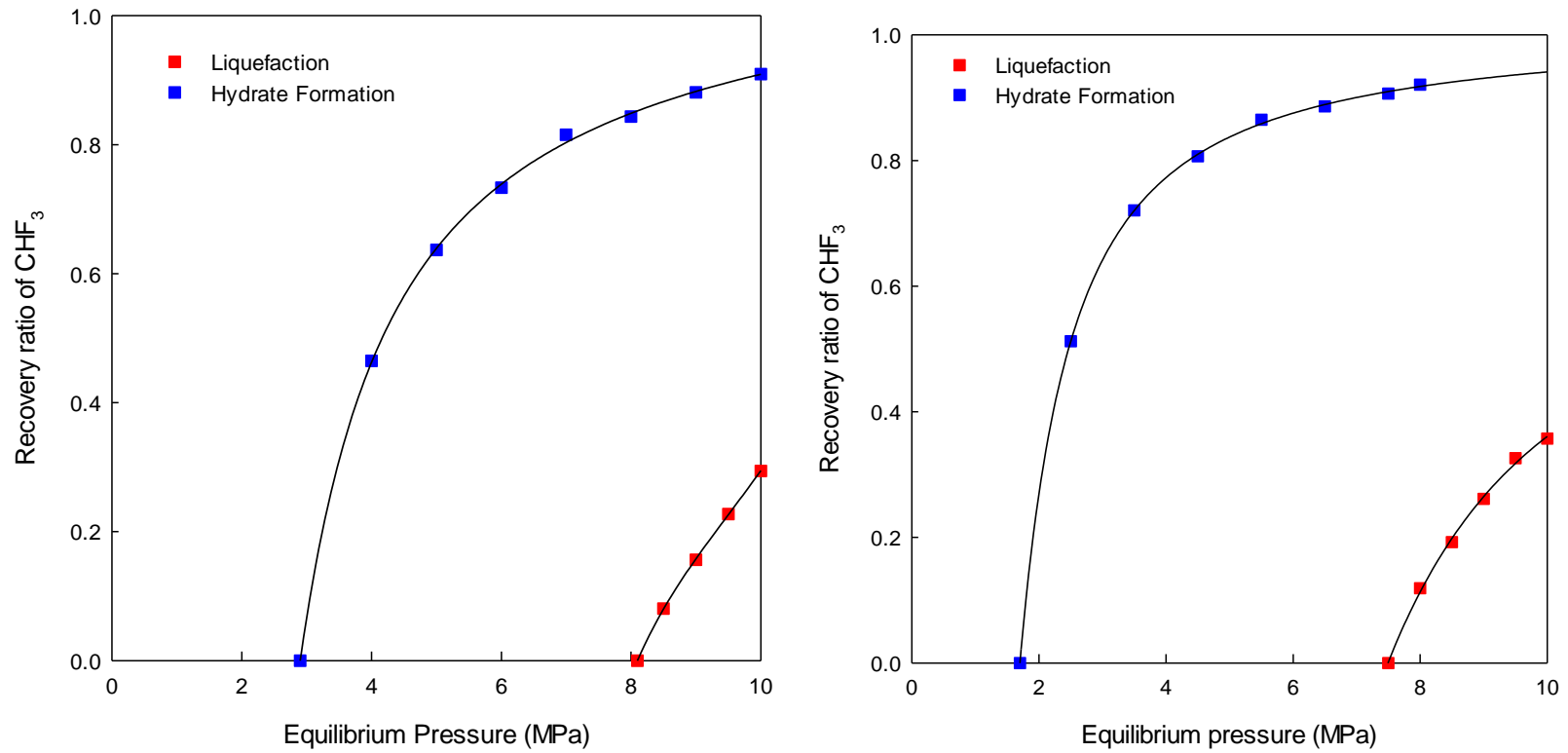


Figure 5.2.2. Comparison of thermodynamic CHF₃ separation efficiency between gas hydrate formation and liquefaction processes.

(a) Effect of pressure with CHF₃ mole fraction of 0.4 at 283.15 K.

(b) Effect of pressure with CHF₃ mole fraction of 0.4 at 279.15 K.

Another approach to gain fundamental information for practicality evaluation was the energy measurement which is required for the hydrate formation reaction. Herein, a high-pressure micro-differential scanning calorimeter (HP IDSC, VII Evo, Setaram Inc., France) was used to confirm the formation of pure F-gas (CHF_3 or C_2F_6) hydrate from the F-gas + water mixture. The HP μ -DSC can operate at up to 40 MPa in a temperature range of 233.15– 393.15 K. The HP μ -DSC has a resolution of 0.02 μ W with temperature deviation of ± 0.2 K. A multi-cycle mode of cooling-heating was adopted for with 25 mg of pure water at the desired pressure in order to enhance the conversion of the F-gas hydrate. A more detailed description of the experimental methods can be found in our previous papers [85, 86]. Figure 5.2.3 shows the representative configuration of F-gas hydrate dissociation process through which the enthalpy required for complete conversion of water to F-gas hydrate is calculated. In Figure 5.2.3, one endothermic peak which correspond to pure CHF_3 hydrate dissociation is clearly shown and integrated the overall enthalpy required for the hydrate formation reaction to occur. The enthalpy required for the complete conversion of water to pure C_2F_6 hydrate was measured in the same way. The enthalpy measurements were conducted at least five times to obtain reliable data for respective pure F-gas hydrate. From the experimental results, the dissociation enthalpy values of pure CHF_3 and C_2F_6 hydrates were 70.1 (± 0.3) kJ/mol CHF_3 and 127.9 (± 0.6) kJ/mol C_2F_6 , respectively. It is meaningful that the dissociation enthalpies of both pure CHF_3 and C_2F_6 hydrates were first measured in this study, and the values obtained here are similar to those of common sI and sII hydrates.

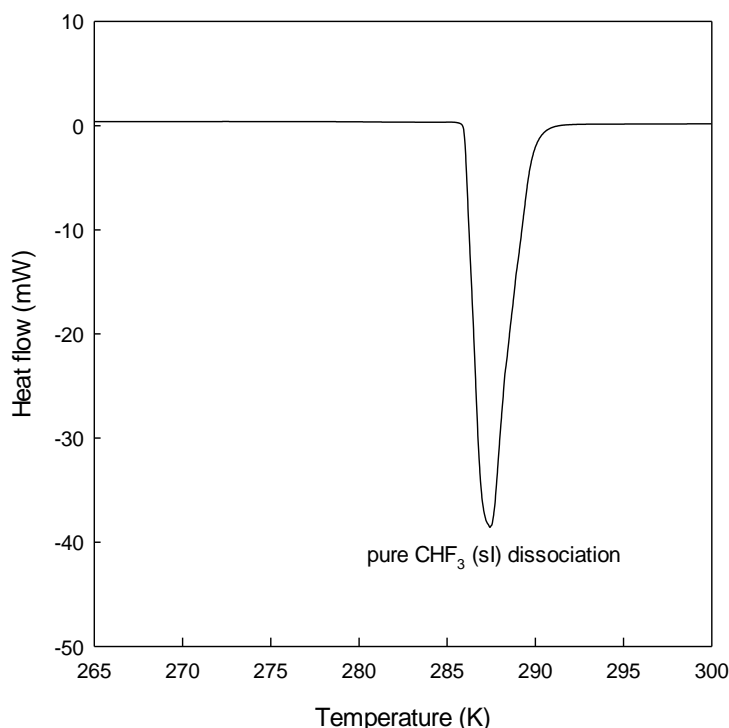


Figure 5.2.3. Hydrate dissociation thermogram for pure CHF_3 + water system at 1.8 MPa with a heating rate of 1 K/min.

In conclusion, this study obtained two valuable results for further application of gas hydrate-based separation process in industrial fields. However, it is true that these lab-scale experimental data are not sufficient to construct overall process schematic diagram. Therefore, there are remaining future works which have to be dealt with, such as calculation of energy required for process operation and test operation of scaled-up process in overall (Figure 5.2.4). Membrane adsorption and liquefaction process have been suggested for pre and post processes for the gas hydrate-based separation process until present, but further development of those processes to maximize the recovery ratio and purity of F-gas while minimizing the process expenditure. Also, process design including determination of sequence of the overall process as well as the agitator, shape, material of the process and energy calculation required for temperature and pressure maintenance should be further conducted. Especially, considering that gas hydrate formation with bulky water is kinetically unfavorable, the addition of kinetic promoters such as surfactants should be studied and tested. Lastly, the operation test with scaled-up model process would support examination on the feasibility of the overall process. With those engineering optimization enhanced, it is highly expected that gas hydrate-based F-gas separation process will become an effective and practical gas separation method in real industries.

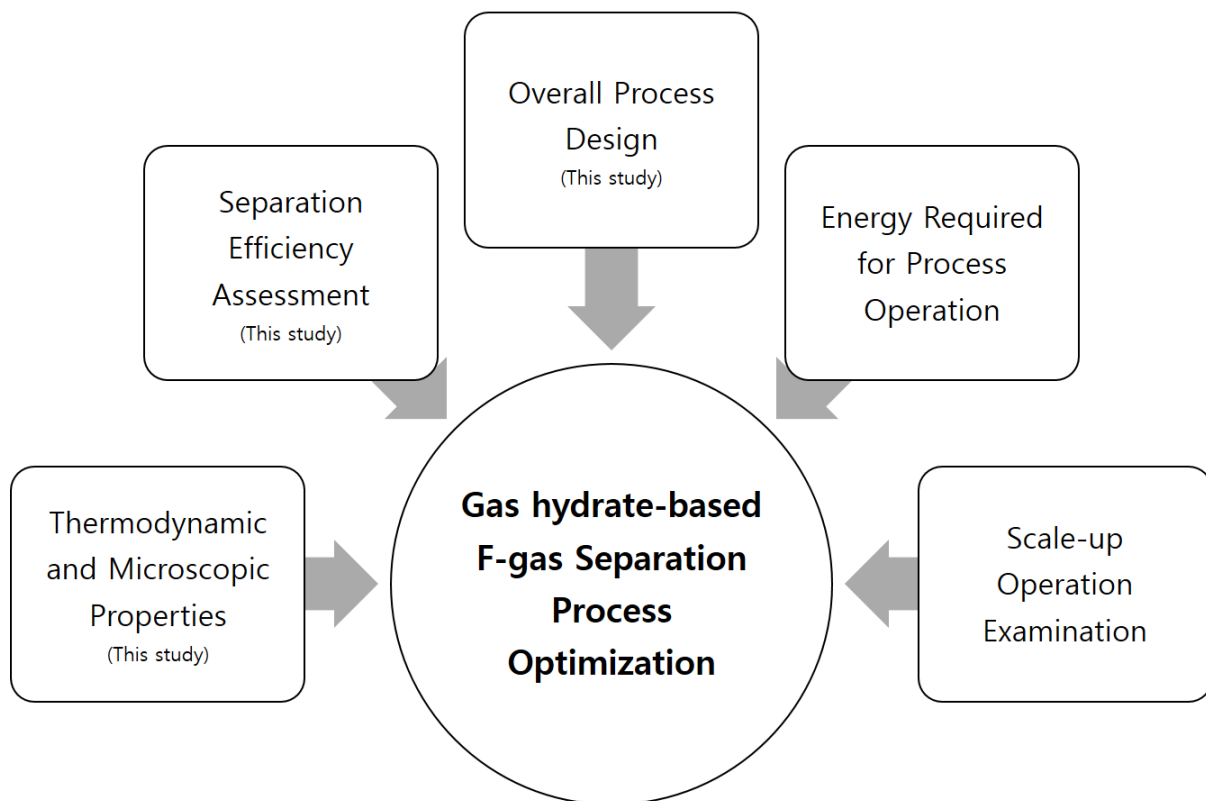


Figure 5.2.4. Overall works required for overall gas hydrate-based F-gas separation process optimization.

References

- [1] E.D. Sloan, C.A. Koh, Clathrate Hydrates of Natural Gases Third Edition, CHEMICAL INDUSTRIES-NEW YORK THEN BOCA RATON-MARCEL DEKKER THEN CRC PRESS 119 (2008).
- [2] E.D. Sloan Jr, Fundamental principles and applications of natural gas hydrates, *Nature* 426 (2003) 353.
- [3] J.S. Gudmundsson, M. Parlaktuna, A.A. Khokhar, Storing Natural-Gas as Frozen Hydrate, *SPE Prod. Facil.* 9 (1994) 69-73.
- [4] A.A. Khokhar, J.S. Gudmundsson, E.D. Sloan, Gas storage in structure H hydrates, *Fluid Phase Equilib.* 150-151 (1998) 383-392.
- [5] Z.G. Sun, R. Wang, R. Ma, K. Guo, S. Fan, Natural gas storage in hydrates with the presence of promoters, *Energy Convers. Manage.* 44 (2003) 2733-2742.
- [6] W. Hao, J. Wang, S. Fan, W. Hao, Evaluation and analysis method for natural gas hydrate storage and transportation processes, *Energy Convers. Manage.* 49 (2008) 2546-2553.
- [7] R. Kumar, P. Linga, I. Moudrakovski, J.A. Ripmeester, P. Englezos, Structure and kinetics of gas hydrates from methane/ethane/propane mixtures relevant to the design of natural gas hydrate storage and transport facilities, *AIChE J.* 54 (2008) 2132-2144.
- [8] S.P. Kang, H. Lee, Recovery of CO₂ from flue gas using gas hydrate: thermodynamic verification through phase equilibrium measurements, *Environ. Sci. Technol.* 34 (2000) 4397-4400.
- [9] P. Linga, R. Kumar, P. Englezos, The clathrate hydrate process for post and pre-combustion capture of carbon dioxide, *Journal of hazardous materials* 149 (2007) 625-629.
- [10] N.H. Duc, F. Chauvy, J.M. Herri, CO₂ capture by hydrate crystallization—A potential solution for gas emission of steelmaking industry, *Energy Convers. Manage.* 48 (2007) 1313-1322.
- [11] X.S. Li, C.G. Xu, Z.Y. Chen, H.J. Wu, Hydrate-based pre-combustion carbon dioxide capture process in the system with tetra-n-butyl ammonium bromide solution in the presence of cyclopentane, *Energy* 36 (2011) 1394-1403.
- [12] S. Park, S. Lee, Y. Lee, Y. Seo, CO₂ capture from simulated fuel gas mixtures using semiclathrate hydrates formed by quaternary ammonium salts, *Environ. Sci. Technol.* 47 (2013) 7571-7577.
- [13] P. Babu, R. Kumar, P. Linga, Pre-combustion capture of carbon dioxide in a fixed bed reactor using the clathrate hydrate process, *Energy* 50 (2013) 364-373.
- [14] S. Kim, S.P. Kang, Y. Seo, Semiclathrate-based CO₂ capture from flue gas in the presence of tetra-n-butyl ammonium chloride (TBAC), *Chem. Eng. J.* 276 (2015) 205-212.
- [15] Z.M. Xia, X.S. Li, Z.Y. Chen, G. Li, K.F. Yan, C.G. Xu, Q.N. Lv, J. Cai, Hydrate-based CO₂ capture and CH₄ purification from simulated biogas with synergic additives based on gas solvent, *Appl. Energy*

162 (2016) 1153-1159.

[16] S. Kim, S.D. Choi, Y. Seo, CO₂ capture from flue gas using clathrate formation in the presence of thermodynamic promoters, *Energy* 118 (2017) 950-956.

[17] H. Lee, Y. Seo, Y.T. Seo, I.L. Moudrakovski, J.A. Ripmeester, Recovering methane from solid methane hydrate with carbon dioxide, *Angew. Chem.* 115 (2003) 5202-5205.

[18] M. Ota, K. Morohashi, Y. Abe, M. Watanabe, R.L. Smith Jr, H. Inomata, Replacement of CH₄ in the hydrate by use of liquid CO₂, *Energy Convers. Manage.* 46 (2005) 1680-1691.

[19] S. Lee, Y. Lee, J. Lee, H. Lee, Y. Seo, Experimental verification of methane-carbon dioxide replacement in natural gas hydrates using a differential scanning calorimeter, *Environ. Sci. Technol.* 47 (2013) 13184-13190.

[20] K.N. Park, S.Y. Hong, J.W. Lee, K.C. Kang, Y.C. Lee, M.G. Ha, J.D. Lee, A new apparatus for seawater desalination by gas hydrate process and removal characteristics of dissolved minerals (Na⁺, Mg²⁺, Ca²⁺, K⁺, B³⁺), *Desalination* 274 (2011) 91-96.

[21] J.H. Cha, Y. Seol, Increasing gas hydrate formation temperature for desalination of high salinity produced water with secondary guests, *ACS Sustainable Chem. Eng.* 1 (2013) 1218-1224.

[22] S. Han, J.Y. Shin, Y.W. Rhee, S.P. Kang, Enhanced efficiency of salt removal from brine for cyclopentane hydrates by washing, centrifuging, and sweating, *Desalination* 354 (2014) 17-22.

[23] K.C. Kang, P. Linga, K.N. Park, S.J. Choi, J.D. Lee, Seawater desalination by gas hydrate process and removal characteristics of dissolved ions (Na⁺, K⁺, Mg²⁺, Ca²⁺, B³⁺, Cl⁻, SO₄²⁻), *Desalination* 353 (2014) 84-90.

[24] J.N. Zheng, M.J. Yang, Y. Liu, D.Y. Wang, Y.C. Song, Effects of cyclopentane on CO₂ hydrate formation and dissociation as a co-guest molecule for desalination, *J. Chem. Thermodyn.* 104 (2017) 9-15.

[25] M. Mooijer-van den Heuvel, C. Peters, J. de Swaan Arons, Influence of water-insoluble organic components on the gas hydrate equilibrium conditions of methane, *Fluid Phase Equilib.* 172 (2000) 73-91.

[26] Y. Seo, H. Tajima, A. Yamasaki, S. Takeya, T. Ebinuma, F. Kiyono, A new method for separating HFC-134a from gas mixtures using clathrate hydrate formation, *Environ. Sci. Technol.* 38 (2004) 4635-4639.

[27] K. Sugahara, M. Yoshida, T. Sugahara, K. Ohgaki, High-pressure phase behavior and cage occupancy for the CF₄ hydrate system, *J. Chem. Eng. Data* 49 (2004) 326-329.

[28] E.K. Lee, J.D. Lee, H.J. Lee, B.R. Lee, Y.S. Lee, S.M. Kim, H.O. Park, Y.S. Kim, Y.D. Park, Y.D. Kim, Pure SF₆ and SF₆-N₂ mixture gas hydrates equilibrium and kinetic characteristics, *Environ. Sci. Technol.* 43 (2009) 7723-7727.

[29] T. Nagata, H. Tajima, A. Yamasaki, F. Kiyono, Y. Abe, An analysis of gas separation processes of HFC-134a from gaseous mixtures with nitrogen—Comparison of two types of gas separation methods,

liquefaction and hydrate-based methods, in terms of the equilibrium recovery ratio, *Sep. Purifi. Technol.* 64 (2009) 351-356.

[30] I. Cha, S. Lee, J.D. Lee, G.W. Lee, Y. Seo, Separation of SF₆ from gas mixtures using gas hydrate formation, *Environ. Sci. Technol.* 44 (2010) 6117-6122.

[31] A. Ravishankara, S. Solomon, A.A. Turnipseed, R. Warren, Atmospheric lifetimes of long-lived halogenated species, *Science* 259 (1993) 194-199.

[32] C. Roehl, D. Boglu, C. Brühl, G. Moortgat, Infrared band intensities and global warming potentials of CF₄, C₂F₆, C₃F₈, C₄F₁₀, C₅F₁₂, and C₆F₁₄, *Geophys. Res. Lett.* 22 (1995) 815-818.

[33] D. Oram, W. Sturges, S. Penkett, A. McCulloch, P. Fraser, Growth of fluoroform (CHF₃, HFC-23) in the background atmosphere, *Geophys. Res. Lett.* 25 (1998) 35-38.

[34] M.B. Chang, S.J. Yu, An atmospheric-pressure plasma process for C₂F₆ removal, *Environ. Sci. Technol.* 35 (2001) 1587-1592.

[35] W.T. Tsai, H.P. Chen, W.Y. Hsien, A review of uses, environmental hazards and recovery/recycle technologies of perfluorocarbons (PFCs) emissions from the semiconductor manufacturing processes, *J. Loss Prev. Process Ind.* 15 (2002) 65-75.

[36] A. McCulloch, Fluorocarbons in the global environment: a review of the important interactions with atmospheric chemistry and physics, *J. Fluorine Chem.* 123 (2003) 21-29.

[37] J. Wijmans, Z. He, T. Su, R. Baker, I. Pinnau, Recovery of perfluoroethane from chemical vapor deposition operations in the semiconductor industry, *Sep. Purifi. Technol.* 35 (2004) 203-213.

[38] P. Kowalczyk, R. Holyst, Efficient adsorption of super greenhouse gas (tetrafluoromethane) in carbon nanotubes, *Environ. Sci. Technol.* 42 (2008) 2931-2936.

[39] X. Zhang, X. Zhao, J. Hu, C. Wei, H.T. Bi, Adsorption dynamics of trichlorofluoromethane in activated carbon fiber beds, *J. Hazard. Mater.* 186 (2011) 1816-1822.

[40] Z. Du, S. Deng, Y. Bei, Q. Huang, B. Wang, J. Huang, G. Yu, Adsorption behavior and mechanism of perfluorinated compounds on various adsorbents—a review, *J. Hazard. Mater.* 274 (2014) 443-454.

[41] I.-J. Chung, K.R. Lee, S.T. Hwang, Separation of CFC-12 from air by polyimide hollow-fiber membrane module, *J. Membr. Sci.* 105 (1995) 177-185.

[42] Y. Hirayama, N. Tanihara, Y. Kusuki, Y. Kase, K. Haraya, K.-i. Okamoto, Permeation properties to hydrocarbons, perfluorocarbons and chlorofluorocarbons of cross-linked membranes of polymethacrylates with poly (ethylene oxide) and perfluorononyl moieties, *J. Membr. Sci.* 163 (1999) 373-381.

[43] H. Kubota, K. Shimizu, Y. Tanaka, T. Makita, Thermodynamic properties of R13 (CClF₃), R23 (CHF₃), R152a (C₂H₄F₂), and propane hydrates for desalination of sea water, *J. Chem. Eng. Jpn.* 17 (1984) 423-429.

[44] T. Sugahara, K. Ohgaki, Border gas hydrate system having quadruple point of hydrate+ two liquids+ gas phases, *J. Chem. Eng. Jpn.* 33 (2000) 174-176.

- [45] H. Hashemi, S. Babae, P. Naidoo, A.H. Mohammadi, D. Ramjugernath, Experimental measurements and thermodynamic modeling of clathrate hydrate dissociation conditions for refrigerants R116, R23, and their mixture R508B, *J. Chem. Eng. Data* 59 (2014) 3907-3911.
- [46] M. Mooijer-van den Heuvel, N. Sawirjo, C. Peters, Influence of fluoroalkanes on the phase behaviour of methane gas hydrate systems, *Fluid Phase Equilib.* 241 (2006) 124-137.
- [47] D.H. Brouwer, E.B. Brouwer, G. Maclaurin, M. Lee, D. Parks, J.A. Ripmeester, Some New Halogen-containing Hydrate-formers for Structure I and II Clathrate Hydrates¹, *Supramol. Chem.* 8 (1997) 361-367.
- [48] S. Takeya, K.A. Udachin, I.L. Moudrakovski, R. Ohmura, J.A. Ripmeester, Disorder of hydrofluorocarbon molecules entrapped in the water cages of structure I clathrate hydrate, *Chem. Eur. J.* 22 (2016) 7567-7573.
- [49] T. Uchida, R. Ohmura, A. Hori, Critical size for guest molecules to occupy dodecahedral cage of clathrate hydrates, *J Phys. Chem. C* 112 (2008) 4719-4724.
- [50] T. Uchida, R. Ohmura, A. Hori, Raman peak frequencies of fluoromethane molecules measured in clathrate hydrate crystals: experimental investigations and density functional theory calculations, *The Journal of Physical Chemistry A* 114 (2009) 317-323.
- [51] Y. Wu, M. Onomichi, S. Sasaki, H. Shimizu, High-pressure Raman study of liquid and crystalline CHF_2Cl and CHF_3 , *J. Raman Spectro.* 24 (1993) 845-849.
- [52] T. Makino, Y. Kunitab, T. Sugaharab, K. Ohgakib, Isothermal phase equilibria and cage occupancies for $\text{CH}_4 + \text{CHF}_3$ mixed-gas hydrate system, *Open Thermodyn. J.* 2 (2008) 17-21.
- [53] M.T. Kirchner, R. Boese, W.E. Billups, L.R. Norman, Gas hydrate single-crystal structure analyses, *J. Ame. Chem.Soc.* 126 (2004) 9407-9412.
- [54] M. Segall, P.J. Lindan, M.a. Probert, C.J. Pickard, P.J. Hasnip, S. Clark, M. Payne, First-principles simulation: ideas, illustrations and the CASTEP code, *J. Phys. Cond. Mat.* 14 (2002) 2717.
- [55] S.J. Clark, M.D. Segall, C.J. Pickard, P.J. Hasnip, M.I. Probert, K. Refson, M.C. Payne, First principles methods using CASTEP, *Zeitschrift für Kristallographie-Crystalline Materials* 220 (2005) 567-570.
- [56] J.P. Perdew, K. Burke, M. Ernzerhof, Generalized gradient approximation made simple, *Phys. Rev. Lett.* 77 (1996) 3865.
- [57] B. Delley, An all-electron numerical method for solving the local density functional for polyatomic molecules, *J. Chem. Phys.* 92 (1990) 508-517.
- [58] B. Delley, From molecules to solids with the DMol 3 approach, *J. Chem. Phys.* 113 (2000) 7756-7764.
- [59] N. Metropolis, A.W. Rosenbluth, M.N. Rosenbluth, A.H. Teller, E. Teller, Equation of state calculations by fast computing machines, *J. Chem. Phys.* 21 (1953) 1087-1092.
- [60] J.I. Siepmann, D. Frenkel, Configurational bias Monte Carlo: a new sampling scheme for flexible

chains, *Mol. Phys.* 75 (1992) 59-70.

[61] H. Sun, COMPASS: an ab initio force-field optimized for condensed-phase applications overview with details on alkane and benzene compounds, *J. Phys. Chem. B* 102 (1998) 7338-7364.

[62] A. Van Cleeff, G. Diepen, Gas hydrates of nitrogen and oxygen, *Recueil Des Travaux Chimiques Des Pays-Bas* 79 (1960) 582-586.

[63] E. Kim, E. Shin, G. Ko, S.H. Kim, O.H. Han, S.K. Kwak, Y. Seo, Enclathration of CHF₃ and C₂F₆ molecules in gas hydrates for potential application in fluorinated gas (F-gas) separation, *Chem. Eng. J.* 306 (2016) 298-305.

[64] S. Sasaki, S. Hori, T. Kume, H. Shimizu, Microscopic observation and in situ Raman scattering studies on high-pressure phase transformations of a synthetic nitrogen hydrate, *J. Chem. Phys.* 118 (2003) 7892-7897.

[65] M. Heuchel, R.Q. Snurr, E. Buss, Adsorption of CH₄-CF₄ mixtures in silicalite: simulation, experiment, and theory, *Langmuir* 13 (1997) 6795-6804.

[66] K. Shiojiri, Y. Yanagisawa, A. Yamasaki, F. Kiyono, Separation of F-gases (HFC-134a and SF₆) from gaseous mixtures with nitrogen by surface diffusion through a porous Vycor glass membrane, *J. Membr. Sci.* 282 (2006) 442-449.

[67] P. Babu, T. Yang, H.P. Veluswamy, R. Kumar, P. Linga, Hydrate phase equilibrium of ternary gas mixtures containing carbon dioxide, hydrogen and propane, *J. Chem. Thermodyn.* 61 (2013) 58-63.

[68] T. Sugahara, T. Makino, K. Ohgaki, Isothermal phase equilibria for the methane+ ethylene mixed gas hydrate system, *Fluid Phase Equilib.* 206 (2003) 117-126.

[69] T. Maekawa, Phase equilibria for hydrate formation from binary mixtures of ethane, propane and noble gases, *Fluid Phase Equilib.* 243 (2006) 115-120.

[70] H. Miyauchi, K. Yasuda, Y. Matsumoto, S. Hashimoto, T. Sugahara, K. Ohgaki, Isothermal phase equilibria for the (HFC-32+ HFC-134a) mixed-gas hydrate system, *J. Chem. Thermodyn.* 47 (2012) 1-5.

[71] T. Sugahara, H. Miyauchi, S. Suzuki, Y. Matsumoto, K. Yasuda, T. Makino, K. Ohgaki, Isothermal phase equilibria for the (xenon+ cyclopropane) mixed-gas hydrate system, *J. Chem. Thermodyn.* 47 (2012) 13-16.

[72] D. Davidson, S. Garg, C. Ratcliffe, J. Tse, S. Gough, Characterization of a clathrate hydrate of nitrogen trifluoride, *Can. J. Chem.* 62 (1984) 1229-1235.

[73] K. Shin, K.A. Udachin, I.L. Moudrakovski, D.M. Leek, S. Alavi, C.I. Ratcliffe, J.A. Ripmeester, Methanol incorporation in clathrate hydrates and the implications for oil and gas pipeline flow assurance and icy planetary bodies, *Proc. Natl. Acad. Sci.* 110 (2013) 8437-8442.

[74] S. Takeya, H. Fujihisa, A. Hachikubo, H. Sakagami, Y. Gotoh, Distribution of butane in the host water cage of structure II clathrate hydrates, *Chem. Euro. J.* 20 (2014) 17207-17213.

[75] S. Takeya, K.A. Udachin, I.L. Moudrakovski, R. Susilo, J.A. Ripmeester, Direct space methods for

powder X-ray diffraction for guest– host materials: applications to cage occupancies and guest distributions in clathrate hydrates, *J. Ame. Chem. Soc.* 132 (2009) 524-531.

[76] M. Gilbert, P. Nectoux, M. Drifford, The Raman spectrum of NF_3 : Coriolis coupling and transition dipole interaction in the liquid, *J. Chem. Phys.* 68 (1978) 679-691.

[77] J. Ripmeester, C. Ratcliffe, Low-temperature cross-polarization/magic angle spinning carbon-13 NMR of solid methane hydrates: structure, cage occupancy, and hydration number, *J. Phys. Chem.* 92 (1988) 337-339.

[78] Y.T. Seo, H. Lee, ^{13}C NMR analysis and gas uptake measurements of pure and mixed gas hydrates: Development of natural gas transport and storage method using gas hydrate, *Korean J. Chem. Eng.* 20 (2003) 1085-1091.

[79] S. Adisasmito, R.J. Frank III, E.D. Sloan Jr, Hydrates of carbon dioxide and methane mixtures, *J. Chem. Eng. Data* 36 (1991) 68-71.

[80] W. Shin, S. Park, D.Y. Koh, J. Seol, H. Ro, H. Lee, Water-soluble structure H clathrate hydrate formers, *J. Phys. Chem. C* 115 (2011) 18885-18889.

[81] J. Lederhos, A. Mehta, G. Nyberg, K. Warn, E. Sloan, Structure H clathrate hydrate equilibria of methane and adamantane, *AIChE journal* 38 (1992) 1045-1048.

[82] Y. Jin, M. Kida, J. Nagao, Structure H (sH) clathrate hydrate with new large molecule guest substances, *J. Phys. Chem. C* 117 (2013) 23469-23475.

[83] E. Kim, Y.K. Jin, Y. Seo, Structural transition and phase behavior of N_2 gas hydrates with pinacolyl alcohol and tert-amyl alcohol, *Fluid Phase Equilib.* 393 (2015) 85-90.

[84] E. Kim, G. Ko, Y. Seo, Greenhouse Gas (CHF_3) Separation by gas hydrate formation, *ACS Sustainable Chem. Eng.* 5 (2017) 5485-5492.

[85] E. Kim, S. Lee, J.D. Lee, Y. Seo, Influences of large molecular alcohols on gas hydrates and their potential role in gas storage and CO_2 sequestration, *Chem. Eng. J.* 267 (2015) 117-123.

[86] E. Kim, S. Lee, J.D. Lee, Y. Seo, Enclathration of tert-butyl alcohol in sII hydrates and its implications in gas storage and CO_2 sequestration, *Fuel* 164 (2016) 237-244.

[87] K. Sugahara, M. Yoshida, T. Sugahara, K. Ohgaki, Thermodynamic and Raman spectroscopic studies on pressure-induced structural transition of SF_6 hydrate, *J. Chem. Eng. Data* 51 (2006) 301-304.

[88] R. Susilo, J. Lee, P. Englezos, Liquid–liquid equilibrium data of water with neohexane, methylcyclohexane, tert-butyl methyl ether, n-heptane and vapor–liquid–liquid equilibrium with methane, *Fluid Phase Equilib.* 231 (2005) 20-26.

[89] T. Uchida, R. Ohmura, I.Y. Ikeda, J. Nagao, S. Takeya, A. Hori, Phase Equilibrium Measurements and Crystallographic Analyses on Structure-H Type Gas Hydrate Formed from the CH_4 – CO_2 – Neohexane– Water System, *J. Phys. Chem. B* 110 (2006) 4583-4588.

[90] E. Pace, A. Plaush, H. Samuelson, Vibrational spectra and frequency assignments for octafluoropropane (C_3F_8) and hexafluoroacetone ($\text{C}_3\text{F}_6\text{O}$), *Spectrochim. Acta* 22 (1966) 993-1006.

- [91] S.G. Penoncello, Z. Shan, R.T. Jacobsen, A fundamental equation for the calculation of the thermodynamic properties of trifluoromethane (R-23), Univ. of Idaho, Moscow, ID (US), 2000.
- [92] S. Chen, R. Wilhoit, B.J. Zwolinski, Ideal gas thermodynamic properties of six chlorofluoromethanes, J. Phys. Chem. Ref. Data 5 (1976) 571-580.

Acknowledgement

First of all, I want to express all my sincere gratitude to my advisor prof. Yongwon Seo for his continuous and patient support of my Ph.D. study. He is the best professor I've ever known, who is a considerate and generous teacher while being a passionate and competent researcher at the same time. He always gave the motivation for my research and the guidance for me to become a better researcher. I believe I could complete my Ph.D. study thanks to his effort and support.

I express my appreciation to prof. Changsoo Lee, prof. Sung-Deuk Choi, prof. Sang Kyu Kwak and Dr. Seong-Pil Kang, who served as the examining committee of my Ph.D. thesis/dissertation. Their insightful and instructive advices encouraged me to broaden my research with various perspectives, and reinforce my Ph.D. thesis.

Also, I thank to my fellow ACE lab mates, for uncountable days we spent working together, and for all the memories we made in last 6 years.

Lastly, I would thank to my family, my one and only reason to accomplish the Ph.D. degree. I give my all honor to them. Thank you mom and dad, by always being there and giving me physical and spiritual support throughout my life. And I would express my special gratitude to my husband, Dr. Seunghyun Kim, who always supports my adventurous life and stands by my side. He has been a good husband and a good mentor to me at the same time, that I could learn lots of values and ways to live the life through him.

감사의 말

2009년 UNIST에 첫 발을 디딘 후로 벌써 10년이라는 세월이 흘렀습니다. 이 곳에 처음 입학할 때에는 제가 박사 학위까지 공부를 할 것이라는 것도, 또 10년이라는 긴 시간을 보낼 것이라는 것도 몰랐는데 말이지요. 아직도 그 때의 뿌연 먼지가 날리던 흙길과, 채 지어지지 않은 공학관 건물들, 제 손이 닿는 그 순간 처음 사용되던 책상들, 그리고 동기들의 설레고 들뜬 얼굴과 초봄 산골 특유의 짙은 풀 향기가 생생하게 떠오릅니다. 처음 제가 만났던 UNIST가 지금은 몰라볼 정도로 크고 멋있게 성장하는 그 시간 동안, 아마 저도 영성하고 서툰 스무 살 새내기에서 어엿한 공학 박사로 함께 성장해 온 듯 합니다. 이 페이지에서는, 제가 지금의 저로서 있을 수 있도록 저의 곁에서 도와주신 모든 분들께 감사 인사를 드리고자 합니다.

저의 부모님, 언제나 사랑으로 저를 키워 주시고 제가 바른 사람으로 성장할 수 있도록 삶의 스승이 되어 주셔서 감사합니다. 삶을 살아가고 겪을수록 저를 위한 부모님의 희생과 노력을 점차 더 많이 알아가는 것 같습니다. 제 이름을 지으실 때 담아주신 뜻대로, 이 박사 학위를 가지고 세상에 사랑과 은혜를 전하는 사람이 되도록 노력하겠습니다. 항상 사랑하고 감사합니다.

그리고 저의 학술적 어버이이신 서용원 교수님, 제가 학부 인턴 학생으로서 교수님과 함께한 지가 엇그제 같은데 벌써 교수님 밑에서 어엿한 박사로서 졸업을 하게 되니 감회가 참 새롭습니다. 급하고 꼼꼼하지 못한 성미 탓에 실험실에서 실수도 많이 하고, 고집이 세고 주장이 강해 교수님을 가끔 당혹스럽게 해 드린 기억도 납니다. 이렇게 모가 많고 부족한 저를 넓은 마음으로 차근차근 가르쳐주시고, 바른 방향으로 이끌어주시어 한 명의 연구자로 빛어 주신 교수님께 정말 감사 드립니다. 항상 ‘Technician’ 이 아닌 ‘Researcher’ 가 되라고 하신 교수님, 제가 앞으로 어떤 자리에 있든 교수님의 제자임을 잊지 않고 능동적인 연구자로 조금씩 더 성장할 수 있도록 노력할 것을 약속 드리며, 6년 동안 소중한 가르침 주셔서 다시 한 번 깊이 감사 드립니다.

또한 학위과정 중 저의 학술적 성장을 지켜 봐주시고 저에게 필요한 조언을 아낌없이 해주신 이창수 교수님, 최성득 교수님, 광상규 교수님 그리고 강성필 박사님께 진심으로 감사인사 드립니다. 바쁘신 와중에도 저의 박사학위 심사과정 단계마다 적극적으로 임해주시고, 보다 더 양질의 학위 논문을 완성할 수 있도록 세심한 도움을 주셔서 제가 무사히 박사학위를 마무리 할 수 있었습니다. 저에게 해 주신 과학적 조언과 엔지니어링적 조언을 거울 삼아, 앞으로 제가 하게 되는 어떤 연구에 있어서든지 항상 다각적 시각으

로 완성도 있는 연구를 수행하도록 노력하겠습니다.

6년동안 만났던 ACE LAB의 선배님들과 후배들에게 감사 인사를 전합니다. 특히 선배가 없던 저에게 처음으로 선배란 무엇인지 느끼게 해 주시고, 많은 것을 보고, 듣고, 배우도록 해 주신 이승민 박사님, 김소영 박사님, 이요한 박사님, 그리고 김연주 언니께 감사 드립니다. 이승민 박사님, 제가 미처 보지 못한 저의 모습을 알아주시고, 이해해 주시고, 보듬어 주셔서 정말 감사 드립니다. 제가 가장 힘든 시기에 저에게 따뜻한 위로와 진심 어린 응원을 주신 덕에 제가 힘을 많이 얻었습니다. 그리고 김소영 언니, 이요한 오빠, 6년 중 거의 4년이라는 시간을 함께하며 언니, 오빠와 크고 작은 추억을 많이 쌓았습니다. 아마 제 대학원 생활에서는 언니, 오빠와 함께한 시간이 가장 많이 생각 날 것 같아요. 그리고 저의 학위과정 중 소소한 추억과 인연이 되어준 고마운 후배들, 지연, 동영, 결, 준섭, 원중, 정훈 그리고 우진이에게 인사 전합니다. 말도 많고 탈도 많은 선배와 함께 실험실 생활하느라 소소한 마음 고생도 있었을 테고, 힘든 일도 있었을 테지만 무던하게 지금까지 잘 지내주어서 고맙습니다. ACE LAB 선후배 식구들, 다시 한번 저에게 좋은 인연이 되어주셔서 감사 드리며, 앞으로 하시는 모든 연구와 삶의 과정에서 행복하시길 기원합니다.

또한, 학위과정 중 저에게 크고 작은 힘이 되어 주었던 UNIST 09학번 동기들에게 감사합니다. 동규, 만날 때마다 내가 정말 솔직할 수 있는 시간을 주는 너에게 무척 고맙다. 오랜 시간을 함께하면서 우리가 이 학교의 보도 블록 중 밟지 않은 것이 있을까 할 만큼 종종 너와 함께한 산책이 나에겐 큰 휴식이자 위안이었어. 선영이와 상윤이, 소소한 농담과 웃음거리들이 넘쳐나는 너희를 만날 때면 나도 덩달아 곤잘 웃곤 했던 기억이 난다. 지금도 그렇지만 앞으로도 YOLO를 놓지 않는 너희가 되길 바라. 효주, 대학원 과정의 막바지에 당면하는 비슷한 고민과 걱정들을 너와 함께 나누고 서로 덜어줄 수 있어서 나는 참 좋았어. 이 외에도 승후, 수현이와 미처 언급하지 못한 우리 동기들, 모두 저와 10년에 가까운 시간을 함께 보내 주어서 감사합니다. 이제는 우리 UNIST의 1기라는 자부심을 가지고 사회에서 각자의 역할에 충실하며 멋있는 모습으로 다시 만나면 좋겠습니다.

마지막으로 저와 함께한 시간보다 앞으로 함께 할 시간이 훨씬 더 많을, 사랑하는 남편 김승현 박사님과 이 순간을 함께 기념하고 싶습니다. 학위과정 동안에 때로는 남편으로서, 때로는 동료로서, 그리고 때로는 친구로서의 당신이 곁에 있어준 덕분에 지금 제가 이렇게 무사히 박사학위를 마칩니다. 힘들거나 슬플 때, 기쁘거나 아플 때 언제나 제 옆자리에서 든든한 버팀목이 되어줄 뿐 아니라, 항상 묵묵히 응원과 격려를 해 주는 당신에게 참 감사합니다. 이제 10년에 걸친 UNIST에서의 시간을 함께 마무리하고 우리 둘 만

의 여정을 걸음에 있어서 앞으로도 한결같은 모습으로 사랑하고 의지하며, 또한 각자의 커리어에서 멋있는 동료이자 부부가 되길 소망합니다. 그리고 우리의 작은 고양이 천사들, 탄이와 울이, 너무나도 착하고 예쁘게 잘 키워서 정말 고맙고, 무지개 다리 건너는 그 날까지 행복과 사랑만 가득한 삶 살 수 있도록 엄마 아빠가 잘 할게요. 나의 남편, 그리고 새로운 우리 가족, 항상 사랑하고 고맙습니다.

돌아보면 UNIST는 저에게 소중한 인연과 추억을 너무나도 많이 안겨 주었습니다. 두근거리던 대학교 새내기 시절부터 박사 졸업을 하는 지금까지, 제 삶에 UNIST의 어느 것 하나 함께하지 않은 것이 없습니다. 이렇게 멋진 곳에서 학부와 대학원 과정을 거쳐 박사 학위를 잘 마무리 할 수 있게 되어서 무척 행복하고 감사합니다. 이 곳에서 이루어 낸 저의 박사 학위 논문이, 동료 공학자들과 앞으로 수학 할 많은 후배들에게 좋은 참고자료로 쓰여 미래의 과학기술 발전에 조금이나마 보탬이 되었으면 합니다. 감사합니다.

2019년 1월

김 은 애